Modèles d'endommagement à gradient en grandes déformations

Blandine Crabbé

NNT : 2018SACLX085

Thèse de doctorat

Gradient damage models in large deformation

Thèse de doctorat de l'Université Paris-Saclay
préparée à l'Ecole polytechnique

Ecole doctorale n°579 Sciences mécaniques et énergétiques, matériaux et géosciences (SMEMAG)
Spécialité de doctorat : Mécanique des matériaux

Thèse présentée et soutenue à Palaiseau, le 15 novembre 2018, par

MME BLANDINE CRABBÉ

Composition du Jury :

M. Patrick LE TALLEC Professeur, Ecole polytechnique	Président du jury
Mme Laura DE LORENZIS Professeur, Technische Universität Braunschweig	Rapporteur
M. Oscar LOPEZ-PAMIES Professeur associé, University of Illinois	Rapporteur
M. Khrishnaswamy RAVI-CHANDAR Professeur, University of Texas	Examinateur
M. Joachim GUILIÉ Docteur, MFP Michelin	Encadrant industriel
M. Jean-Jacques MARIGO Profeseur, Ecole polytechnique	Directeur de thèse

Thèse de doctorat
pour obtenir le titre de
Docteur de l'Université Paris-Saclay
Préparée à l'Ecole polytechnique
Spécialité : MÉCANIQUE

Gradient damage models in large deformation

Présentée par Blandine Crabbé

Thèse soutenue le 15 novembre 2018 à l'Ecole polytechnique devant un jury composé de

Patrick Le Tallec	Prof. Ecole polytechnique	Président
Laura de Lorenzis	Prof. TU Braunschweig	Rapporteur
Oscar Lopez-Pamies	Assoc. Prof. University of Illinois	Rapporteur
Krishnaswamy Ravi-Chandar	Prof. University of Texas	Examinateur
Jean-Jacques Marigo	Prof. Ecole polytechnique	Directeur de thèse
Joachim Guilié	Dr. MFP Michelin	Encadrant industriel

Laboratoire de Mécanique des Solides
Ecole polytechnique
91120 Palaiseau, France

Mercis

Il est parfois bien difficile de mettre des mots sur des sentiments, et je suis très admirative de ceux qui réussissent avec brio l'exercice de style le plus complexe du doctorat, à savoir l'écriture des remerciements. Ce n'est malheureusement pas mon cas, et je m'excuse auprès de tous ceux qui auraient mérité éloges et compliments, et ne recevront qu'un simple **M**erci. Qu'ils sachent toutefois qu'il est écrit en toute sincérité, et que cette simplicité ne fait que cacher ma profonde reconnaissance.

Merci à mes rapporteurs, Laura de Lorenzis et Oscar Lopez Pamies, d'avoir lu la thèse et fait le déplacement pour la soutenance.

Merci au président du jury, et directeur du laboratoire, Patrick Le Tallec, pour son profond dévouement pour le laboratoire, qui en fait un lieu où il fait bon travailler.

Merci à mon directeur de thèse, Jean-Jacques Marigo, pour sa gentillesse et sa pédagogie.

Merci à Joachim Guilié, mon référent Michelin, pour son aide dans la découverte du monde de l'entreprise.

Merci à Ramzy Boussetta et à toute l'équipe Michelin pour leur accueil chaleureux et leur bienveillance lors de mes passages à Ladoux.

Merci à Eric Chamberland, pour son aide, sa disponibilité, et sa simplicité.

Merci aux secrétaires du laboratoire, pour leur bonne humeur et leur aide.

Merci à tous les doctorants pour les bons moments partagés au LMS. En particulier, **M**erci à Erwan pour les innombrables cafés pris ensemble, **M**erci à Anchal pour les aventures, **M**erci à Laurent pour les débats philosophiques, **M**erci à Ustim, Jean-Pierre, Alexandre, et tous ceux que j'oublie.

Merci à ma famille pour son soutien indéfectible (et parce qu'avec vous, on a la garantie de ne jamais s'ennuyer !).

Merci à Arthur pour sa présence à mes côtés, passée, présente, et à venir. *Vamos pegar o primeiro avião…*

Vous avez fait de ces trois années des années inoubliables, riches en émotions, et sans vous tous cette thèse aurait été bien différente.

Contents

Résumé

Griffith fut l'un des pionniers de la mécanique de la rupture, et le premier à concevoir un lien entre la propagation d'une fissure et la création d'une énergie de surface. Il a su voir la croissance d'une fissure comme le résultat d'une compétition entre la restitution d'énergie de déformation et la création d'une énergie de surface au cours d'un incrément de longueur de fissure. Depuis ce temps, l'intérêt pour la modélisation de la nucléation et la propagation des fissures n'a fait que croître. En 1998, Francfort et Marigo ont proposé une approche variationnelle de la rupture, dans laquelle l'évolution de l'endommagement ou d'une fissure est régie par un principe de minimisation d'énergie. Dans le cadre de matériaux fragiles, avec un comportement adoucissant, ils ont construit des modèles d'endommagement qui reposent sur trois grands principes : l'*irréversibilité*, la *stabilité* et le *bilan d'énergie*. Ils ont régularisé ces modèles en ajoutant à l'énergie un terme contenant un gradient spatial d'endommagement pondéré par un paramètre appelé *longueur caractéristique* ou longueur interne. Au cours des dernières années, ces modèles, parfois appelés modèles à champs de phase, ont été largement utilisés pour modéliser la rupture fragile et ductile, depuis l'initiation de l'endommagement jusqu'à la propagation d'une fissure. Ils ont été enrichis par l'apport de couplages avec de la plasticité, de la température ou de la dynamique. Cependant, la majorité des études disponibles dans la littérature ne concerne que le cadre des petites déformations, et très peu d'études poussées ont été menées afin d'étudier leur pertinence dans un contexte de grandes déformations. Le but de ce travail est par conséquent d'étudier ces modèles dans un contexte de grandes déformations, tant d'un point de vue analytique que numérique.

Dans la première partie de ce travail, nous établissons des solutions analytiques d'évolution, homogène et localisée, de l'endommagement, pour des matériaux visqueux, en petites et en grandes déformations. Les calculs se font dans un cadre uni-dimensionnel, sur une barre soumise à un déplacement à l'une de ses extrémités. En petites déformations, les modèles rhéologiques de Maxwell et Poynting-Thomson sont étudiés, et en grandes déformations, les modèles de Maxwell et Zener sont choisis. Une étude sur l'évolution de l'endommagement dans un cas purement hyperélastique est aussi menée. En grandes déformations, les calculs se font dans la configuration de référence. L'énergie dissipée par l'endommagement est écrite sous la même forme que dans le cas d'un matériau élastique linéaire. Dans le cas d'une barre hyperélastique, lorsque l'endommagement atteint sa valeur maximale, la barre est considérée comme cassée, et par conséquent l'énergie hyperélastique est nulle. L'énergie de rupture pour un matériau hyperélastique est donc la même que pour un matériau linéaire élastique. Ceci permet de comparer les résultats analytiques et numériques. Dans le cas des matériaux visqueux, que ce soit en petites ou en grandes déformations, les études analytiques ont mené aux mêmes résultats. Il s'avère que pour le modèle de Maxwell, qui est un modèle de fluide, il existe une vitesse de déformation seuil en-dessous de laquelle un matériau ne peut s'endommager. Pour le modèle de Poynting-Thomson, qui représente le comportement d'un solide, une telle condition quant au développement de l'endommagement homogène n'existe

pas : quelle que soit la vitesse de déformation imposée, la barre peut toujours s'endommager. En revanche, les développements ont montré qu'il existe tout de même une condition sur la valeur de la vitesse de déformation pour que l'endommagement se localise sur la barre.

A cette première partie analytique succède naturellement une partie numérique qui détaille l'implémentation des modèles d'endommagement à gradient dans des codes éléments finis en grandes déformations : la librairie FEniCS a été utilisée, notamment pour effectuer des tests en 1D et 2D. Le code académique MEF++ a quant à lui été utilisé pour des simulations de taille plus conséquentes, en 2D et 3D. De même qu'en petites déformations, une stratégie de minimisation alternée est adoptée pour résoudre successivement les problèmes d'endommagement et de déplacement. Le comportement hyperélastique du matériau est modélisé par une loi de Mooney-Rivlin quasi-incompressible. Une méthode mixte pénalisée en déplacement-pression est utilisée : la pression est discrétisée avec des champs scalaires constants par éléments, tandis que le déplacement est discrétisé avec des champs linéaires ou quadratiques, selon la complexité des cas étudiés. De nombreux tests sont effectués, sur diverses géométries en 2D et 3D. Cela a permis de mettre en évidence la capacité des modèles à initier de l'endommagement en grandes déformations dans des structures parfaitement saines, pour des matériaux quasi-incompressibles.

Les modèles d'endommagement utilisés pour la seconde partie ne sont cependant capables d'initier de l'endommagement que dans les zones ou la déformation est importante, c'est-à-dire dans les zones de forte contrainte déviatorique. Il a toutefois été montré que certains matériaux polymères, quasi-incompressibles, s'endommagent dans les zones de forte pression hydrostatique. Par conséquent, la recherche et l'étude d'un modèle d'endommagement capable d'initier de l'endommagement dans les zones de forte pression, pour des matériaux quasi-incompressibles lorsqu'ils sont sains, fait l'objet d'une troisième partie. Une nouvelle dépendance à l'endommagement est introduite dans le coefficient de compressibilité. Des développements analytiques en 1D et 2D permettent de vérifier l'implémentation de ces nouveaux modèles.

Enfin, la croissance brusque de cavités dans un matériau hyperélastique, appelée phénomène de cavitation, est étudiée, ainsi que son interaction avec l'endommagement. Dans un premier temps, nous considérons la cavitation comme une simple bifurcation hyperélastique d'un matériau néo-Hookéen compressible isotrope. Nous étudions le cas d'une sphère pleine soumise à une élongation, et déterminons l'expression analytique de l'élongation critique pour laquelle un trou fait son apparition. Dans un second temps, nous montrons qu'il y a une compétition entre la cavitation et l'endommagement, et qu'en fonction de la valeur du ratio des élongations critiques respectives pour chaque phénomène, deux types de rupture apparaissent.

Abstract

Gradient damage models, also known as phase-field models, are now widely used to model brittle and ductile fracture, from the onset of damage to the propagation of a crack in various materials. Yet, they have been mainly studied in the framework of small deformation, and very few studies aims at proving their relevance in a finite deformation framework. This would be more helpful for the tire industry that deals with very large deformation problems, and has to gain insight into the prediction of the initiation of damage in its structures.

The first part of this work places emphasis on finding analytical solutions to unidimensional problems of damaging viscous materials in small and large deformation. In all the cases, the evolution of damage is studied, both in the homogeneous and localised cases. Having such solutions gives a suitable basis to implement these models and validate the numerical results.

A numerical part naturally follows the first one, that details the specificities of the numerical implementation of these non local models in large deformation. In order to solve the displacement and damage problems, the strategy of alternate minimisation (or staggered algorithm) is used. When solved on the reference configuration, the damage problem is the same as in small deformation, and consists in a bound constraint minimisation. The displacement problem is non linear, and a mixed finite element method is used to solve a displacement-pressure problem. A quasi-incompressible Mooney-Rivlin law is used to model the behaviour of the hyperelastic material. Various tests in 2D and 3D are performed to show that gradient damage models are perfectly able to initiate damage in sound, quasi-incompressible structures, in large deformation.

In the simulations depicted above, it should be noted that the damage laws combined to the hyperelastic potential results in an initiation of damage that takes place in zones of high deformation, or in other words, in zones of high deviatoric stress. However, in some polymer materials, that are known to be quasi-incompressible, it has been shown that the initiation of damage can take place in zones of high hydrostatic pressure. This is why an important aspect of the work consists in establishing a damage law such that the material be incompressible when there is no damage, and the pressure play a role in the damage criterion. Such a model is exposed in the third part.

Finally, the last part focuses on the cavitation phenomenon, that can be understood as the sudden growth of a cavity. We first study it as a purely hyperelastic bifurcation, in order to get the analytical value of the critical elongation for which cavitation occurs, in the case of a compressible isotropic Neo-Hookean material submitted to a radial displacement. We show that there is a competition between the cavitation phenomenon and the damage, and that depending on the ratio of the critical elongation for damage and the critical elongation for cavitation, different rupture patterns can appear.

CHAPTER I

INTRODUCTION

Contents

In this introduction, we will first recall the history of damage models, with an overview of non local models and a highlight on the gradient damage models. It will be followed by the construction of these gradient damage models that will be used in this manuscript. Finally, we will describe the contexts -both scientific and industrial, in which this work has taken form.

I.1 History of damage models

While rupture mechanics aims at the description of a macroscopic crack that goes through a structure whose material is sound, damage mechanics aims at describing the phenomenon that lead to the apparition of a macroscopic crack. The state of damage characterises the state of a material between the perfectly sound material –exempt of any micro defects such as micro cracks or micro cavities, and the existence of a crack at a mesoscale. In the framework of

continuum mechanics, damage models use an internal variable to describe the deterioration of the material *via* the quantification of defects present in the material. At the macroscale, this deterioration can be observed through its effects on macroscopic properties of the material: it can decrease the elasticity modulus, the yield stress (when coupled to plasticity), the density, etc.

An homogenisation operation is introduced in order to quantify the presence of micro defects in the material and to define an average of the stress and strain fields. Let us consider a solid in which a damaged representative volume element (RVE) was isolated, and whose sound section is noted δS and damaged section δS_D. The damage variable is defined by

$$D(\overrightarrow{n}) = \max\left(\frac{\delta S_D}{\delta S}\right) \tag{I.1}$$

and it corresponds to the density of micro cracks in the RVE of normal $\overrightarrow{n}$. For isotropic damage, the distribution of defects is uniform in all directions, and the value of $D(\overrightarrow{n})$ does not depend on the orientation $\overrightarrow{n}$. Thus, the variable D is enough to characterise the state of damage. $D = 0$ corresponds to the non damaged state, while $D = 1$ corresponds to the rupture of the element. An effective stress has therefore to be introduced, that is defined as the stress related to the surface that can actually resist to the efforts

$$\tilde{\sigma} = \sigma\frac{S}{\tilde{S}} \quad \text{or} \quad \tilde{\sigma} = \frac{\sigma}{1-D}. \tag{I.2}$$

Many phenomenological damage laws have been introduced in the past. One of the first was Kachanov's visco-plastic damage law, introduced in 1958 [31], in which he introduced a macroscopic damage variable to describe the creep. His pioneering work was soon followed and the theory of continuum damage mechanics (CDM) thoroughly developed in the last decades. It is well described in the book of Lemaitre [37] or Lemaitre and Desmorat [39].

Nowadays, many damage laws exist in the literature, and can be classified into two main families: the local and non local damage laws. Local damage laws state that the damage at one point of the structure does not depend on the damage on the surrounding points. These models have been proven to be unsuitable to model the damage evolution of a structure, for various reasons. First, one can show that it is possible, using these models, to break a structure, *i.e.* reach a damage value that is maximum, without any cost of energy. Indeed, the damage band can be taken as thin as one wants, and when it reduces to zero, the dissipated energy which is the integral of the dissipated density energy over the domain also reduces to zero. This a a first reason that demonstrates that local models do not work well. Moreover, it has been shown that they induce a very strong dependency to the mesh: the damage band width is equal to the mesh element size. Finally, demonstrations of the instability of the solutions of the damage evolution have also been made. Thus, there are physical, numerical and mathematical arguments that caution us not to use local damage models.

To alleviate all these faults, non local damage models have been introduced. A review of these models can be read in [8]. There are two main schools regarding the formulation of the

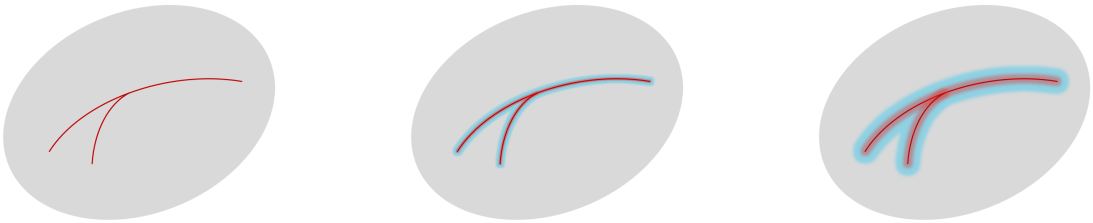

(a) Sharp crack *(b) Regularisation with $\ell/2$* *(c) Regularisation with ℓ*

Figure I.1: Regularisation of a sharp crack: the sharp interface is replaced by a smeared zone whose width depends on the internal length ℓ.

non locality of the damage. The first deals with the study of non local models of integral type. In these models, the constitutive law of a material at a given point contains terms that average a state variable, or a thermodynamic potential on a given vicinity of the considered point. The second group introduces gradient terms of state variables or thermodynamic forces. The common point of these two different approaches lies in the introduction of a *characteristic length* – or internal length, that controls the width of the damaged zone. We will focus mainly on the non local damage models of gradient type, called "gradient damage models", and sometimes referred to in the literature as "phase field models". The introduction of a spatial gradient of the damage variable regularises the displacement discontinuity: the sharp interface of the crack which induces a jump of the displacement across the two lips of the crack is now replaced by a smeared zone of finite width where the damage is continuous, as can be seen on Figure I.1. The localisation of damage is also penalised: if the damage localises over a very thin band, the gradient is therefore very high and the dissipated energy can not be zero any more. The construction of these gradient damage models, introduced in 1998 by Francfort and Marigo [18] is the object of the next part.

I.2 Construction of damage gradient models

This section is an introduction to the variational approach to fracture where we show, based on [45], how the damage evolution problem can be written with a variational formulation. There exists plethora of literature on this subject, the reader can refer to [9], [10], [18], [19], [46],[53], [54],[55].

Following the paper of [45], we will first expose the construction of local damage models based on thermodynamic principles, and after showing that they do not work well, a non local term of dissipated energy will be introduced in the strain work. Notations will be introduced along the presentation, but a table that summarises all the notations can be found in I.3.

For this general presentation, we will work in the framework of small deformation, for isotropic and linear elastic materials. We will also make the assumption that apart from the

damage, there is no other source of dissipation of energy.

I.2.1 Non regularised models

First, we construct local damage models: after determining the principal ingredients of a damage model, the evolution law can be written using thermodynamic arguments. We show that the problem can be formulated under a weak form, and we establish the three principles on which the study of regularized models relies.

I.2.1.a Modelling ingredients

To construct a damage model, three elements are necessary:

i) A damage parameter: here, it is a scalar (we are working with isotropic materials) variable, α, that takes its values in an interval $[0, \alpha_M[$. The value zero corresponds to a perfectly sound material while the value α_M, which can be finite or infinite, depending on the model, corresponds to the final stage of damage in the structure.

ii) The dependency of the stress-strain relation to the damage parameter: for a fixed value of α, the material has a linear elastic behaviour. It progressively loses rigidity when α grows: its elasticity is characterised by the relation $\alpha \mapsto \mathrm{E}(\alpha)$ between the stiffness tensor and the damage parameter.

iii) An evolution law of α.

I.2.1.b Evolution law of α

In the case of materials that are time independent, the evolution laws are governed by threshold laws and can be written with Kuhn-tucker conditions that involve a function of the damage α and the linearised deformation tensor $\boldsymbol{\varepsilon}$, $\phi : \mathbb{M}_s^N \times \mathbb{R}^+ \mapsto \mathbb{R}$ that is written, in the case of damage

$$\begin{cases} \dot{\alpha} \geq 0 \\ \phi(\boldsymbol{\varepsilon}, \alpha) \leq 0 \\ \dot{\alpha}\phi(\boldsymbol{\varepsilon}, \alpha) = 0 \end{cases} \tag{I.3}$$

where $\dot{\alpha}$ is the time derivative of the damage.

In I.3, the first inequality is called the *irreversibility condition*. It states that the damage can only grow or stay constant. By no means can it decrease, which can be understood as the fact that once a material is damaged, it cannot heal. The second inequality introduces a *damage criterion*, characteristic of threshold laws. The last equation of I.3, called *consistency condition*, allows for the growing of damage only if the damage criterion is reached.

The admissible strain (and respectively, stress) domains are defined by

$$\mathscr{R}(\alpha) = \{\boldsymbol{\varepsilon} \mid \phi(\boldsymbol{\varepsilon}, \alpha) \leq 0\} \tag{I.4}$$

and

$$\mathscr{R}^*(\alpha) = \{\boldsymbol{\sigma} \mid \phi(\mathrm{S}(\alpha)\boldsymbol{\sigma}, \alpha) \leq 0\}\,, \tag{I.5}$$

where $\mathrm{S}(\alpha) = \mathrm{E}(\alpha)^{-1}$ is the compliance tensor. The boundary of the admissible strain domain is defined by

$$\partial\mathscr{R}(\alpha) = \{\boldsymbol{\varepsilon} \mid \phi(\boldsymbol{\varepsilon}, \alpha) = 0\}\,. \tag{I.6}$$

The Drucker-Iliushin postulate

$$W = \oint_{\mathscr{C}} \boldsymbol{\sigma}\cdot\mathrm{d}\varepsilon \geq 0 \tag{I.7}$$

which states that energy has to be supplied to the material so that it can do a cycle of deformation $\mathscr{C}$ (the strain work has to be positive over a cycle), implies that the evolution law of α has necessarily to be *standard*. For the demonstration, the reader can refer to [52].

Writing

$$\psi(\boldsymbol{\varepsilon}, \alpha) = \frac{1}{2}\mathrm{E}(\alpha)\boldsymbol{\varepsilon}\cdot\boldsymbol{\varepsilon} \tag{I.8}$$

the elastic energy for a given α, with E the elasticity tensor, we recover the standard law

$$-\frac{1}{2}\mathrm{E}'(\alpha)\boldsymbol{\varepsilon}\cdot\boldsymbol{\varepsilon} \leq k(\alpha), \tag{I.9}$$

where $k(\alpha) = -\dfrac{\partial\psi}{\partial\alpha}(\boldsymbol{\varepsilon}, \alpha)$ for $\boldsymbol{\varepsilon} \in \partial\mathscr{R}(\alpha)$.

Remark ([18]): in the following work, we will consider that k is a constant. Its value is determined *via* a variable change, and its dimension is the one of a pressure that corresponds to the stress of the first apparition of damage during a traction test.

I.2.1.c Softening and hardening behaviours

Strain space

In the strain space, the evolution law (I.9) is written

$$\boldsymbol{\varepsilon}\cdot\boldsymbol{\varepsilon} \leq \frac{2k}{-\mathrm{E}'(\alpha)}. \tag{I.10}$$

When $\mathscr{R}(\alpha)$ is increasing with α, we speak of strain positive yielding. This is equivalent to the increase of $-1/\mathrm{E}'(\alpha)$, which is also the convexity of $\mathrm{E}''(\alpha) > 0$. Conversely, the negative strain yielding corresponds to the diminishing of the admissible strain domain when the damage is growing, which can be written $\mathrm{E}''(\alpha) < 0$.

Stress space

In the stress space, the evolution law (I.9) is

$$\frac{1}{2}\mathrm{S}'(\alpha)\boldsymbol{\sigma}\cdot\boldsymbol{\sigma} \leq k. \tag{I.11}$$

We call it hardening when $\mathscr{R}^*(\alpha)$ increases with α, *i.e.* when $\mathrm{S}''(\alpha) < 0$. We call it softening when the admissible stress domain decreases with the increase of α, so when $\mathrm{S}''(\alpha) > 0$. One interesting property is that hardening implies positive strain yielding.

Examples

There exists two main families of models of damage laws,

$$\mathrm{E}(\alpha) = (1-\alpha)^p \mathrm{E}_0, \ \alpha \in [0,1], \tag{I.12}$$

and

$$\mathrm{E}(\alpha) = \frac{\mathrm{E}_0}{(1+\alpha)^q}, \ \alpha \in [0,\infty), \tag{I.13}$$

where $p, q \in \mathbb{N}$. A study of the sign of the second derivative of (I.13) leads to the following result: if $0 < q < 1$, the models are hardening, if $q > 1$, they are softening damage models.

I.2.1.d Energy construction and stability

We write

$$W = \int_{t_0}^{t_1} \boldsymbol{\sigma}(t)\cdot\dot{\boldsymbol{\varepsilon}}(t)\mathrm{d}t \tag{I.14}$$

the strain work. It is a state function (see [18]) that depends only on $\boldsymbol{\varepsilon}$ and α: the work supplied to transform the material from a sound state ($\alpha = 0$) to a state of strain and damage $(\boldsymbol{\varepsilon}, \alpha)$ is independent of the path of deformation. Therefore we can write the strain work as

$$W(\boldsymbol{\varepsilon}, \alpha) = \frac{1}{2}\mathrm{E}(\alpha)\boldsymbol{\varepsilon}\cdot\boldsymbol{\varepsilon} + k\alpha, \tag{I.15}$$

in which we can observe the elastic energy density $\frac{1}{2}\mathrm{E}(\alpha)\boldsymbol{\varepsilon}\cdot\boldsymbol{\varepsilon}$ and the dissipated energy density $k\alpha$. We have shown that the strain energy density is the sum of the elastic energy density and the dissipated energy density.

Let us note that with this form of energy, the second thermodynamic principle, under the Clausius-Duhem inequality, is automatically fulfilled (see [53]).

The study of stable states of a system under a given loading is one way to select the solutions of an evolution problem. The stable states are usually considered as the local minima of the potential of a system. Yet, due to the irreversible nature of the damage, this definition has to be slightly adjusted.

Definition ([18]). An admissible state of strain and damage of a brittle structure submitted to a given loading is stable if and only if there exists a vicinity of admissible stable states in which all other accessible state has a lesser potential energy.

This definition uses the notion of *accessible* state: even if there exists states of lesser potential energy, if the damage is also lesser, the structure will not go to it because the damage can only grow.

Remark. A position is stable only if it is an equilibrium position. Moreover, among the equilibrium positions, those whose second derivative is positive are stable, those whose second derivative is negative are unstable.

For a controlled deformation, the state $(\boldsymbol{\varepsilon}, \alpha)$ is stable if $W(\boldsymbol{\varepsilon}, \alpha + h) \geq W(\boldsymbol{\varepsilon}, \alpha)$ for $h \geq 0$ small enough. The development up to the second order of this expression gives

$$W(\boldsymbol{\varepsilon}, \alpha + h) = W(\boldsymbol{\varepsilon}, \alpha) + h\left(\frac{1}{2}\mathrm{E}'(\alpha) + w'(\alpha)\right) + \frac{h^2}{2}\frac{1}{2}\mathrm{E}'(\alpha)\boldsymbol{\varepsilon}\cdot\boldsymbol{\varepsilon} + \mathrm{o}(\|h\|)^2. \tag{I.16}$$

The first order gives the damage criterion while the second order developement gives the positive strain yielding.

I.2.1.e Variational formulation of the evolution problem

Now that all the preliminary notions have been introduced, we seek to solve a quasi-static evolution problem. Its consists in finding for each time t the displacement and damage fields u_t and α_t that fulfil under the strong form the mechanical equilibrium and the yield system of Kuhn-Tucker

$$\left.\begin{array}{l} \text{i) Equilibrium: } \mathrm{div}(\boldsymbol{\sigma}) = 0 \\ \text{ii) Boundary conditions} \\ \text{iii) Behaviour law} \\ \text{iv) Evolution law of } \alpha \\ \quad - \text{ irreversibility: } \dot{\alpha} \geq 0 \\ \quad - \text{ damage criterion: } -\dfrac{1}{2}\mathrm{E}'(\alpha)\boldsymbol{\varepsilon}\cdot\boldsymbol{\varepsilon} \leq w'(\alpha) \\ \quad - \text{ consistency condition: } \dot{\alpha}\left(\dfrac{1}{2}\mathrm{E}'(\alpha)\boldsymbol{\varepsilon}\cdot\boldsymbol{\varepsilon} + w'(\alpha)\right) = 0 \end{array}\right\} \tag{I.17}$$

To begin with, we write the total energy of the structure for a given state (u_t, α_t), at a given time t

$$\mathscr{E}_t(u_t, \alpha_t) = \int_\Omega W(\boldsymbol{\varepsilon}(u(x)), \alpha(x))\mathrm{d}x - \int_{\partial_F\Omega} F_t(x)\cdot u(x)\mathrm{d}s - \int_\Omega f_t(x)\cdot u(x)\mathrm{d}x, \tag{I.18}$$

where Ω is the reference domain of dimension N, with $u = U_t$ the imposed displacement on $\partial_D\Omega$, F_t is the imposed force on $\partial_F\Omega$, and f_t are the volume forces.

It can be shown (see [53]) or [52]) that the strong formulation (I.17) of the evolution problem is equivalent to the weak formulation (I.19) of this problem

$$\left.\begin{array}{l} \text{i) Admissibility of displacements: } u_t = U_t \text{ on } \partial_D\Omega \\ \text{ii) Initial condition: } \alpha(t=0) = \alpha_0 \\ \text{iii) Irreversibility: } \dot{\alpha} \geq 0 \\ \text{iv) Stability condition:} \\ \qquad \mathscr{E}_t'(u_t, \alpha_t)(v, \beta) \geq 0, \ \forall v \in \mathcal{C}_0, \ \forall \beta \in \mathcal{D}_t \\ \text{v) Energy balance:} \\ \qquad \dfrac{\mathrm{d}}{\mathrm{d}t}\left(\mathscr{E}_t(u_t, \alpha_t)\right) = \displaystyle\int_{\partial_D\Omega} \boldsymbol{\sigma}_t n \dot{u}_t \mathrm{d}s - \int_{\partial_F\Omega} \dot{F}_t \cdot u_t \mathrm{d}s - \int_\Omega \dot{f}_t \cdot u_t \mathrm{d}x \end{array}\right\} \tag{I.19}$$

where $\mathcal{C}_0$ is the set of admissible displacements fields at time t defined by

$$\mathcal{C}_0 = \left\{ v \in H^1(\Omega) \mid v = 0 \text{ on } \partial_D\Omega \right\}, \tag{I.20}$$

and $\mathcal{D}_t$ is the set of admissible damage fields at time t defined as follows

$$\mathcal{D}_t = \left\{ \beta \in H^1(\Omega) \mid 0 \leq \alpha_t \leq \beta \leq 1 \right\}. \tag{I.21}$$

I.2.2 Regularised model

In the previous section, we have shown how local damage models can be constructed, and how the evolution problem of a structure under a given loading can be written as a variational problem. Yet we will now see that these local models are not satisfactory and that another ingredient has to be added to the modelling.

I.2.2.a Why a regularisation?

The study of the solutions of an evolution problem, in the case of imposed displacements as well as imposed forces, has shown that these latter are all unstable [52], [18]. Moreover, local damage models exhibit strong dependency of the numerical solutions to the mesh that can lead to infinite localisation of the damage. Since the width of the damage band is controlled by the mesh element size, if the mesh is infinitely refined, the damage zone surface tends to be null, and the dissipated energy tends to zero. We see clearly that breaking a structure without any cost of energy is not physically acceptable, as is the fact that the localisation of damage be a process driven by the mesh size.

To remedy these problems, Francfort and Marigo introduced a regularisation of the damage solution. The idea consists in penalising the localisation of the damage so that if localises on a very thin band, it has to cost it a lot of energy. Practically speaking, a term containing

a spatial gradient of damage is introduced in the energy density, so that the damage at one point of the structure depends also of the damage on the points surrounding it, and the damage model becomes a non local damage model.

The previous approach where we developed the construction of the local (or non regularised) models will now reveal itself very powerful for the construction of non local models. Indeed, the evolution problem and the stability of the states will be formulated in the same way, the only difference lying in the expression of the energy. We will use the three previously established principles of *irreversibility*, *stability* and *energy balance* to obtain the new evolution problem.

I.2.2.b Irreversibility, stability, energy balance

Terms of spatial gradient of α are introduced in the energy, and by taking into account the objectivity principle that applies to α, and the hypothesis of isotropy of the material, we finally obtain the expression of the strain energy density for a gradient damage model

$$W(\boldsymbol{\varepsilon}, \alpha, \nabla\alpha) = \frac{1}{2}\mathrm{E}(\alpha)\boldsymbol{\varepsilon}\cdot\boldsymbol{\varepsilon} + w(\alpha) + \frac{1}{2}w_1\ell^2\nabla\alpha\cdot\nabla\alpha, \tag{I.22}$$

where ℓ is a characteristic length of the material, also called internal length. $w(\alpha)$ is the dissipated energy density during a homogeneous process of damage.

The first order stability condition (I.19).iv written with the energy (I.22) gives on one hand the equilibrium equation $\mathrm{div}(\boldsymbol{\sigma}) = 0$, and on the other hand the local damage criterion after integrating by part

$$w'(\alpha) + \frac{1}{2}\mathrm{E}'(\alpha)\boldsymbol{\varepsilon}\cdot\boldsymbol{\varepsilon} - w_1\ell^2\Delta\alpha \geq 0 \quad \text{in } \Omega, \tag{I.23}$$

as well as boundary conditions on α

$$\frac{\partial\alpha}{\partial n} \geq 0 \quad \text{on } \partial\Omega. \tag{I.24}$$

The difference in the damage criterion between a local and a non local damage models holds to the presence of a Laplacian of α in the damage criterion when the model is regularised.

The energy balance (I.19).v enables to find the consistency conditions in the bulk and on the boundaries

$$(w'(\alpha) + \frac{1}{2}\mathrm{E}'(\alpha)\boldsymbol{\varepsilon}\cdot\boldsymbol{\varepsilon} - w_1\ell^2\Delta\alpha)\dot{\alpha} = 0 \quad \text{in } \Omega \tag{I.25}$$

$$\frac{\partial\alpha}{\partial n}\dot{\alpha} = 0 \quad \text{on } \partial\Omega. \tag{I.26}$$

I.2.2.c Localisation on a 1D bar

Since the introduction of a term with a spacial gradient of α in the energy aims at regularising the localisation of damage, an interesting study is the one of a 1D bar submitted to traction,

on which the damage localises. This approach is general, and can (and will) be applied to other similar problems of damage localisation.

Let us consider a bar of length L, on which a crack develops at a point X_0. The damaged zone is considered of size $2d$, and the damage is localised on the interval $(X_0 - d, X_0 + d)$. We want to determine the expression of the damage on this zone, as well as the dissipated energy of the broken bar. The dissipated energy $w(\alpha)$ is from now on written

$$w(\alpha) = w_1 \alpha. \tag{I.27}$$

The method consists in writing the damage criterion

$$0 = w'(\alpha) - \frac{\sigma^2}{E_0(1-\alpha)^3} - w_1 \ell^2 \alpha'', \tag{I.28}$$

to integrate it

$$C = w_1 \alpha - \frac{\sigma^2}{2E_0(1-\alpha)^2} - \frac{1}{2} w_1 \ell^2 \alpha'^2 \tag{I.29}$$

where C is a constant determined with $\alpha = 0$ in (I.29)

$$C = -\frac{\sigma^2}{2E_0}.$$

Damage profiles are thus given by

$$\pm \, \mathrm{d}x = \frac{w_1 \ell \, \mathrm{d}\alpha}{\sqrt{2w_1\alpha + \frac{\sigma^2}{E_0}(1 - \frac{1}{(1-\alpha)^2})}}, \tag{I.30}$$

and when a crack has appeared in X_0, $\sigma = 0$, and the damage profile is

$$\ell\sqrt{2\alpha} = \pm(x - (X_0 \pm d)). \tag{I.31}$$

d is such that $\alpha(X_0) = 1$ and is

$$d = \ell\sqrt{2}. \tag{I.32}$$

An illustration is shown on Figure I.2: when ℓ decreases, the profile becomes thinner and tends to a sharp crack.

The dissipated energy to create a crack is the integral over the bar of the dissipated energy through the damage process and the elastic energy. When a crack has appeared ($\sigma = 0$), the elastic energy is null, and the rupture energy, defined as the integral over the domain of the dissipated energy, is

$$G_c = \int_{X_0-d}^{X_0+d} \left(\frac{\sigma_c^2 \alpha(x)}{E_0} + \frac{1}{2} w_1 \ell^2 \alpha'(x)^2 \right) \mathrm{d}x. \tag{I.33}$$

where the critical stress σ_c is the stress for which damage first develops, and is $\sigma_c = \sqrt{w_1 E_0}$.

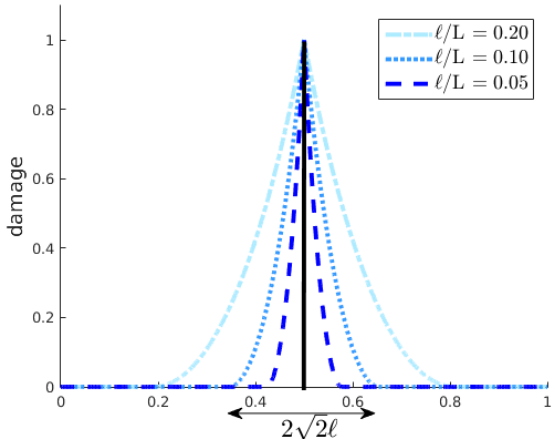

Figure I.2: Damage profile on a broken 1D bar for different internal lengths.

When $\sigma = 0$, (I.29) shows that the two contributions of (I.33) are equal. Moreover, because of the symmetry of the damage profile, the integral can be performed on a demi-profile only

$$G_c = 2 \int_{X_0}^{X_0+d} w_1 \ell^2 \alpha'(x)^2 \mathrm{d}x \tag{I.34}$$

and using (I.30), we get the expression of the rupture energy with respect to the internal length and the critical stress

$$G_c = \frac{4\sqrt{2}}{3} \sigma_c \ell. \tag{I.35}$$

I.2.2.d Strength of the model

The construction of the models brought out that they do not need any evolution law to be postulated, nor any *ad hoc* criteria that are sometimes used (Rankine, Mazars, etc). They are able to initiate and propagate a crack without the presence of any defect. There is no need of an *a priori* known crack path, and for this reason, they go much further into the modelling of rupture than the Griffith theory which can only predict whether a crack will propagate or not.

I.2.3 Numerical implementation

All along this work, analytical results will be compared to numerical results. This is why we chose to introduce now the method used to solve a quasi-static evolution problem of a damaging structure under loading. The time span $(0, T)$ over which the loading is applied is discretized and a time step is written Δt. The total energy of the structure is the integral

over the domain of the elastic energy and the dissipated energy, minus the external work

$$\mathscr{E}(u,\alpha) = \frac{1}{2}\int_\Omega \mathrm{E}(\alpha)\boldsymbol{\varepsilon}(u)\cdot\boldsymbol{\varepsilon}(u)\mathrm{d}x + G_c c_w \int_\Omega \left(\frac{w(\alpha)}{\ell} + \ell\nabla\alpha\cdot\nabla\alpha\right)\mathrm{d}x - (\text{Ext.Work}) \qquad \text{(I.36)}$$

where $\dfrac{1}{c_w} = 4\int_0^1 \sqrt{w(\alpha)}\mathrm{d}\alpha$ is a adimensionalisation parameter. In the numerical experiments, the dissipated energy is written in terms of G_c and $w(\alpha) = \alpha$, so that the link between this model and a fracture model like Griffith is more clear.

The numerical problem consists in minimising the total energy (I.36) with respect to both its variables u and α

$$\min_{u,\alpha}\left(\mathscr{E}(u,\alpha) = \int_\Omega \left(\frac{(1-\alpha)^2 + k_{res}}{2}\mathrm{E}_0\boldsymbol{\varepsilon}(u)\cdot\boldsymbol{\varepsilon}(u) + G_c\frac{3}{8}\left(\frac{\alpha}{\ell} + \ell\nabla\alpha\cdot\nabla\alpha\right)\right)\mathrm{d}x\right) \qquad \text{(I.37)}$$

This energy is not convex with respect to the pair (u,α), nevertheless, it is convex with respect to u and α separately. This is why a strategy of alternate minimisation, also called staggered algorithm, is chosen: at each time step, the displacement problem is solved, using a fixed value of the damage, then the damage problem is solved using the previous value of the displacement, and until there is a convergence on α. The algorithm is written as follows

- Initialization at time t_i: $(u_{old}, \alpha_{old}) = (u_{i-1}, \alpha_{i-1})$
- Repeat until $\|\alpha_{new} - \alpha_{old}\|_\infty < \text{tol}$
  1. Calculate, with $u(x) = t_i\varepsilon_0$ on $\partial_D\Omega$
     $u_{new} = \underset{u}{\operatorname{argmin}}\ \mathscr{E}(u, \alpha_{old})$
  2. Calculate, under the constraint $\alpha_{i-1} \leq \alpha \leq 1 \quad$ in Ω
     $\alpha_{new} = \underset{\alpha}{\operatorname{argmin}}\ \mathscr{E}(u_{new}, \alpha)$
- Update: $(u_i, \alpha_i) = (u_{new}, \alpha_{new})$

The numerical parameters and their influence on the results will be investigated, in particular in Chapter III.

I.3 Notations

We give in this section the notations that will be used throughout this thesis.

- Vectors are written in italic letters, like u, second order tensors are in boldface letters, like $\boldsymbol{\sigma}$, and fourth order tensors are written in capital upright letters, like E.

- In a uni-dimensional framework, all vectorial and tensorial quantities are written in italic, to show that they are scalar in that situation. For an example, u, σ, E, etc.
- Vectors components are written with indices, like u_i, and second order tensors components are written with two indices, like σ_{ij}.
- The Einstein summation convention is adopted.
- The inner product between two vectors or two tensors of same order is written with a dot, and stands for $u \cdot v = u_i v_i$ or $\boldsymbol{\sigma} \cdot \boldsymbol{\varepsilon} = \sigma_{ij} \varepsilon_{ij}$.
- The euclidean norm of a vector or a second order tensor is denoted $\|.\|$, as $\|u\| = \sqrt{u \cdot u}$, or $\|\boldsymbol{\sigma}\| = \sqrt{\boldsymbol{\sigma} \cdot \boldsymbol{\sigma}}$.
- The dot stands for the time derivative, as in $\dot{\alpha} = \partial \alpha / \partial t$.
- For a function of one variable, the prime stands for the derivative of the function with respect to its variable, as in $w'(\alpha) = \mathrm{d}w/\mathrm{d}\alpha$.
- For a functional, the prime stands for the Gâteaux derivative of the functional at a given point in an admissible direction, as in $\mathscr{E}'(\alpha)(\beta)$.
- tr stands for the trace operator, div stands for the divergence in the actual configuration (that is also the reference configuration in small deformation), and Div for the divergence in the reference configuration.

Table I.1 gives the main notations and symbols used in the following chapters.

Damage model	
α	Scalar damage variable
$\nabla \alpha$	Spatial gradient of damage
$w(\alpha)$	Dissipated energy density
ℓ	Internal length
σ_c	Critical stress
G_c	Rupture energy
d	Length of half the size of the localisation
Material constants	

Table I.1: Notations

A	Young modulus
ν	Poisson coefficient
μ	First Lamé coefficient
κ	Compressibility coefficient
E	4th order tensor of stiffness
S	4th order tensor of compliance
C	Neo-Hookean model coefficient
C_{10}, C_{01}	Mooney-Rivlin model coefficients

Kinematic

I	Identity tensor
$\boldsymbol{\varepsilon}$	Tensor of infinitesimal deformation
$\boldsymbol{\sigma}$	Cauchy stress tensor
$\boldsymbol{\sigma}^D$	Deviatoric part of $\boldsymbol{\sigma}$
p	Hydrostatic pressure
$\boldsymbol{F}$	Gradient deformation tensor
$\boldsymbol{C}$	Right Cauchy-Green deformation tensor
$\boldsymbol{B}$	Left Cauchy-Green deformation tensor
$\boldsymbol{E}$	Green-Lagrange deformation tensor
$\boldsymbol{\Pi}$	First Piola-Kirchhoff stress tensor
$\boldsymbol{S}$	Second Piola-Kirchhoff stress tensor
$\boldsymbol{\tau}$	Kirchhoff stress tensor
J	Determinant of $\boldsymbol{F}$
I_1, I_2	First and second invariants of $\boldsymbol{C}$
$\bar{I}_1$, $\bar{I}_2$	Reduced first and second invariants of $\boldsymbol{C}$

Various

N	Space dimension, $1 \leq N \leq 3$
ψ	Elastic energy density
W	Strain work density

Table I.1: Notations

$\mathscr{E}$	Total energy of the system
Ω, Ω_0	Domain in the actual - reference configuration
$\partial\Omega$	Boundaries of the domain
Δt	Time step
$\mathcal{C}_t$, $\mathcal{D}_t$, $\mathcal{X}_t$	Admissible strain, damage, viscous strain, domains

Chapter II

ε_0	Loading speed
$\boldsymbol{\varepsilon}^v$	Viscous deformation tensor
$\boldsymbol{\varepsilon}^e$	Elastic deformation tensor
A_v	Rigidity of the second elastic spring in the PT model
η	Viscosity coefficient
$\boldsymbol{F}^e$	Elastic part of the gradient deformation tensor
$\boldsymbol{F}^v$	Viscous part of the gradient deformation tensor
$\mathscr{C}_0$, $\mathscr{C}_i$, $\mathscr{C}_t$	Initial, intermediary, actual configurations

Table I.1: Notations

I.4 Project background and organization of the work

In the past years, gradient damage models – or phase field models, have been developed in many frameworks, and coupled with many phenomenons. They were coupled with temperature, which lead to the simulations of thermal shocks seen in [11], or with plasticity to model ductile fracture in [1] and more recently in [58]. Usually studied with a quasi-static loading, they are now also adapted to dynamic fragmentation, by calculating the displacement with the elastodynamics equation, see for example [41]. Recent work of [2] show that they are also relevant to model fatigue, provided that a dissipation potential which explicitly depends on the strain history be introduced, that enables the dissipated energy to decrease when the accumulated strain increases.

Although gradient damage models have been widely studied in many contexts in small deformation, their study has never been extended to large deformation. Indeed, the modelling of crack nucleation and propagation for rubbery material is not a subject that has been widely investigated in the past years. Yet, it is essential to understand these mechanisms because many materials of such a nature undergo loadings and solicitations that can lead to

fracture. This is the case for the industry of tires that would greatly benefit from a better understanding of these phenomena. Using the J-integral method, industrials are able to predict for what load a pre-existing crack will propagate, but for the most part, they are still unable to predict the initiation of damage in a sound structure, *i.e.* where and when the damage will begin. This work has therefore emerged from such a context, and aims at having a better understanding of the initiation of rupture in large deformation, while adapting the gradient damage models to the framework of large deformation.

In that perspective, the results are decomposed into four parts. In Chapter II, analytical solutions for three problems are constructed. Because of the viscous effects in polymers, two rheological models are investigated, in small and large deformation. This leads to the study of damaging viscoelastic materials, of hyperelastic materials and hyper-viscoelastic materials. Chapter III exposes the implementation of the gradient damage models in large deformation in an academic finite element code [16]: a recall is made of the method used to solve the displacement problem in finite strain, and numerical results are shown. The damage laws used in this chapter are such that the hydrostatic pressure does not play any role in the initiation of damage for an incompressible material. Therefore, Chapter IV presents a new damage law that overcomes this weakness. Both analytical and numerical results are exposed. Finally, Chapter V introduces the cavitation phenomenon, a famous damage process in polymers. It is first investigated as a purely hyperelastic bifurcation, then the competition that takes place between the cavitation and the damage is studied.

CHAPTER II

UNIDIMENSIONAL STUDY OF GRADIENT DAMAGE MODELS FOR VISCOELASTIC MATERIALS

Contents

In this chapter, we are mainly concerned with one dimensional studies, for viscous material in small and large deformation. Thus, we will first develop the behaviour of a viscous damaging bar in small deformation, then we will abandon the hypothesis of linearised deformation to study a hyperelastic bar, which will finally lead us to the analysis of a hyper-viscoelastic bar under loading.

II.1 Damage and viscoelasticity

II.1.1 Energy density, first order stability and energy balance in 3D

The three principles (irreversibility, first order stability and energy balance) that govern the evolution law of α, and were established in I.2.1.e remain valid if any other source of dissipation is added (plasticity, temperature). The difference lies in the total energy that now has to take into account the viscous dissipation.

II.1.1.a Rheological models and energy density

The connection between stress and strain for a viscoelastic material can be set through the use of rheological models. In the following, we will focus on the Maxwell and the Poynting-Thomson model, shown respectively on Figures II.12a and II.10b. The Maxwell model is the association in series of an elastic spring and a viscous dashpot, which, in the Poynting model, is replaced by a Kelvin-Voigt element. Note that in small deformation, Zener and Poynting-Thomson have similar responses, and thus are equivalent.

The energy density associated to these models is hence the sum of the elastic energy of the springs and the dissipated energy in the dashpot. The total deformation is decomposed as the sum of an elastic and an inelastic (viscous) energy. The time derivative of the viscous

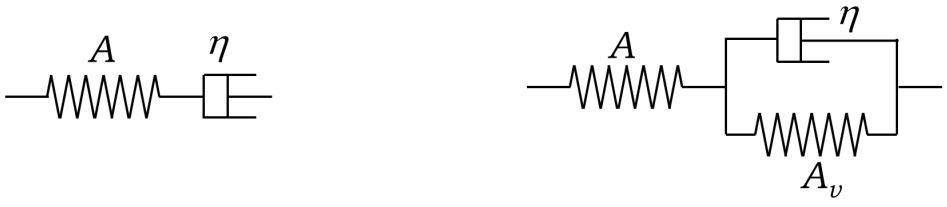

(a) Maxwell model *(b) Poynting-Thomson model*

Figure II.1: Rheological models

deformation $\dot{\varepsilon}^v$ that appears in the viscous dissipation potential is discretized, and we get

$$\psi(\boldsymbol{\varepsilon}, \boldsymbol{\varepsilon}^v) = \frac{1}{2}A(\boldsymbol{\varepsilon} - \boldsymbol{\varepsilon}^v)\cdot(\boldsymbol{\varepsilon} - \boldsymbol{\varepsilon}^v) + \frac{1}{2}A_v\boldsymbol{\varepsilon}^v\cdot\boldsymbol{\varepsilon}^v + \frac{\Delta t}{n}\eta\left(\frac{\| \boldsymbol{\varepsilon}^v - \boldsymbol{\varepsilon}^v_{i-1}\|}{\Delta t}\right)^n \tag{II.1}$$

where n is an integer that models the non linear behaviour of the spring. We will use $n = 2$ in order to work with linear viscoelastic laws. η characterises the viscous time scale, and has the dimension of a stress multiplied by a time.

Adding the dependency of the material parameters to the damage parameter such that A, A_v and η are functions of α and writing the strain work as the sum of the elastic potentials, the viscous dissipation potential, and the dissipated energy during the damage process, we obtain the total energy of the structure at time t

$$\begin{aligned}\mathscr{E}_t(u, \boldsymbol{\varepsilon}^v, \alpha) = \int_\Omega &\frac{1}{2}A(\alpha)(\boldsymbol{\varepsilon}(u) - \boldsymbol{\varepsilon}^v)\cdot(\boldsymbol{\varepsilon}(u) - \boldsymbol{\varepsilon}^v) + \frac{1}{2}A_v(\alpha)\boldsymbol{\varepsilon}^v\cdot\boldsymbol{\varepsilon}^v \\ &+ \frac{\Delta t}{n}\eta(\alpha)\left(\frac{\| \boldsymbol{\varepsilon}^v - \boldsymbol{\varepsilon}^v_{i-1}\|}{\Delta t}\right)^n + w(\alpha) + \frac{1}{2}w_1\ell^2\nabla\alpha\cdot\nabla\alpha.\end{aligned} \tag{II.2}$$

II.1.1.b First order stability

Using the first order stability principle (I.19) and thus deriving (II.2) in the admissible direction $(v, \boldsymbol{\xi}^v, \beta) \in \mathcal{C}_0\times\mathcal{X}\times\mathcal{D}_t$ gives

$$\begin{aligned}\mathscr{E}_t(u, \boldsymbol{\varepsilon}^v, \alpha)(v, \boldsymbol{\xi}^v, \beta) = \int_\Omega \Bigg\{ &\frac{1}{2}A'(\alpha)(\boldsymbol{\varepsilon}(u) - \boldsymbol{\varepsilon}^v)\cdot(\boldsymbol{\varepsilon}(u) - \boldsymbol{\varepsilon}^v)\beta + \frac{1}{2}A'_v(\alpha)\boldsymbol{\varepsilon}^v\cdot\boldsymbol{\varepsilon}^v\beta + w'(\alpha)\beta \\ &+ w_1\ell^2\nabla\alpha\cdot\nabla\beta + \frac{\Delta t}{2}\eta'(\alpha)\left(\frac{\| \boldsymbol{\varepsilon}^v - \boldsymbol{\varepsilon}^v_{i-1}\|}{\Delta t}\right)^2\beta \\ &+ A(\alpha)(\boldsymbol{\varepsilon}(u) - \boldsymbol{\varepsilon}^v)\cdot\boldsymbol{\varepsilon}(v) - A(\alpha)(\boldsymbol{\varepsilon}(u) - \boldsymbol{\varepsilon}^v)\cdot\boldsymbol{\xi}^v + A_v(\alpha)\boldsymbol{\varepsilon}^v\cdot\boldsymbol{\xi}^v \\ &+ \eta(\alpha)\left(\frac{\|\boldsymbol{\varepsilon}^v - \boldsymbol{\varepsilon}^v_{i-1}\|}{\Delta t}\right)\|\boldsymbol{\xi}^v\|\Bigg\}\,\mathrm{d}x \;\geq 0 \quad \forall(v, \boldsymbol{\xi}^v, \beta) \in \mathcal{C}_0\times\mathcal{X}\times\mathcal{D}_t,\end{aligned} \tag{II.3}$$

with the admissible spaces defined as follows

$$\mathcal{C}_0 = \left\{v \in H^1(\Omega) \mid v = 0 \text{ on } \partial_D\Omega\right\}, \tag{II.4}$$

$$\mathcal{D}_t = \left\{\beta \in H^1(\Omega) \mid 0 \leq \alpha_t \leq \beta \leq 1\right\}, \tag{II.5}$$

and

$$\mathcal{X} = \left\{\xi^v \in \mathrm{L}^2(\Omega)\right\}. \tag{II.6}$$

Taking $v = 0$ and $\boldsymbol{\xi}^{\boldsymbol{v}} = 0$ gives

$$\begin{aligned}\int_\Omega \beta\Bigg(&\frac{1}{2}A'(\alpha)(\boldsymbol{\varepsilon}(u) - \boldsymbol{\varepsilon}^{\boldsymbol{v}})\cdot(\boldsymbol{\varepsilon}(u) - \boldsymbol{\varepsilon}^{\boldsymbol{v}}) + \frac{1}{2}A'_v(\alpha)\boldsymbol{\varepsilon}^{\boldsymbol{v}}\cdot\boldsymbol{\varepsilon}^{\boldsymbol{v}} + w'(\alpha) - w_1\ell^2\Delta\alpha \\ &+ \frac{\Delta t}{2}\eta'(\alpha)\left(\frac{\| \boldsymbol{\varepsilon}^{\boldsymbol{v}} - \boldsymbol{\varepsilon}^{\boldsymbol{v}}_{\boldsymbol{i-1}}\|}{\Delta t}\right)^2\Bigg)\,\mathrm{d}x + \int_{\partial\Omega}\frac{\partial\alpha}{\partial n}\beta\mathrm{d}s \;\geq 0 \quad \forall\beta \in \mathcal{D}_t,\end{aligned} \tag{II.7}$$

and we obtain the local damage criterion by taking $\Delta t \to 0$

$$\frac{1}{2}A'(\alpha)(\boldsymbol{\varepsilon}(u)-\boldsymbol{\varepsilon^v})\cdot(\boldsymbol{\varepsilon}(u)-\boldsymbol{\varepsilon^v})+\frac{1}{2}A'_v(\alpha)\boldsymbol{\varepsilon^v}\cdot\boldsymbol{\varepsilon^v}+w'(\alpha)-w_1\ell^2\Delta\alpha \;\geq\; 0 \quad \text{in } \Omega, \tag{II.8}$$

as well as boundary conditions on α

$$\frac{\partial\alpha}{\partial n} \;\geq\; 0 \quad \text{on } \partial\Omega. \tag{II.9}$$

$\beta = 0$ and $\boldsymbol{\xi^v} = 0$ gives the equilibrium

$$\operatorname{div}(\boldsymbol{\sigma}) = 0 \quad \text{in } \Omega. \tag{II.10}$$

$\beta = 0$ and $v = 0$ gives

$$(-\boldsymbol{\sigma}+A_v(\alpha)\boldsymbol{\varepsilon^v})\cdot\boldsymbol{\xi^v}+\eta(\alpha)\left(\frac{\|\boldsymbol{\varepsilon^v}-\boldsymbol{\varepsilon^v_{i-1}}\|}{\Delta t}\right)\|\boldsymbol{\xi^v}\| \;\geq\; 0 \quad \forall\boldsymbol{\xi}^v\in\mathcal{X} \tag{II.11}$$

re written

$$(-\boldsymbol{\sigma}+A_v(\alpha)\boldsymbol{\varepsilon^v})\cdot\frac{\boldsymbol{\xi^v}}{\|\boldsymbol{\xi^v}\|}+\eta(\alpha)\frac{\|\boldsymbol{\varepsilon^v}-\boldsymbol{\varepsilon^v_{i-1}}\|}{\Delta t} \;\geq\; 0 \quad \forall\boldsymbol{\xi}^v\in\mathcal{X}. \tag{II.12}$$

For $\boldsymbol{\xi^v} = -\dfrac{-\boldsymbol{\sigma}+A_v(\alpha)\boldsymbol{\varepsilon^v}}{\|-\boldsymbol{\sigma}+A_v(\alpha)\boldsymbol{\varepsilon^v}\|}$, we have $\|\boldsymbol{\xi^v}\| = 1$ and injecting it in (II.12) gives

$$\eta(\alpha)\frac{\|\boldsymbol{\varepsilon^v}-\boldsymbol{\varepsilon^v_{i-1}}\|}{\Delta t} \;\geq\; \|-\boldsymbol{\sigma}+A_v(\alpha)\boldsymbol{\varepsilon^v}\|. \tag{II.13}$$

II.1.1.c Energy balance

In the configuration free of stresses on the edges, the energy balance states

$$\frac{\mathrm{d}\mathscr{E}}{\mathrm{d}t} = \int_{\partial_D\Omega}\boldsymbol{\sigma}_t n\dot{u}_t\mathrm{d}s, \tag{II.14}$$

where

$$\frac{\mathrm{d}\mathscr{E}}{\mathrm{d}t} = \mathscr{E}'(\boldsymbol{\varepsilon}(u_t),\boldsymbol{\varepsilon}^v_t,\alpha_t)(\boldsymbol{\varepsilon}(\dot{u}_t),\dot{\boldsymbol{\varepsilon}}^v_t,\dot{\alpha}_t). \tag{II.15}$$

We develop this expression

$$\begin{aligned}\frac{\mathrm{d}\mathscr{E}}{\mathrm{d}t} = \int_\Omega\Bigg\{&\frac{1}{2}A'(\alpha_t)(\boldsymbol{\varepsilon}(u_t)-\boldsymbol{\varepsilon}^v_t)\cdot(\boldsymbol{\varepsilon}(u)-\boldsymbol{\varepsilon}^v)\dot{\alpha}_t+\frac{1}{2}A'_v(\alpha_t)\boldsymbol{\varepsilon}^v_t\cdot\boldsymbol{\varepsilon}^v_t\dot{\alpha}_t+w'(\alpha)\dot{\alpha}_t+w_1\ell^2\nabla\alpha.\nabla\dot{\alpha}_t\\&+\frac{\Delta t}{2}\eta'(\alpha_t)\left(\frac{\|\boldsymbol{\varepsilon}^v_t-\boldsymbol{\varepsilon}^v_{t-1}\|}{\Delta t}\right)^2\dot{\alpha}_t+A(\alpha_t)(\boldsymbol{\varepsilon}(u_t)-\boldsymbol{\varepsilon}^v)\cdot\boldsymbol{\varepsilon}(\dot{u}_t)\\&-A(\alpha_t)(\boldsymbol{\varepsilon}(u_t)-\boldsymbol{\varepsilon}^v_t)\cdot\dot{\boldsymbol{\varepsilon}}^v+A_v(\alpha_t)\boldsymbol{\varepsilon}^v\cdot\dot{\boldsymbol{\varepsilon}}^v+\eta(\alpha_t)\left(\frac{\|\boldsymbol{\varepsilon}^v_t-\boldsymbol{\varepsilon}^v_{t-1}\|}{\Delta t}\right)\|\dot{\boldsymbol{\varepsilon}}^v\|\Bigg\}\mathrm{d}x\geq 0.\end{aligned} \tag{II.16}$$

Since the stress-strain law is

$$\boldsymbol{\sigma}_t = A(\alpha_t)(\boldsymbol{\varepsilon}(u_t) - \boldsymbol{\varepsilon}_t^v), \tag{II.17}$$

(II.16) becomes

$$\begin{aligned}\frac{\mathrm{d}\mathscr{E}}{\mathrm{d}t} = \int_\Omega \dot{\alpha}_t \left(\frac{1}{2}A'(\alpha_t)(\boldsymbol{\varepsilon}(u_t) - \boldsymbol{\varepsilon}_t^v)\cdot(\boldsymbol{\varepsilon}(u) - \boldsymbol{\varepsilon}^{\boldsymbol{v}}) + \frac{1}{2}A_v'(\alpha)\boldsymbol{\varepsilon}_t^v\cdot\boldsymbol{\varepsilon}_t^v + w'(\alpha) - w_1\ell^2\Delta\alpha \right.\\ \left. + \frac{\Delta t}{2}\eta'(\alpha)\left(\frac{\| \boldsymbol{\varepsilon}_t^v - \boldsymbol{\varepsilon}_{t-1}^v\|}{\Delta t}\right)\right)\mathrm{d}x + \int_{\partial\Omega}\frac{\partial\alpha}{\partial n}\dot{\alpha}\mathrm{d}s - \int_\Omega \mathrm{div}(\boldsymbol{\sigma}_t)\dot{u}_t\mathrm{d}x + \int_{\partial_D\Omega}\boldsymbol{\sigma}_t n\dot{u}_t\mathrm{d}s \\ + \int_\Omega \left\{(-\boldsymbol{\sigma}_t + A_v(\alpha_t)\boldsymbol{\varepsilon}^v)\cdot\dot{\boldsymbol{\varepsilon}}^v + \eta(\alpha_t)\left(\frac{\|\boldsymbol{\varepsilon}_t^v - \boldsymbol{\varepsilon}_{t-1}^v\|}{\Delta t}\right)\|\dot{\boldsymbol{\varepsilon}}^v\|\right\}\mathrm{d}x.\end{aligned} \tag{II.18}$$

Using (II.14), (II.18) simplifies into

$$\begin{aligned}\int_\Omega \dot{\alpha}_t \left(\frac{1}{2}A'(\alpha_t)(\boldsymbol{\varepsilon}(u_t) - \boldsymbol{\varepsilon}_t^v)\cdot(\boldsymbol{\varepsilon}(u_t) - \boldsymbol{\varepsilon}_t^v) + \frac{1}{2}A_v'(\alpha)\boldsymbol{\varepsilon}_t^v\cdot\boldsymbol{\varepsilon}_t^v + w'(\alpha_t) - w_1\ell^2\Delta\alpha_t \right.\\ \left. + \frac{\Delta t}{2}\eta'(\alpha_t)\left(\frac{\| \boldsymbol{\varepsilon}_t^v - \boldsymbol{\varepsilon}_{t-1}^v\|}{\Delta t}\right)\right)\mathrm{d}x + \int_{\partial\Omega}\frac{\partial\alpha}{\partial n}\dot{\alpha}\mathrm{d}s - \int_\Omega \mathrm{div}(\boldsymbol{\sigma}_t)\dot{u}_t\mathrm{d}x \\ + \int_\Omega \left\{(-\boldsymbol{\sigma}_t + A_v(\alpha_t)\boldsymbol{\varepsilon}_t^v)\cdot\dot{\boldsymbol{\varepsilon}}^v + \eta(\alpha_t)\left(\frac{\|\boldsymbol{\varepsilon}_t^v - \boldsymbol{\varepsilon}_{t-1}^v\|}{\Delta t}\right)\|\dot{\boldsymbol{\varepsilon}}^v\|\right\}\mathrm{d}x = 0.\end{aligned} \tag{II.19}$$

From (II.10), we have the equilibrium equation

$$\mathrm{div}(\boldsymbol{\sigma}) = 0, \tag{II.20}$$

that leads to

$$-\int_\Omega \mathrm{div}(\boldsymbol{\sigma}_t)\dot{u}_t\mathrm{d}x = 0. \tag{II.21}$$

There remains, making Δt goes to 0

$$\begin{aligned}\int_\Omega \dot{\alpha}_t \left(\frac{1}{2}A'(\alpha_t)(\boldsymbol{\varepsilon}(u_t) - \boldsymbol{\varepsilon}_t^v)\cdot(\boldsymbol{\varepsilon}(u_t) - \boldsymbol{\varepsilon}_t^v) + \frac{1}{2}A_v'(\alpha)\boldsymbol{\varepsilon}_t^v\cdot\boldsymbol{\varepsilon}_t^v + w'(\alpha_t) - w_1\ell^2\Delta\alpha_t\right)\mathrm{d}x \\ + \int_{\partial\Omega}\frac{\partial\alpha}{\partial n}\dot{\alpha}\mathrm{d}s + \int_\Omega \left((-\boldsymbol{\sigma}_t + A_v(\alpha_t)\boldsymbol{\varepsilon}_t^v)\cdot\dot{\boldsymbol{\varepsilon}}^v + \eta(\alpha_t)\|\dot{\boldsymbol{\varepsilon}}^v\|\|\dot{\boldsymbol{\varepsilon}}^v\|\right)\mathrm{d}x = 0.\end{aligned} \tag{II.22}$$

From the local damage criterion (II.8) and the irreversibility condition that enforces $\dot{\alpha} \geq 0$, we have

$$\int_\Omega \dot{\alpha}_t \left(\frac{1}{2}A'(\alpha_t)(\boldsymbol{\varepsilon}(u_t) - \boldsymbol{\varepsilon}_t^v)\cdot(\boldsymbol{\varepsilon}(u_t) - \boldsymbol{\varepsilon}_t^v) + \frac{1}{2}A_v'(\alpha)\boldsymbol{\varepsilon}_t^v\cdot\boldsymbol{\varepsilon}_t^v + w'(\alpha_t) - w_1\ell^2\Delta\alpha_t\right)\mathrm{d}x \geq 0. \tag{II.23}$$

It follows from (II.9) and the irreversibility condition that

$$\int_{\partial\Omega}\frac{\partial\alpha}{\partial n}\dot{\alpha}\mathrm{d}s \geq 0. \tag{II.24}$$

We now have to study the sign of

$$\int_\Omega ((-\boldsymbol{\sigma}_t + A_v(\alpha_t)\boldsymbol{\varepsilon}_t^v)\cdot\dot{\boldsymbol{\varepsilon}}^v + \eta(\alpha_t)\|\dot{\boldsymbol{\varepsilon}}^v\|\|\dot{\boldsymbol{\varepsilon}}^v\|)\,\mathrm{d}x. \tag{II.25}$$

Let us suppose that

$$(-\boldsymbol{\sigma}_t + A_v(\alpha_t)\boldsymbol{\varepsilon}_t^v)\cdot\dot{\boldsymbol{\varepsilon}}^v + \eta(\alpha_t)\|\dot{\boldsymbol{\varepsilon}}^v\|\|\dot{\boldsymbol{\varepsilon}}^v\| < 0. \tag{II.26}$$

From (II.13), we would have

$$\|-\boldsymbol{\sigma}_t + A_v(\alpha_t)\boldsymbol{\varepsilon}_t^v\|.\|\dot{\boldsymbol{\varepsilon}}^v\| + (-\boldsymbol{\sigma}_t + A_v(\alpha_t)\boldsymbol{\varepsilon}_t^v)\cdot\dot{\boldsymbol{\varepsilon}}^v < 0, \tag{II.27}$$

which means

$$1 + \frac{(-\boldsymbol{\sigma}_t + A_v(\alpha_t)\boldsymbol{\varepsilon}_t^v)\cdot\dot{\boldsymbol{\varepsilon}}^v}{\|-\boldsymbol{\sigma}_t + A_v(\alpha_t)\boldsymbol{\varepsilon}_t^v\|.\|\dot{\boldsymbol{\varepsilon}}^v\|} < 0. \tag{II.28}$$

$\|.\|$ being taken as an euclidean norm, this is impossible, hence the expression

$$(-\boldsymbol{\sigma}_t + A_v(\alpha_t)\boldsymbol{\varepsilon}_t^v)\cdot\dot{\boldsymbol{\varepsilon}}^v + \eta(\alpha_t)\|\dot{\boldsymbol{\varepsilon}}^v\|\|\dot{\boldsymbol{\varepsilon}}^v\| \geq 0. \tag{II.29}$$

The left-hand side of the equation (II.22) is composed only of positive or null terms, consequently there are necessarily null at the local level. This gives consistency conditions on the boundaries

$$\frac{\partial\alpha}{\partial n}\dot{\alpha} = 0 \quad \text{on } \partial\Omega, \tag{II.30}$$

and in the bulk

$$\dot{\alpha}_t\left(\frac{1}{2}A'(\alpha_t)(\boldsymbol{\varepsilon}(u_t) - \boldsymbol{\varepsilon}_t^v)\cdot(\boldsymbol{\varepsilon}(u_t) - \boldsymbol{\varepsilon}_t^v) + \frac{1}{2}A_v'(\alpha)\boldsymbol{\varepsilon}_t^v\cdot\boldsymbol{\varepsilon}_t^v + w'(\alpha_t) - w_1\ell^2\Delta\alpha_t\right) = 0 \quad \text{in } \Omega, \tag{II.31}$$

and also the expression

$$(-\boldsymbol{\sigma}_t + A_v(\alpha_t)\boldsymbol{\varepsilon}_t^v)\cdot\dot{\boldsymbol{\varepsilon}}^v + \eta(\alpha_t)\|\dot{\boldsymbol{\varepsilon}}^v\|\|\dot{\boldsymbol{\varepsilon}}^v\| = 0. \tag{II.32}$$

With the Cauchy-Schwartz inequality we have

$$-(-\boldsymbol{\sigma}_t + A_v(\alpha_t)\boldsymbol{\varepsilon}_t^v)\cdot\dot{\boldsymbol{\varepsilon}}^v \leq \|-\boldsymbol{\sigma}_t + A_v(\alpha_t)\boldsymbol{\varepsilon}_t^v\|\|\dot{\boldsymbol{\varepsilon}}^v\|, \tag{II.33}$$

which becomes using (II.32)

$$\eta(\alpha_t)\|\dot{\boldsymbol{\varepsilon}}^v\|\|\dot{\boldsymbol{\varepsilon}}^v\| \leq \|-\boldsymbol{\sigma}_t + A_v(\alpha_t)\boldsymbol{\varepsilon}_t^v\|\|\dot{\boldsymbol{\varepsilon}}^v\|. \tag{II.34}$$

Moreover, with (II.13), we get

$$\|-\boldsymbol{\sigma}_t + A_v(\alpha_t)\boldsymbol{\varepsilon}_t^v\| \;\leq\; \eta(\alpha_t)\|\dot{\boldsymbol{\varepsilon}}^v\| \;\leq\; \|-\boldsymbol{\sigma}_t + A_v(\alpha_t)\boldsymbol{\varepsilon}_t^v\| \tag{II.35}$$

and there is an equality in (II.35) to ensure (II.32). Equality in Cauchy-Schwartz is equivalent to the collinearity of $\dot{\boldsymbol{\varepsilon}}^v$ and $(-\boldsymbol{\sigma}_t + A_v(\alpha_t)\boldsymbol{\varepsilon}_t^v)$.

Finally, we have the equality

$$\|\dot{\boldsymbol{\varepsilon}}^v\| = \frac{\|-\boldsymbol{\sigma}_t + A_v(\alpha_t)\boldsymbol{\varepsilon}_t^v\|}{\eta(\alpha_t)} \tag{II.36}$$

which is the 3D evolution law of $\boldsymbol{\varepsilon^v}$,that can be qualified as optimal because it requires both the first order stability and the energy balance to be established.

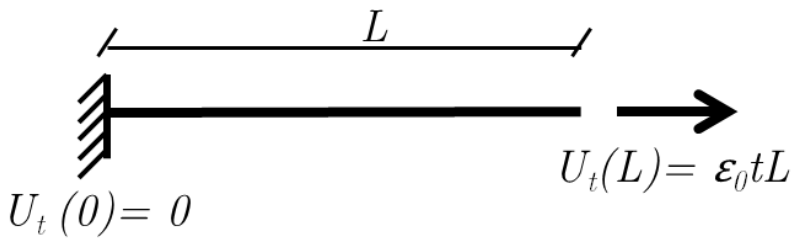

Figure II.2: 1D traction test with imposed displacement with constant loading speed ε_0.

II.1.2 Homogeneous damage

Let us consider a bar of length L such that the displacement in $x(0) = 0$ and $x(L) = \varepsilon_0 tL$. The damage field is chosen as a local field, which means that the damage in the bar is independent of the position x on which it is evaluated. We consequently have

$$\alpha_t'(x) = 0, \quad \forall x \in (0, L), \tag{II.37}$$

which leads to homogeneous fields of deformation

$$u_t'(x) = \varepsilon_0 t, \quad u_t(x) = \varepsilon_0 tx. \tag{II.38}$$

The damage law used for the rigidities of the springs is a softening one

$$A(\alpha) = A_0(1-\alpha)^2 \tag{II.39}$$

$$A_v(\alpha) = A_{v_0}(1-\alpha)^2, \tag{II.40}$$

and the dissipated energy density is chosen as linear

$$w(\alpha) = w_1\alpha. \tag{II.41}$$

The equations (II.8), (II.9), (II.10) and (II.36) obtained in II.1.1 give us the local damage criterion and boundary conditions on α

$$\frac{1}{2}A'(\alpha)(\varepsilon(u)-\varepsilon^v)^2 + \frac{1}{2}A_v'(\alpha)(\varepsilon^v)^2 + w'(\alpha) - w_1\ell^2\alpha'' \geq 0 \ \text{ in } \Omega \tag{II.42}$$

$$\frac{\partial\alpha}{\partial n} \geq 0 \ \text{ on } \partial\Omega \tag{II.43}$$

as well as the equilibrium equation $\sigma'(x) = 0,\ x \in (0, L)$ and the viscous evolution law of the material

$$\dot{\varepsilon}^v = \frac{\sigma - A_v(\alpha)\varepsilon^v}{\eta}. \tag{II.44}$$

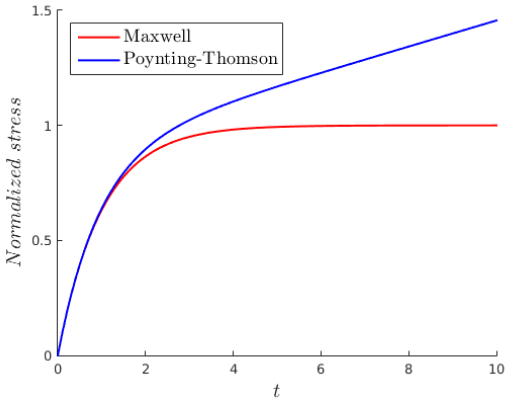

Figure II.3: Normalized stress response of a viscoelastic material submitted to a fixed speed loading. Both models have the same instantaneous elastic response, but only the Poynting-Thomson model has a deferred elastic response.

II.1.2.a Viscoelastic phase

In what follows, the study of the homogeneous damaging states is split into two parts: the first addresses the purely viscoelastic phase during which there is no damage occurring, while the second allows for damage to grow since the damage criterion is reached. By deriving with respect to time the expression

$$\sigma = A_0(\varepsilon - \varepsilon^v) \tag{II.45}$$

and injecting (II.44), we obtain the normalized equation

$$\frac{\eta}{A_0 + A_{v_0}}\dot{\sigma} + \sigma = \frac{A_0\eta}{A_0 + A_{v_0}}\dot{\varepsilon} + \frac{A_0 A_{v_0}}{A_0 + A_{v_0}}\varepsilon, \tag{II.46}$$

where $\varepsilon = t\varepsilon_0$, $\dot{\varepsilon} = \varepsilon_0$, and with the initial condition $\sigma(0) = 0$. Rewritting this equation $\tau_\varepsilon\dot{\sigma} + \sigma = A_\infty(\varepsilon + \tau_\sigma\dot{\varepsilon})$ and using the initial condition, we obtain

$$\sigma(t) = e^{-\frac{t}{\tau_\varepsilon}}\dot{\varepsilon}\left[\tau_\varepsilon A_\infty(1 - e^{\frac{t}{\tau_\varepsilon}}) + A_\infty(t + \tau_\sigma)e^{\frac{t}{\tau_\varepsilon}} - A_\infty\tau_\sigma\right], \tag{II.47}$$

where $\tau_\varepsilon = \dfrac{\eta}{A_0 + A_{v_0}}$, $A_\infty = \dfrac{A_0 A_{v_0}}{A_0 + A_{v_0}}$ and $\tau_\sigma = \dfrac{\eta}{A_{v_0}}$.

For the Maxwell model ($A_{v_0} = 0$), the stress in a bar submitted to a traction test with a constant speed loading ε_0 is

$$\sigma(t) = A_0\tau_0\varepsilon_0\left(1 - \exp\left(\frac{-t}{\tau_0}\right)\right), \tag{II.48}$$

where $\tau_0 = \eta/A_0$ is the characteristic time of the Maxwell model. This solution is visible on Figure II.3: the initial slope is $A_0\varepsilon_0$, there is therefore an instantaneous elastic response,

then when $t \to +\infty$, the stress goes to a fixed limit $\eta\varepsilon_0$.

In the case of the Poynting-Thomson model, there is an identical instantaneous elastic response, in which the secondary spring does not play any role, but there is also a deferred elastic response of module A_∞ that does not exist in the Maxwell model. When $t \to +\infty$, $\sigma(t)$ tends to an oblique asymptote of expression

$$A_\infty \varepsilon + A_\infty(\tau_\sigma - \tau_\varepsilon)\dot{\varepsilon}, \tag{II.49}$$

as shown on Figure II.3.

We now seek to determine whether there exists a time t_e at which the damage criterion is reached. To this end, we study, with respect to time,the damage criterion (II.42) written in stress, at $\alpha = 0$. We have

$$f(t) = -\frac{1}{2}S'(\alpha)\sigma^2 + w'(\alpha) - \frac{1}{2}S'_v(\alpha)(\varepsilon^v)^2, \tag{II.50}$$

where $S(\alpha) = A(\alpha)^{-1}$, $S_v(\alpha) = A_v(\alpha)^{-1}$, and $w(\alpha) = w_1\alpha$. We look for t_e such that $f(t_e) = 0$.

For the Maxwell model, (II.50) can be written

$$f(t) = w_1 - \frac{\sigma(t)^2}{A_0}, \tag{II.51}$$

where $\sigma(t)$ is given by (II.48). But σ is bounded by the value $\eta\varepsilon_0$. Consequently, there exists a time t_e for which the damage criterion is reached if the following condition holds

$$\varepsilon_0 > \frac{\sqrt{w_1 A_0}}{\eta}. \tag{II.52}$$

This can be seen on Figure II.4 where the damage criterion is plotted with respect to time for different loading speed. There exists a threshold to the loading speed, dependent on the model parameters, below which the material will never suffer any damage, whatever the time during which the traction is applied. The viscosity coefficient η has an influence on this threshold: if it is close to zero, the applied loading speed has to be infinite so that the material can be damaged. The physical interpretation is easy: no speed deformation, as big as it could be, can damage a perfect fluid. Conversely, when the viscosity of the material is large, a small deformation speed can be enough to damage it.

For the Poynting-Thomson model, we have

$$f(t) = w_1 - \frac{\sigma(t)^2}{A_0} - A_{v_0}(\varepsilon^v)^2, \tag{II.53}$$

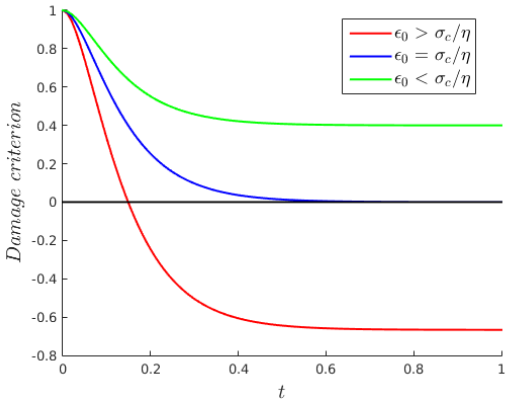

Figure II.4: Maxwell model. The damage criterion tends to a finite limit when time goes to infinity. If the speed loading is smaller than the threshold value (II.52)*, the damage criterion can never be reached.*

where $\sigma(t)$ is given by (II.47). The fundamental difference between the two rheological models, that is, the presence or not of a deferred elastic phase in the stress response of the material, triggers a different evolution of the damage criteria. In the Poynting-Thomson model, since the stress goes to infinity when $t \to +\infty$ (because it is an elastic phase), we see immediately that the damage criterion (II.53) goes to $-\infty$. Since $f(0) = w_1 > 0$, there always exists a time t_e such that the damage criterion is reached, whatever the value of the loading speed.

These results can also be interpreted using the properties of the models ([15] or [38]). The Maxwell model is sometimes referred to as the *viscoelastic fluid* model, because if a constant solicitation is applied, there is no possibility of equilibrium: for an example, during a creep test when a stress is applied on a non limited time, an elastic response is observed, that keeps growing. In this way, the material whose behaviour is modelled by a Maxwell model exhibits a typical property of Newtonian fluids, that is its capacity to deform indefinitely under a finite stress. On the contrary, the Kelvin-Voigt model which composes the Poynting-Thomson model is called viscoelastic solid, because the presence of an elastic phase in the end of a creep test makes it behaves nearly like a solid. The Poynting-Thomson model shows the same behaviour at infinity, and is therefore called *standard linear model* or *three parameters model*.

II.1.2.b Damaging phase

Critical stress and damaging time

In the case of the Maxwell model, the critical stress is

$$\sigma_c = \sqrt{w_1 A_0}. \tag{II.54}$$

We can see that σ_c does not depend on the viscosity coefficient neither on the loading speed, and is the same value as the one of a linear elastic material. The time at which damage begins is

$$t_e = -\tau_0 \ln\left(1 - \frac{\sigma_c}{\eta\varepsilon_0}\right), \tag{II.55}$$

and in this case, it depends on all the parameters of the model. The higher the loading speed, the quickest the material begins to damage. When the material is nearly fluid, t_e goes to infinity. Since II.52 has to be respected, t_e is always positive.

For the Poynting-Thomson model, it is more difficult to determine the critical stress because of the term in ε^v in the damage criterion. Let us note

$$p = \frac{A_{v_0}}{A_0}. \tag{II.56}$$

We write (II.42) with respect to stress, and we replace the expression of ε_v by $\left(\varepsilon - \dfrac{\sigma}{A_0(1-\alpha)^2}\right)$ in order to obtain σ as a function of α, t, and the parameters of the model

$$\sigma = \frac{1}{1+p}\left[\varepsilon A_{v_0}(1-\alpha)^2 + \sqrt{w_1(1-\alpha)^3(A_0+A_{v_0}) - \varepsilon^2 A_0 A_{v_0}(1-\alpha)^4}\right] \tag{II.57}$$

The critical stress is obtained with $\alpha = 0$ in (II.57)

$$\sigma_c = \frac{1}{1+p}\left[\varepsilon_e A_{v_0} + \sqrt{w_1(A_0+A_{v_0}) - \varepsilon_e^2 A_0 A_{v_0}}\right], \tag{II.58}$$

where $\varepsilon_e = t_e\varepsilon_0$.

Moreover, to be able to determine the time t_e from which the material begins to be damaged, the equality in the damage criterion (II.42) with $\alpha = 0$ written in stress has to be solved, which leads to

$$0 = w_1 - \frac{\sigma(t_e)^2}{A_0} - A_{v_0}\left(t_e\varepsilon_0 - \frac{\sigma(t_e)}{A_0}\right)^2 \tag{II.59}$$

where $\sigma(t_e)$ is the value of (II.47) for $t = t_e$. The numerical solution is plotted on Figure II.5a, where the total deformation at time t_e is $t_e\varepsilon_0$. This equation does not admit any analytical solution, therefore it is not possible to express σ_c with respect to the models parameters. Yet, we can still analyse some of its properties, in particular its values in the limiting cases of the loading speed. When ε_0 goes to zero, the critical stress goes to $A_{v_0}/(A_0 + A_{v_0})$ and the two rigidities of the springs matter. This is not the case when ε_0 goes to $+\infty$, since σ_c goes to the value of the critical stress in the Maxwell case. This means that only the main spring plays a role in this value, and this can be explained by the fact that if the loading speed is large, only the instantaneous elastic response has the sufficient time to intervene.

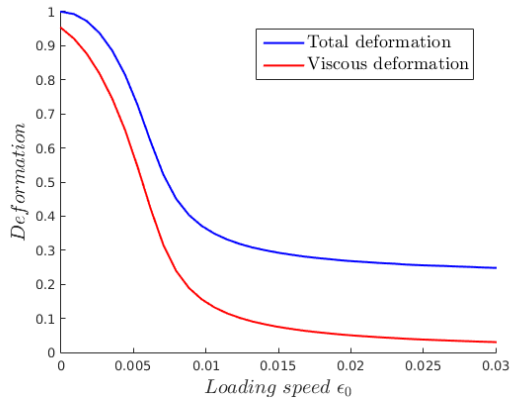

(a) Total deformation and viscous deformation.

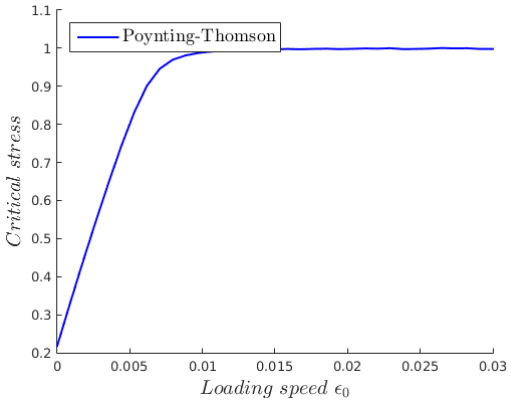

(b) Critical stress.

Figure II.5: Poynting-Thomson model. Values of the total and viscous deformation, and stress when the damage criterion is reached, with respect to the loading speed.

With the assumption that ε_e is monotonous with respect to ε_0, we can deduce that σ_c is also monotonous: it is consequently growing and bounded.

All this can be seen on Figure II.5b. Indeed, it shows clearly that the critical stress has two phases of evolution depending on the loading speed: in the first, it grows quickly, and can be approximated with a linear function of ε_0. Using (II.49) enables us to describe the behaviour of σ_c for large values of t_e, *i.e.* small values of ε_0. In this case, the critical stress can be approximated by the expression

$$\sigma_c \approx \sqrt{w_1 A_0}\sqrt{\frac{p}{1+p}} + \frac{\eta}{(1+p)^2}\varepsilon_0. \tag{II.60}$$

During the second phase, the critical stress becomes constant.

On Figure II.5a the evolution of the total deformation and the viscous deformation at time t_e is plotted with respect to the loading speed ε_0: when a traction with a slow speed loading is applied, the viscous deformation is quite big, and the viscous behaviour is predominant on the elastic behaviour. On the contrary, when the loading speed is high, the material gets damaged very quickly and the elastic deformation is important.

To summarize, we can again observe a difference with the Maxwell model: in the latter, the related critical stress is constant, whereas for the Poynting-Thomson model it depends on the loading speed. We can notice that σ_c takes only finite values because of a natural equilibrium between the critical values: when a very quick loading speed is applied on the bar, although the critical stress should go to infinity, it does not take an infinite value because the damaging time t_e goes to zero.

Evolution law of α

From now on, let us consider that the damage criterion has been reached, and let us look for the evolution law of the damage and the stress. Taking into account (II.39), the time derivative of (II.45) is

$$\dot{\sigma} = A_0 \left[-2\dot{\alpha}(1-\alpha)(\varepsilon - \varepsilon_v) + (1-\alpha)^2(\dot{\varepsilon} - \dot{\varepsilon}_v) \right]. \tag{II.61}$$

For the Maxwell model, the damage criterion written with respect to stress in which we inject the damage law (II.39) gives the expression of α and $\dot{\alpha}$ with respect to the stress and the model parameters. Injecting this expression in (II.61), we get the differential equation that govern the stress during the damaging phase and the initial condition

$$\begin{cases} \dot{\sigma}(t) = -3A_0 \left(\dfrac{\sigma(t)}{\sigma_c} \right)^{\frac{4}{3}} \left(\dot{\varepsilon} - \dfrac{\sigma(t)}{\eta} \right) \\ \sigma(0) = \sigma_c. \end{cases} \tag{II.62}$$

Writing $\tilde{t} = \dfrac{3A_0 \eta^{\frac{1}{3}} \varepsilon_0^{\frac{4}{3}}}{\sigma_c^{\frac{4}{3}}} t$, and $\tilde{\sigma} = \dfrac{\sigma}{\eta \varepsilon_0}$, we get the normalized and adimensionalized differential equation of $\tilde{\sigma}$ that governs the softening phase

$$\begin{cases} \dfrac{\mathrm{d}\tilde{\sigma}}{\mathrm{d}\tilde{t}} = -\tilde{\sigma}^{\frac{4}{3}}(1-\tilde{\sigma}) \\ \tilde{\sigma}(0) = \tilde{\sigma}_c. \end{cases} \tag{II.63}$$

This autonomous differential equation admits two stationary solutions, $\tilde{\sigma} : \tilde{t} \mapsto 0$ and $\tilde{\sigma} : \tilde{t} \mapsto 1$. For initial conditions $\tilde{\sigma}(0) \in]0,1[, \dot{\tilde{\sigma}} < 0$ so the function $\tilde{\sigma} : \tilde{t} \mapsto \tilde{\sigma}(t)$ is strictly decreasing on $[0, +\infty[$ and is bounded by 0. For initial conditions strictly superior to 1, the function is strictly increasing and goes to $+\infty$. Figure II.6a shows solutions of (II.63) for different initial conditions in $]0,1[$.

In order that the material be damaged, the material parameters have to follow the condition (II.52). This means that we always have $\tilde{\sigma}(0) < 1$, and the solution of the differential equation can only be a decreasing function of time that goes to zero.

On Figure II.6b, the stress response of a damaging viscoelastic material is plotted, for different values of σ_c. When σ_c is small, the time t_e is also small, and we see that on the value of σ_c depends the shape of the softening phase. When the critical stress gets close to the value $\eta\varepsilon_0$, a stress plateau appears, and the closest to this value, the largest the plateau. When $\sigma_c = \eta\varepsilon_0$, we go back to the purely viscoelastic solution.

The Poynting-Thomson model is dealt with slightly differently, because the differential equation established is the one which governs the evolution of α rather than the one of σ. We introduce the notation

$$r = \sqrt{w_1(1-\alpha)^3(A_0 + A_{v_0}) - \varepsilon^2 A_0 A_{v_0}(1-\alpha)^4}. \tag{II.64}$$

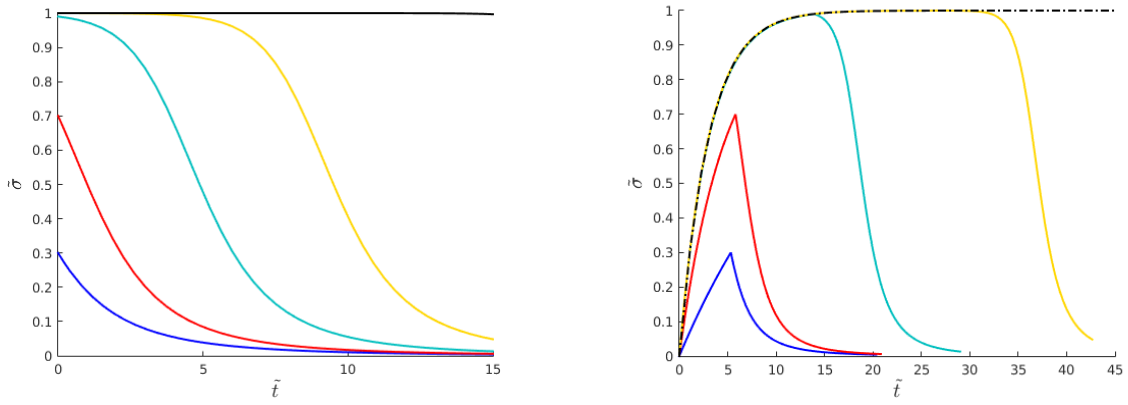

(a) Solution of the adimensionalized equation (II.63).

(b) Adimensionalized stress softening for different σ_c.

Figure II.6: Maxwell model. Homogeneous damage evolution: damaging phase (left) and viscoelastic followed by damaging phase (right). When the value of σ_c gets close to $\eta\varepsilon_0$, a stress plateau appears.

Deriving with respect to time (II.57) and injecting the expression of $\dot{\sigma}$ in the expression of the derivative of the stress/strain relation (II.61) gives a non autonomous differential equation that governs the evolution of α

$$\dot{\alpha} = \frac{\dfrac{A_{v_0}}{1+p}\varepsilon_0\left(-(1-\alpha)^2 + \dfrac{\varepsilon A_0(1-\alpha)^4}{r}\right) + A_0(1-\alpha)^2\left(\varepsilon_0 - \dfrac{r}{\eta}\right)}{\dfrac{1}{1+p}\left(-2(1-\alpha)\varepsilon A_{v_0} + \dfrac{-3w_1(1-\alpha)^2(A_0+A_{v_0}) + 4(1-\alpha)^3\varepsilon^2 A_0 A_{v_0}}{2r} + \dfrac{2(\varepsilon A_{v_0}(1-\alpha)^2 + r)}{1-\alpha}\right)}, \tag{II.65}$$

where r is given by (II.64), $\varepsilon = t\varepsilon_0$, and $p = \dfrac{A_{v_0}}{A_0}$.

Similarly as for the Maxwell model, we normalize and adimensionalize the equation (II.65) in order to be able to study it more easily. We write

$$w_1 = \frac{\eta^2\varepsilon_0^2}{A_0(1+p)}\tilde{k}, \tag{II.66}$$

and

$$t = \frac{\eta}{A_0(1+p)}\tilde{t}. \tag{II.67}$$

Therefore

$$\sigma = \frac{\eta\varepsilon_0}{1+p}\tilde{\sigma}, \tag{II.68}$$

where

$$\tilde{\sigma} = \frac{p}{1+p}\tilde{t}(1-\alpha)^2 + \tilde{r}, \tag{II.69}$$

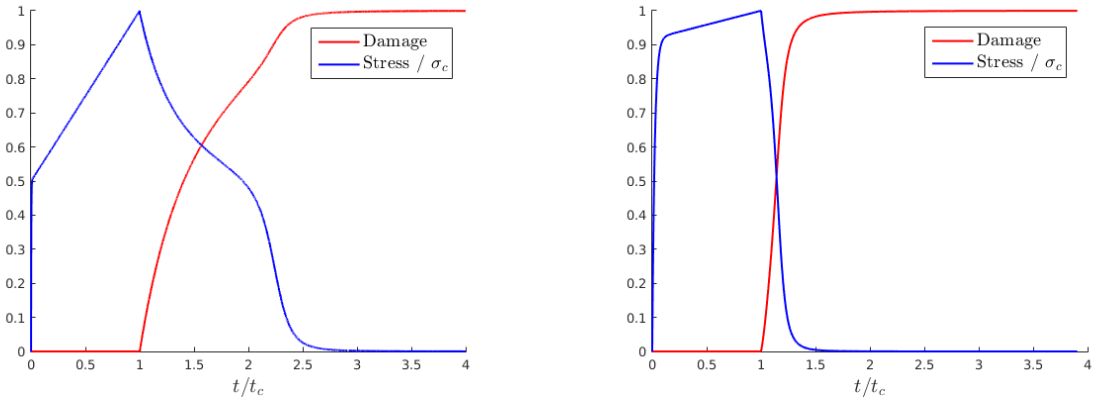

(a) (b)

Figure II.7: Poynting-Thomson model. Homogeneous damage evolution and stress evolution for two different values of σ_c: on the left, σ_c is ten times higher than σ_c on the right.

and

$$\tilde{r} = \sqrt{\tilde{k}(1-\alpha)^3 - \frac{p}{(1+p)^2}\tilde{t}^2(1-\alpha)^4}. \tag{II.70}$$

Inserting these variable changes in (II.65), we get

$$\frac{\mathrm{d}\alpha}{\mathrm{d}\tilde{t}} = \frac{2}{1+p}\frac{\tilde{\sigma} - (1+p)\tilde{r}^2}{\tilde{k}}. \tag{II.71}$$

Unlike the Maxwell model, this equation cannot be studied analytically. We can yet notice that if $\tilde{\sigma} - (1+p)\tilde{r}^2 \leq 0$ when $t = t_e$, $\dot{\alpha}$ will not be positive. Since this phenomenon is not physically acceptable because it violates the irreversibility condition, we suppose that there are some temporal discontinuities in the evolution of α.

Finally, we can see that this equation is not autonomous, *i.e.* that its solutions will depend on the time t_e at which the initial condition is fixed. We will thus not observe stationary solutions as were seen with the Maxwell model. Indeed, since for large time the material is again following an elastic evolution, the stress grows linearly.

The equation (II.65) can be solved numerically, as can be (II.71) with the initial condition $\alpha(t_e) = 0$, and we can deduce $\sigma(t)$ with (II.57). On Figure II.7 we plot the damage and stress evolution for two different values of σ_c: in the first case, the critical value of the stress is 10 times the value of the second case, and we can see that this difference induces different responses over the time.

II.1.3 Damage localisation

In this section, we no longer assume a homogeneous field of damage. From now on, the spatial derivative of α will not be null any more. The previous calculations have to be done

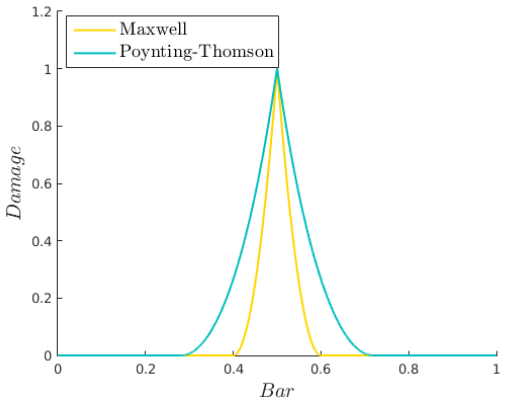

Figure II.8: Damage profiles for Maxwell and Poynting-Thsomson model. The width of the damage profile is greater for the Poynting-Thomson model.

again, assuming this time that the damage localises on the bar. The differences induced by the use of the two rheological models will be highlighted, in the expressions of the damage profiles as well as in the expression of the dissipated energy.

Let us consider the bar of length L on which a traction with constant loading speed ε_0 is applied on one end. Let us assume that the damage localises on a finite interval of the bar, centered in X_0, and of width $2d$.

II.1.3.a Damage profiles

Maxwell model

For the Maxwell model, we write the damage criterion (II.42) with respect to stress on the interval $(X_0 - d, X_0 + d)$

$$0 = -\frac{\sigma^2}{A_0(1-\alpha)^3} + w_1 - w_1 \ell^2 \alpha''. \tag{II.72}$$

We see in this formulation that when the damage criterion is written in the stress space, the viscosity does not play any role: thus, the damage criterion is the same as in linear elasticity. Consequently, the damage profiles are the same as in elasticity, and the width of the damage band $2d$ is also the same. The only difference lies in the evolution of the stress since one is linear (Hooke's law), and the other is not due to the viscosity. Note that a particularity of the Maxwell model imposes that the loading speed be greater than a threshold value so that the localisation can arise.

Poynting-Thomson model

As was done for the Maxwell model, we write the local damage criterion (II.42) with respect to the stress on $(X_0 - d, X_0 + d)$

$$0 = -\frac{1}{2}S'(\alpha)\sigma^2 + \frac{1}{2}A'_v(\alpha)(\varepsilon^v)^2 + w'(\alpha) - w_1\ell^2\alpha''. \tag{II.73}$$

In the case of the Poynting-Thomson model, this criterion has an additional term which involves the viscous deformation ε^v. At this point, we make the assumption that the damage localises suddenly at time t_{loc}, so that the viscous deformation does not have time to localise, and keeps the value it had just before the localisation happened. The value of the viscous deformation at time t_{loc} can be numerically computed with the formula

$$\varepsilon^v(t_{loc}) = \exp\left(-\int_0^{t_{loc}} \frac{A_{v_0}}{\eta}(1-\alpha(t))^2 \,\mathrm{d}t\right)\left[\int_0^{t_{loc}} \frac{\sigma(s)}{\eta}\exp\left(\int_0^s \frac{A_{v_0}}{\eta}(1-\alpha(t))^2 \,\mathrm{d}t\right)\mathrm{d}s\right]. \tag{II.74}$$

The damage profile around X_0 is given by the solution of the differential equation

$$0 = -\frac{1}{2}S'(\alpha)\sigma^2 + \frac{1}{2}A'_v(\alpha)(\varepsilon^v)^2 + w'(\alpha) - w_1\ell^2\alpha'', \tag{II.75}$$

also written

$$0 = -\frac{\sigma^2}{A_0(1-\alpha)^3} - A_{v_0}(1-\alpha)(\varepsilon^v)^2 + w_1 - w_1\ell^2\alpha''. \tag{II.76}$$

When the bar is broken, $\sigma = 0$, and we have

$$0 = -A_{v_0}(1-\alpha)\varepsilon^{v^2} + w_1 - w_1\ell^2\alpha'' \tag{II.77}$$

that is rewritten

$$\alpha'' - \omega^2\alpha = K, \tag{II.78}$$

where $\omega^2 = \dfrac{A_{v_0}\varepsilon^{v^2}}{w_1\ell^2}$ and $K = \dfrac{-A_{v_0}\varepsilon^{v^2} + w_1}{w_1\ell^2}$.
At the ends of the localisation, the boundary conditions are as follows

$$\begin{cases} \alpha(X_0 \pm d) = & \alpha_0 \\ \alpha'(X_0 \pm d) = & 0. \end{cases} \tag{II.79}$$

Then the solution of (II.78) is such that

$$\alpha(x) = -\frac{K}{\omega^2} + C_1\exp(x\omega) + C_2\exp(-x\omega), \tag{II.80}$$

with C_1 and C_2 two constants determined with the boundary conditions. In the end, we have

$$\begin{cases} \alpha(x) = \dfrac{K}{\omega^2} + \left(\alpha_0 + \dfrac{K}{\omega^2}\right)\cosh\left[\omega(x - X_0 - d\dfrac{x - X_0}{\mid x - X_0 \mid})\right] & \text{on } (X_0 - d, X_0 + d) \\ \alpha(x) = \alpha_0 & \text{on } (0,1) \setminus (X_0 - d, X_0 + d) \end{cases} \tag{II.81}$$

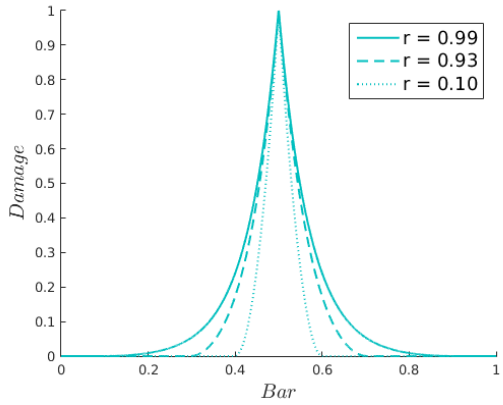

(a) Poynting-Thomson model. Damage profiles for different values of viscous deformation at time t_e: $r = \varepsilon^v/\sqrt{w_1/Ev_0}$.

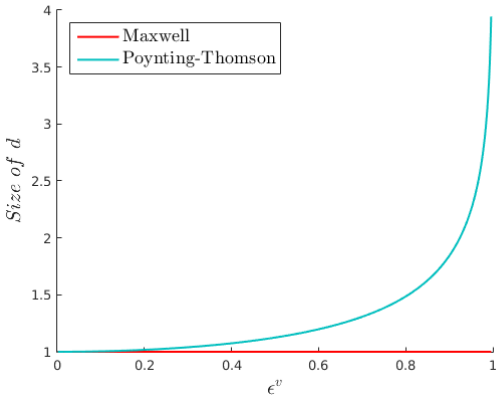

(b) Evolution of the damage width band d with respect to the viscous deformation at time t_e

Figure II.9: Poynting-Thomson model. Damage width band and localisations for different values of ε^v, without a homogeneous damaging phase. The closer to the value $\sqrt{w_1/Ev_0}$ the viscous deformation is, the wider is the damage profile.

The constant d is such that $\alpha(X_0) = 1$, and

$$d = \frac{1}{\omega}\text{argch}\left(\frac{K+\omega^2}{K+\alpha_0\omega^2}\right) \tag{II.82}$$

with the condition

$$(\varepsilon^v(t_{loc}))^2(1-\alpha_0) \leq \frac{w_1}{E_{v_0}} \tag{II.83}$$

where t_{loc} is the time when the damage localises. We have seen previously that the value of $\varepsilon^v(t_e)$ depends on the loading speed. The condition (II.83) is therefore a condition on ε_0, and we find the same type as conditions as was found for the Maxwell model. Both Maxwell and Poynting-Thomson models imply a condition on the loading speed: there exists a threshold below which the damage cannot develop (Maxwell) or localise (Poynting-Thomson). This phenomenon does not exist in linear elasticity.

As shown with equation (II.82), the value of the damage width band depends on the value of ε^v when the damage localises. Deriving the expression $\varepsilon^v \mapsto d(\varepsilon^v)$ with respect to ε^v shows that $d(\varepsilon^v)$ is strictly growing: when ε^v increases, and therefore ε_0 decreases, d becomes wider, as shown on Figure II.9. The limit of $d(\varepsilon^v)$ when ε^v goes to $\sqrt{w_1/A_{v_0}}$ is $+\infty$: the damage width band has to be infinite so that the damage can reach the value 1 in the centre, and the bar can break. To circumvent this problem, the value of α_0 has to be big enough.

We can notice, using l'Hôpital's rule, that when $\varepsilon^v \to 0$, the function $\varepsilon^v \mapsto d(\varepsilon^v)$ goes to $\sqrt{2}\ell$, which is the value of the damage half width band in small deformation.

Whatever the value of ε^v that enables the damage to localise, the damage width band with the Poynting-Thomson model is always greater than the one with the Maxwell model. When ε^v goes to 0, the damage profile goes to the damage profile of the Maxwell model.

II.1.3.b Rupture energy

The rupture energy is the integral over the damage band of the dissipated energy when a crack has appeared. For the Maxwell model, the damage width band $2d$ is the same as for linear elastic material. Moreover, when a crack has developed in the bar, there remains only the dissipated energy, and the viscous energy as well as the elastic energy do not play any role. Consequently, the rupture energy G_c is the same for a Maxwell material or a linear elastic material.

For the Poynting-Thomson model, we have seen previously that the damage width band takes values that are always superior to the values of the Maxwell model. Since the rupture energy is the integral over the damaged region of the damage dissipated energy, it can only be greater or equal to the dissipated energy obtained with the Maxwell model.

II.1.4 Numerical implementation

The last part of this study of damaging viscoelastic materials in 1D consists in the numerical implementation of the models. The FEniCS library is used, as well as the usual strategy of alternate minimization. A bar of length L is discretized in N elements, a time span $(0, T)$ is also discretized. The spaces in which the three unknowns live are chosen such that the damage α and the displacement u are Lagrange functions of order 1, and the viscous strain ε^v is a discontinuous function on the elements.

The alternate minimization has to take into account the introduction of a new variable, ε^v, and so for each time step, three problems are successively solved, as shown in the algorithm below.

- **Initialization** at time t_i
  $(u_{old}, \alpha_{old}, \varepsilon^v_{old}) = (u_{i-1}, \alpha_{i-1}, \varepsilon^v_{i-1})$
- **Repeat** until $\|\alpha_{new} - \alpha_{old}\| < \text{tol}$
  1. $\varepsilon^v_{new} = \arg\min_{\varepsilon^v} \mathscr{E}(u_{old}, \alpha_{old}, \varepsilon^v)$
  2. $u_{new} = \arg\min_{u} \mathscr{E}(u, \alpha_{old}, \varepsilon^v_{new})$
  3. $\alpha_{new} = \arg\min_{\alpha} \mathscr{E}(u_{new}, \alpha, \varepsilon^v_{new})$
- **Update** $(u_i, \alpha_i, \varepsilon^v_i) = (u_{new}, \alpha_{new}, \varepsilon^v_{new})$

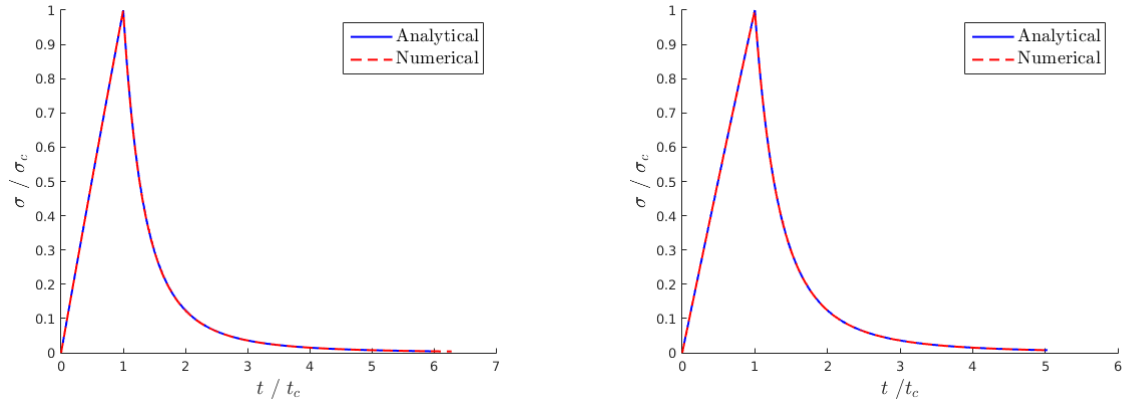

(a) Maxwell model *(b) Poynting-Thomson model*

Figure II.10: Evolution of homogeneous damage for both viscoelastic models. The numerical and theoretical results match perfectly.

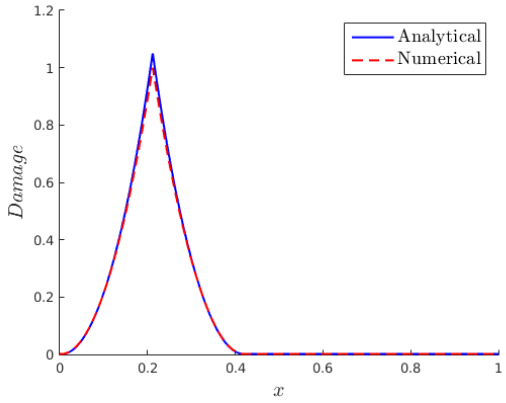

Figure II.11: Poynting-Thomson model. Superposition of analytical and numerical solutions for the localisation of damage. In this case, the homogeneous damaging phase is negligible.

Homogeneous response

The homogeneous response of the two rheological models are tested. For this, a sufficiently large internal length has to be chosen, in order to ensure a homogeneous field of damage on the bar. There are no boundary conditions on α. The responses are plotted on Figure II.10, and we can see that the analytical and numerical solutions match perfectly, for both the viscoelastic phase and the damaging phase. After reaching a critical value of stress, the stress decreases until it reaches zero and the bar is broken.

Localised response

Once the results have been checked in the case of homogeneous fields, we study the localisation of damage. In the case of the Maxwell model, the damage profiles match perfectly,

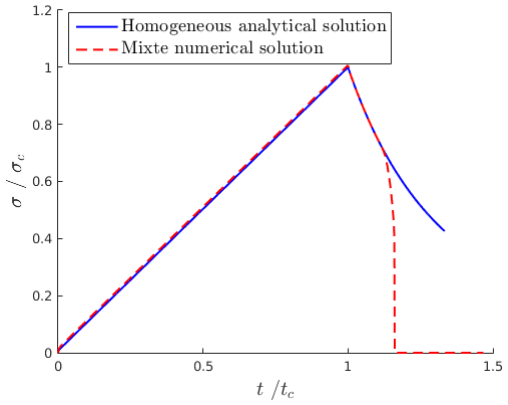

(a) Evolution of stress with respect to time. Comparison of analytical and numerical results.

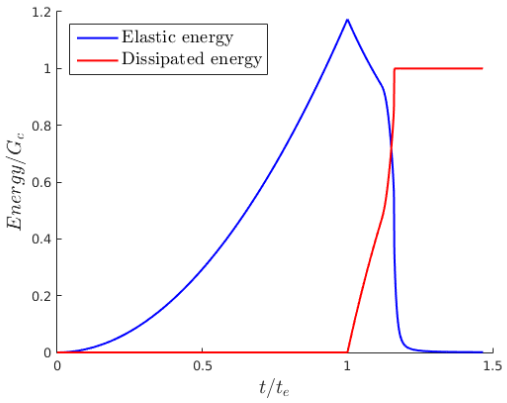

(b) Evolution of elastic and dissipated energies with respect to time.

Figure II.12: Poynting-Thomson model. A homogeneous damaging phase is followed by a localisation of damage.

providing that the loading speed is great enough to trigger damage in the bar. In the case of the Poynting-Thomson model, it is a little more tricky: indeed, the breaking of the bar happens in three phases. There is first a phase of viscoelastic deformation, followed by a phase of homogeneous damage on the bar, until the damage suddenly localises. Due to this homogeneous phase of damage, the boundary conditions on α (Dirichlet boundary conditions of zero damage) that are usually set in order to ensure the localisation on the bar have to be disabled. But because of this, due to numerical considerations, the damage localises on the boundaries and only half a damage profile is obtained. To compensate for this, periodic boundary conditions are used on the damage variable, so that even if half a damage profile grows on the boundaries, the other half will grow on the other boundary.

Figure II.11 shows a case when the homogeneous phase of damage is very fast, and thus the damage α_0 is negligible compared to the damage profile. The numerical simulation has been performed using the following parameters: $\varepsilon_0 = 2.5$, $w_1 = 3.75$, $A_0 = 10$, $Av_0 = 2$, $\eta = 3$. The analytical solution has been plotted using the formula (II.81) and the parameters $d = 0.207$, $\alpha_0 = 0.0016$, $\varepsilon^v = 0.401$. In this case, the analytical expression of the damage profile after rupture corresponds well to the numerical solution.

A second case is when the homogeneous phase that precedes the localisation of damage is not negligible. To obtain such a long phase, the loading speed has to be taken very low. Figure II.12 shows the evolution of the stress and the energies with respect to time in such a situation. The parameters that were used are the following: $\varepsilon_0 = 0.0088$, $w_1 = 3.75$, $A_0 = 10$, $Av_0 = 2$, $\eta = 3$. The viscoelastic phase matches the analytical calculations, and the homogeneous phase is also the same as the one calculated analytically. But we can see that at some point, the homogeneous phase becomes unstable and the localisation appears.

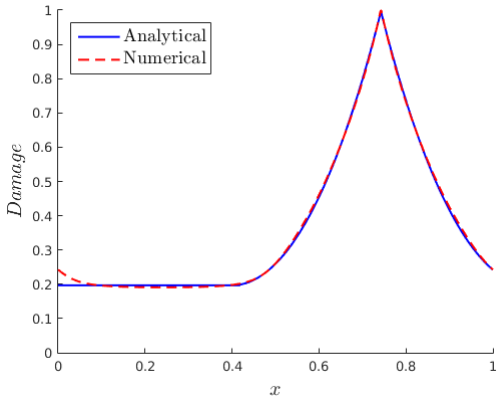

(a) Comparison of analytical and numerical damage profiles.

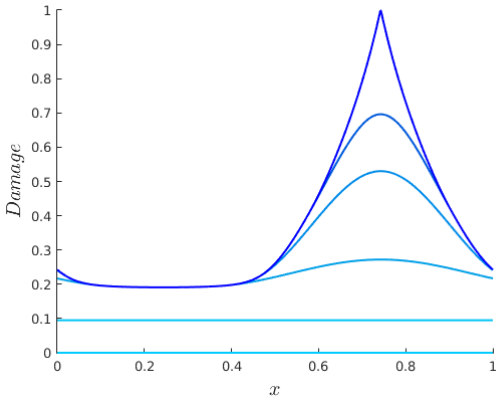

(b) Development of the damage profile for different time steps.

Figure II.13: Poyting-Thomson model. A homogeneous damaging phase is followed by a localisation of damage.

Unlike the previous case shown on Figure II.11 where the damage width band is 40% of the bar, for the same internal length, but a different loading speed, the damage width band in this case is of 60% (Figure II.13a). As was established analytically, the damage support depends on the loading speed. Not only is the damage width band larger, but the localisation arises in a very different way. In a purely elastic case, with the models used here, the localisation of damage is a brutal process: at some given load, the damage suddenly localises, which causes the energy to jump. In this case, as can be seen on Figure II.13b, the localisation of damage is nearly a continuous process, and there is a small energy jump when the bar becomes fully broken (Figure II.12b).

Due to this non brutal localisation, the assumption whereby the viscous deformation does not have time to localise on the bar when the damage localises is no valid any more. This is why on Figure II.13a the analytical results are plotted using a value of ε^v found by parameter fitting. Despite this, the numerical and analytical results match well in this case.

II.2 Damage and hyperelasticity

In this part, we use the framework of large deformation to have a first view of the relevance of the gradient damage models in large deformation. The notations will be introduce as we go along the calculations, but we still give the main notations now. The gradient deformation tensor is written $\boldsymbol{F}$. The Green-Lagrange deformation is written $\boldsymbol{E}$. Depending on the need, different stress tensors are used. The second Piola-Kirchhoff stress is written $\boldsymbol{S}$, the first Piola-Kirchhoff stress $\boldsymbol{\Pi}$, the Kirchhoff stress $\boldsymbol{\tau}$, and the Cauchy stress $\boldsymbol{\sigma}$.

II.2.1 Unidimensional hyperelastic potential

Construction in dimension 3

In large deformation, the most elementary hyperelastic model is the one of Saint-Venant Kirchhoff which consists in writing the elastic energy in terms of Green-Lagrange deformation instead of the linearised deformation tensor. Yet, this simple model induces drawbacks, for physical as well as numerical reasons. This is why we will use the model of Ciarlet-Geymonat [12], which is an extension of this Saint-Venant Kirchhoff model, but enables to overcome its faults.

The construction of this law lays on several criteria: it has to be polyconvex to ensure the existence of minimizers ([6]), to reduce to small deformation

$$\psi(\boldsymbol{F}) = \frac{\lambda}{2}(\mathrm{tr}\boldsymbol{E})^2 + \mu \mathrm{tr}(\boldsymbol{E}^2) + O(\|\boldsymbol{E}\|^3), \tag{II.84}$$

to prevent the reduction of a volume to zero without any cost of energy

$$\psi(\boldsymbol{F}) \to +\infty \quad \text{when} \quad \det(\boldsymbol{F}) \to 0^+, \tag{II.85}$$

and to be coercive

$$\psi(\boldsymbol{F}) \geq (\|\boldsymbol{F}\| + \|\mathrm{cof}\boldsymbol{F}\| + \det \boldsymbol{F}) \tag{II.86}$$

where $\|\mathrm{cof}\boldsymbol{F}\| = \mathrm{tr}(\mathrm{cof}\boldsymbol{F}^T \cdot \boldsymbol{F}) = \frac{1}{2}\left[(\mathrm{tr}\boldsymbol{F}^T \cdot \boldsymbol{F})^2 - \mathrm{tr}(\boldsymbol{F}^T \cdot \boldsymbol{F})^2\right]$. Starting from a general expression of a law that follows the previous conditions (II.84), (II.85), (II.86)

$$\psi(\boldsymbol{F}) = a\|\boldsymbol{F}\|^2 + b\|\mathrm{cof}\boldsymbol{F}\|^2 + c(\det \boldsymbol{F})^2 - d\ln(\det \boldsymbol{F})^2 + e, \tag{II.87}$$

with a, b, c, d and e real constants, the development of this expression leads to the 3D formulation of the Ciarlet-Geymonat potential

$$\psi(\boldsymbol{E}) = (\frac{\lambda}{2} + \mu)\mathrm{tr}(\boldsymbol{E}) + \frac{\lambda}{2}\left[\mathrm{tr}^2(\boldsymbol{E}) - \mathrm{tr}(\boldsymbol{E}^2)\right] + 8c\det(\boldsymbol{E}) - \frac{\lambda + 2\mu}{4}\ln\det(1 + 2\boldsymbol{E}), \tag{II.88}$$

where λ and μ are the Lamé coefficients, and c a material constant strictly positive, following the condition $c = \frac{1}{4}(\Gamma'(1) + \Gamma''(1))$, $\Gamma'(1) \in \left]-\frac{\lambda}{2} - \mu, -\mu\right[$ and $\Gamma''(1) \in \left]\frac{\lambda}{2} + \mu, \lambda + \mu\right[$.

Reduction to dimension 1

Since (II.88) was constructed for 3D specifically, we have to go back to (II.87) and write it in 1D

$$\psi(F) = (a + c)F^2 - d\ln F^2 + e. \tag{II.89}$$

We develop $\ln F^2$ up to the second order with $F^2 = 1 + 2E$

$$\ln F^2 = 2E - \frac{(2E)^2}{2} + O(|E|^3). \tag{II.90}$$

Condition (II.84) gives

$$(a+c)(1+2E) - d(2E-2E^2) + e = \frac{A}{2}E^2, \tag{II.91}$$

and we get by identification

$$a + c = d = -e = \frac{A}{4}. \tag{II.92}$$

In 1D, the hyperelastic potential reduces to

$$\psi(F) = \frac{A}{2}\left(E - \frac{1}{2}\ln(1+2E)\right), \tag{II.93}$$

For small deformation, the development of $\ln(1+2E) = 2\ln(1+u')$ around 0 gives an approximation of the energy density that matches the Hooke's law

$$\psi(F) = \frac{A}{2}u'^2, \tag{II.94}$$

while for large deformation, $u' \ll u'^2$ and $ln(1+u') \ll u'^2$, give a quadratic potential

$$\psi(F) = \frac{A}{2}\frac{u'^2}{2}. \tag{II.95}$$

The second Piola-Kirchhoff stress is

$$S = \frac{A}{2}\frac{2E}{1+2E}, \tag{II.96}$$

In 3D, the Cauchy stress is linked to the second Piola-Kirchhoff stress $\boldsymbol{S}$ by the relation

$$\boldsymbol{\sigma} = \frac{1}{J}\boldsymbol{F}^T\boldsymbol{S}\boldsymbol{F} \tag{II.97}$$

and so, in 1D, with a Ciarlet-Geymonat potential, we have

$$\sigma = \frac{A}{2}\frac{\sqrt{1+2E}}{1+2E}2E \tag{II.98}$$

also written

$$\sigma = \frac{A}{2}(1+u') - \frac{A}{2}\frac{1}{1+u'}. \tag{II.99}$$

II.2.2 Homogeneous damage evolution in a 1D hyperelastic bar

Keeping the relation between the damage and the rigidity as previously defined $A(\alpha) = A_0(1-\alpha)^2$, we can write the total energy of the system. Note that since we are now working in the framework of large deformation, we have to chose in which configuration we want to work, *i.e.* in the reference (initial) or the deformed (actual) configuration. We will come

back to it later, but let us chose to work in the reference configuration $\mathscr{C}_0$ for now. The total energy of the system is

$$\mathscr{E}(u,\alpha) = \int_{\Omega_0} \left(\frac{A(\alpha)}{2}(u' + \frac{u'^2}{2}) - \frac{A(\alpha)}{4}\ln(1+u')^2 + w(\alpha) + \frac{1}{2}w_1\ell^2(\alpha')^2 \right) \mathrm{d}X, \tag{II.100}$$

that is derived in the admissible directions $(v,\beta) \in \mathcal{C}_0 \times \mathcal{D}_t$

$$\begin{aligned}\mathscr{E}'(u,\alpha)(v,\beta) = &\int_{\Omega_0} \left(\frac{A(\alpha)}{2}(1+u')v' - \frac{A(\alpha)}{2}\frac{v'}{1+u'} \right) \mathrm{d}X \\ &+ \int_{\Omega_0} \left(\frac{A'(\alpha)}{2}(u' + \frac{u'^2}{2})\beta - \frac{A'(\alpha)}{2}\ln(1+u')\beta + w'(\alpha)\beta + w_1\ell^2\alpha'\beta' \right) \mathrm{d}X.\end{aligned} \tag{II.101}$$

Using the first stability criterion, and taking $\beta = 0$, we get

$$\int_{\Omega_0} \left(\frac{A(\alpha)}{2}(1+u')v' - \frac{A(\alpha)}{2}\frac{v'}{1+u'} \right) \mathrm{d}X = 0 \quad \forall v \in \mathcal{C}_0, \tag{II.102}$$

and after integrating by part we obtain the equilibrium equation

$$\Pi'(X) = 0, \ X \in (0,L). \tag{II.103}$$

$v = 0$ gives the damage criterion for a hyperelastic material of Ciarlet-Geymonat

$$\frac{A'(\alpha)}{2}\left(u' + \frac{u'^2}{2} - \ln(1+u') \right) + w'(\alpha) - w_1\ell^2\alpha'' \geq 0, \tag{II.104}$$

that is rewritten

$$\frac{A'(\alpha)}{2}\left(E - \frac{1}{2}\ln(1+2E) \right) + w'(\alpha) - w_1\ell^2\alpha'' \geq 0. \tag{II.105}$$

We write this damage criterion with respect to time for $\alpha = 0$, with $u' = t\varepsilon_0$

$$f(t) = -\frac{A_0}{2}\left(t\varepsilon_0 + \frac{(t\varepsilon_0)^2}{2} - \ln(1+t\varepsilon_0) \right) + w_1. \tag{II.106}$$

We have

$$f'(t) = -\frac{A_0}{2}\left(\frac{t\varepsilon_0^2(2+t\varepsilon_0)}{1+t\varepsilon_0} \right) \leq 0, \quad t \geq 0. \tag{II.107}$$

Since $f(t)$ is a decreasing function of time, the damage criterion is always reached. Because of the presence of the logarithm, it is not possible to determine the expression of t_e nor σ_c.

Now we study the homogeneous damaging phase of the material. We write the damage criterion (II.105) in the case of the equality, and we deduce the expression of α with respect to the Green-Lagrange deformation.

$$\alpha = 1 - \frac{w_1}{\frac{A_0}{2}\left(E - \frac{1}{2}\ln(1+2E) \right)} \tag{II.108}$$

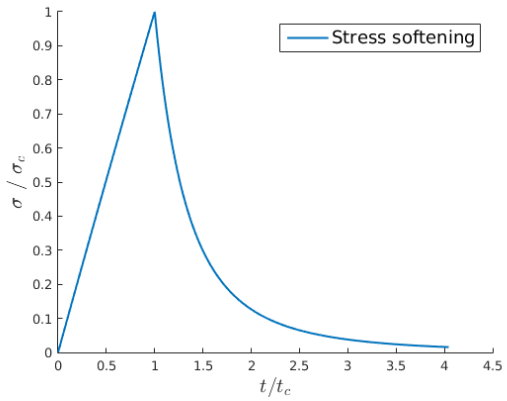

(a) Stress evolution: a hyperelastic phase is followed by a softening phase after the critical stress value has been reached.

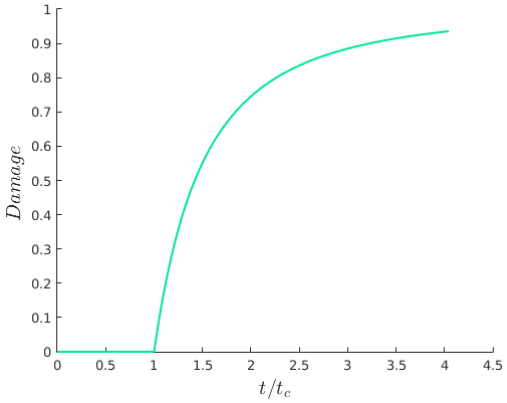

(b) Damage evolution: it is null during the hyperelastic phase, and begins to grow at time t_c and tends to the value one.

Figure II.14: Poynting-Thomson model. Homogeneous damage evolution.

We inject this expression in the one of the Cauchy stress

$$\sigma = \frac{A_0(1-\alpha)^2}{2}\frac{2E}{\sqrt{1+2E}} \tag{II.109}$$

and we plot an example of softening behaviour on Figure II.14. Figure II.14a shows the stress evolution with a hyperelastic phase followed by a softening one, while Figure II.14b shows the evolution of the damage: during the hyperelastic phase, the damage is zero, and after the critical stress has been reached, the damage grows until it reaches the value one for which the material is considered broken.

II.2.3 Localised damage evolution in a 1D hyperelastic bar

As previously seen, let us now consider a bar damaged on a finite interval $[X_0 - d, X_0 + d]$. The damage criterion reads

$$a'(\alpha)\psi_0(F) + w'(\alpha) - w_1\ell^2\alpha'' = 0. \tag{II.110}$$

Multiplying by α' and adding and substracting $a(\alpha)\psi_0'(F)$ gives

$$\alpha' a'(\alpha)\psi_0(F) + a(\alpha)\psi_0'(F) - a(\alpha)\psi_0'(F) + \alpha' w'(\alpha) - w_1\ell^2\alpha'\alpha'' = 0, \tag{II.111}$$

rewritten

$$\frac{\mathrm{d}}{\mathrm{d}x}\left(a(\alpha)\psi_0(F)\right) - a(\alpha)\frac{\partial\psi_0(F)}{\partial F}\frac{\partial F}{\partial x} + \frac{\mathrm{d}}{\mathrm{d}x}(w(\alpha)) - \frac{\mathrm{d}}{\mathrm{d}x}\left(\frac{w_1\ell^2}{2}\alpha'^2\right) = 0. \tag{II.112}$$

Since the first Piola-Kirchhoff tensor is equal to $\Pi = \dfrac{\partial \psi(F)}{\partial F} = a(\alpha)\dfrac{\partial \psi_0(F)}{\partial F}$, (II.112) can be integered with respect to the space variable X, and leads to

$$a(\alpha)\psi_0(F) - \Pi F + w(\alpha) - \frac{w_1 \ell^2}{2}\alpha'^2 = ct = \psi_0(F_0) - \Pi F_0 \tag{II.113}$$

The constant is determined using the fact that the expression is valid for any α, and thus for $\alpha = 0$

$$a(\alpha)\psi_0(F) - \Pi F + w(\alpha) - \frac{w_1 \ell^2}{2}\alpha'^2 = \psi_0(F_0) - \Pi F_0, \tag{II.114}$$

which is equivalent to

$$a(\alpha)\psi_0(F) - \Pi F - \psi_0(F_0) + \Pi F_0 + w(\alpha) - \frac{w_1 \ell^2}{2}(\alpha')^2 = 0. \tag{II.115}$$

In the case that we are studying, we remind that the hyperelastic potential is

$$\psi(F) = \frac{A(\alpha)}{2}\left(\frac{1}{2}(F^2 - 1) - \ln(F)\right) \tag{II.116}$$

and consequently

$$\Pi = \frac{A(\alpha)}{2}\left(F - \frac{1}{F}\right) \tag{II.117}$$

which can be inverted to get the expression of F with respect to Π

$$F = \frac{\Pi}{A(\alpha)} + \frac{\sqrt{\Pi^2 + A(\alpha)^2}}{A(\alpha)}. \tag{II.118}$$

To solve (II.115), let us introduce $H(\Pi, \alpha)$ such that

$$\ell^2 \alpha'^2 = \frac{2}{w_1} H(\Pi, \alpha), \tag{II.119}$$

and

$$H(\Pi, \alpha) = a(\alpha)\psi_0(F) - \Pi F - \psi_0(F_0) + \Pi F_0 + w(\alpha). \tag{II.120}$$

When the bar is not fully broken ($\alpha_{max} < 1$), the damage is maximum in X_0, then the spatial derivative of α is null, and $H(\alpha_{max}, \Pi) = 0$. Numerically, we can inject (II.117), (II.118) in which α is equal to α_{max} in (II.120) and look for the value of Π that makes H the closest to zero. Once the value is found, it is injected in the equation (II.119) that is solved numerically and gives the damage profile $\alpha(X)$ on the bar. These profiles are plotted on Figure II.15a for different values of α_{max}.

When the bar is broken, *i.e.* $\alpha_{max} = 0$, the damage criterion reduces to the one obtained with small deformation, because at that point, only the dissipated energy plays a role, and is chosen the same in small and large deformation. In our models, there is no difference in the

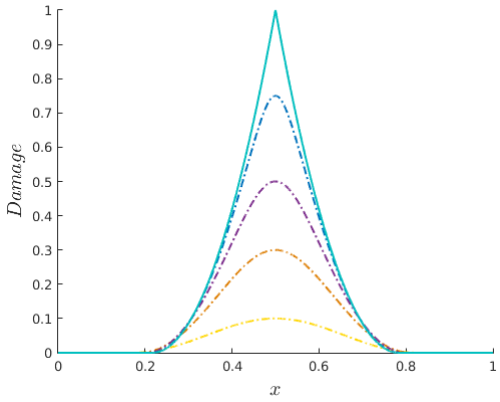

(a) Localisation of damage on the bar during the snap-back, for large deformation.

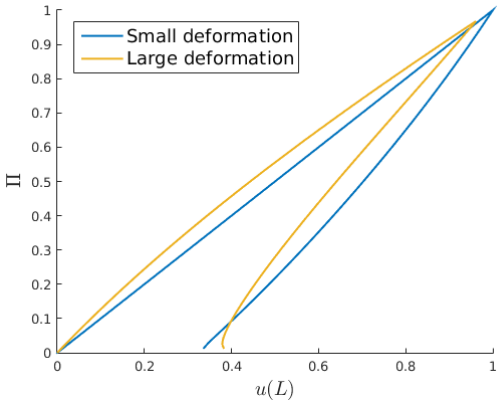

(b) Comparison of snap-backs for small and large deformation: second Piola-Kirchhoff stress Π *with respect to the loading* $u(L)$*.*

Figure II.15: Snap-back

damage profile and the dissipated energy for an elastic material and a hyperelastic material. Yet, the evolution of the stress is different, because of the non linearities in large deformation. One way to put forward this difference consists in looking at the snap-backs for both small and large deformation.

In order to plot the snap-back, the value of the displacement at the extremity of the bar which is submitted to loading has to be determined. Since, for a given α_{max}, Π and $\alpha(x)$ are known on $(0, L)$, F is known too. In 1D, $F = 1 + u'(X)$, and by integrating on the bar, we get

$$u(L) = u(0) + \int_0^L (F(X) - 1)\mathrm{d}X. \tag{II.121}$$

The snap-backs are plotted on Figure II.15b. The area of a snap-back shall give the dissipated energy. In our case, the numerical results give the theoretical value of G_c with less than 1% of error.

II.3 Damage and hyper-viscoelasticity

In large deformation, the additive decomposition of the deformation tensor is not valid any more. We turn to the multiplicative decomposition of the gradient transformation tensor $\boldsymbol{F}$ ([57])

$$\boldsymbol{F} = \boldsymbol{F^e}.\boldsymbol{F^v} \tag{II.122}$$

where $\boldsymbol{F^e}$ is the elastic part of the tensor, and $\boldsymbol{F^v}$ the viscous part. This means that for each point, this gradient is decomposed as the contribution of an elastic (reversible) part, and a

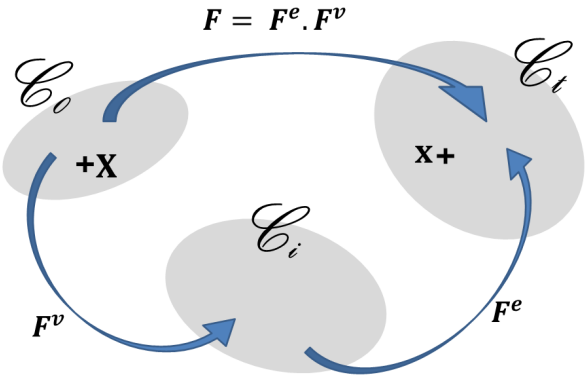

Figure II.16: Introduction of an intermediate state between the reference and the final configuration, free of stress.

viscous part. A relaxed configuration $\mathscr{C}_i$ is defined, such that the material is free of stress in that configuration. The viscous transformation is the passage from the initial state $\mathscr{C}_0$ to the intermediary state $\mathscr{C}_i$. An illustration of this decomposition is shown on Figure II.16.

The gradient of speeds is defined as follows

$$\boldsymbol{L} = \dot{\boldsymbol{F}}\cdot\boldsymbol{F}^{-1} = \left[\dot{\boldsymbol{F}}^{e}\cdot\boldsymbol{F}^{v} + \boldsymbol{F}^{e}\cdot\dot{\boldsymbol{F}}^{v}\right](\boldsymbol{F}^{v})^{-1}\cdot(\boldsymbol{F}^{e})^{-1}, \tag{II.123}$$

and is rewritten

$$\boldsymbol{L} = \boldsymbol{L}^{e} + \boldsymbol{L}^{v} \tag{II.124}$$

with

$$\boldsymbol{L}^{e} = \dot{\boldsymbol{F}}^{e}\cdot\boldsymbol{F}^{e^{-1}} \tag{II.125}$$

$$\boldsymbol{L}^{v} = \boldsymbol{F}^{e}\cdot\dot{\boldsymbol{F}}^{v}\cdot(\boldsymbol{F}^{v})^{-1}\cdot(\boldsymbol{F}^{e})^{-1} \tag{II.126}$$

We then define the viscous Green-Lagrange deformation tensors on the initial configuration $\mathscr{C}_0$

$$\boldsymbol{E}^{\boldsymbol{v}} = \frac{1}{2}(\boldsymbol{F}^{\boldsymbol{v}^{\boldsymbol{T}}}\cdot\boldsymbol{F}^{\boldsymbol{v}} - \boldsymbol{I}) \tag{II.127}$$

and the tensor of elastic deformation $\bar{\boldsymbol{E}}^{e}$ that is by definition defined on the intermediate configuration $\mathscr{C}_i$

$$\bar{\boldsymbol{E}}^{e} = \frac{1}{2}\left((\boldsymbol{F}^{e})^{T}\cdot\boldsymbol{F}^{e} - \boldsymbol{I}\right) \tag{II.128}$$

Since the partition of deformation is valid only on a same configuration, the total strain can be defined as the sum of an elastic part and a viscous part only if a transport is done

$$\boldsymbol{E} = \boldsymbol{F}^{\boldsymbol{v}^{\boldsymbol{T}}}\cdot\bar{\boldsymbol{E}}^{e}\cdot\boldsymbol{F}^{\boldsymbol{v}} + \boldsymbol{E}^{\boldsymbol{v}}. \tag{II.129}$$

To overcome some difficulties, the behaviour law can be written on the intermediate configuration $\mathscr{C}_i$. The second Piola-Kirchhoff stress tensor in the relaxed configuration is

$$\bar{\boldsymbol{S}} = \frac{\partial\psi}{\partial\bar{\boldsymbol{E}}^{e}}, \tag{II.130}$$

and is related to the Kirchhoff stress in the actual configuration $\mathscr{C}_t$ by

$$\boldsymbol{\tau} = \boldsymbol{F}^e \cdot \bar{\boldsymbol{S}} \cdot (\boldsymbol{F}^e)^T. \tag{II.131}$$

Pulling back in the initial configuration $\mathscr{C}_0$ gives the first Piola-Kirchhoff stress that is used for the equilibrium equations

$$\boldsymbol{\Pi} = \boldsymbol{\tau} \cdot \boldsymbol{F}^{-T}. \tag{II.132}$$

The viscous dissipation used for the viscoelastic behaviour is

$$\Phi = 2\eta \|(\boldsymbol{L} - \boldsymbol{L}^{\boldsymbol{e}})_{sym}\|^2. \tag{II.133}$$

II.3.1 Maxwell model

The approach in this part will essentially be the same as the one followed in II.1, except that we will first deal with the Maxwell rheological model (c.f. Figure II.1) made of a spring connected in series with a dashpot.

II.3.1.a Energy

The hyperelastic potential is again chosen as the 1D Ciarlet-Geymonat potential, expressed this time with respect to the elastic deformation because it is the elastic energy that corresponds to the energy of the spring of rigidity A

$$\psi(E^e) = \frac{A}{2}\left[E^e - \frac{1}{2}\ln(1 + 2E^e)\right]. \tag{II.134}$$

If we work in the relaxed configuration, that is, the stress free configuration, we use (II.130) in 1D and have

$$\bar{S} = \frac{A}{2}\left(\frac{2E^e}{1 + 2E^e}\right), \tag{II.135}$$

so the Kirchhoff stress in the actual configuration is

$$\tau = \frac{A}{2} 2E^e, \tag{II.136}$$

and the first Piola-Kirchhoff stress is

$$\Pi = \frac{A}{2}\frac{(F^e)^2 - 1}{F}. \tag{II.137}$$

The same damage laws as previously are used: the dissipated energy during a homogeneous process of damage is chosen as a linear function of α

$$w(\alpha) = w_1 \alpha \tag{II.138}$$

and the localised energy is

$$\frac{1}{2} w_1 \ell^2 (\alpha')^2. \tag{II.139}$$

The total energy of the structure in the reference configuration, after discretization, is therefore

$$\begin{aligned}\mathscr{E}(u,F^v,\alpha) = \int_{\Omega_0} \frac{A(\alpha)}{2}\left[\frac{1}{2}\left(\frac{F^2}{(F^v)^2}-1\right)-\frac{1}{2}\ln\left(\frac{F^2}{(F^v)^2}\right)\right] \\ + w(\alpha)+\frac{1}{2}w_1\ell^2(\alpha')^2+2\eta\frac{\Delta t}{2}\left(\frac{F^v-F^v_{i-1}}{\Delta t F^v_{i-1}}\right)^2 \mathrm{d}X.\end{aligned} \tag{II.140}$$

II.3.1.b First order stability

The derivative of (II.140) at point u in the admissible direction v, keeping in mind that in 1D, $F(u) = 1 + u'$, gives the equilibrium in the reference configuration

$$\mathrm{Div}(\Pi) = 0,\ X \in \Omega_0. \tag{II.141}$$

The derivative of (II.140) at point α in the admissible direction β gives the damage criterion

$$\frac{A'(\alpha)}{2}\left[\frac{1}{2}\left(\frac{F^2}{(F^v)^2}-1\right)-\frac{1}{2}\ln\left(\frac{F^2}{(F^v)^2}\right)\right]+w'(\alpha)-w_1\ell^2\alpha''\geq 0 \quad \text{in } \Omega_0 \tag{II.142}$$

as well as boundary conditions

$$\frac{\partial\alpha}{\partial n}\geq 0 \quad \text{on } \partial\Omega_0. \tag{II.143}$$

Finally, the derivative of (II.140) at point F^v in the direction $\xi^v \in \mathcal{X}$ gives

$$\int_{\Omega_0}\left[\frac{\partial\psi}{\partial F^v}\xi^v+2\eta\Delta t L^v\frac{\xi^v}{\Delta t F^v_{i-1}}\right]\mathrm{d}X = 0 \quad \forall\xi^v, \tag{II.144}$$

and using the chain rule on the term $\dfrac{\partial\psi}{\partial F^v}$ gives

$$\int_{\Omega_0}\left[-\bar{S}\frac{(F^e)^2}{F^v}+2\eta L^v\frac{1}{F^v_{i-1}}\right]\xi^v\mathrm{d}X = 0 \quad \forall\xi^v. \tag{II.145}$$

Taking $\Delta t \to 0$, we find the evolution law for the hyper-viscoelastic material

$$L^v = \frac{\tau}{2\eta}. \tag{II.146}$$

II.3.1.c Hyper-viscoelastic phase

In the same way as in II.1, we begin with the study of a phase during which no damage is occurring. Combining (II.146) with (II.136) gives

$$\dot{\tau} = \left(\tau+\frac{A_0}{2}\right)\left[\frac{2\dot{F}}{F}-\frac{\tau}{\eta}\right]. \tag{II.147}$$

Setting $\frac{2\dot{F}}{F} = \varepsilon_0$, with ε_0 a constant that can be identified as the speed loading, comes to imposing a deformation such that

$$F(t) = \exp(t\varepsilon_0/2). \tag{II.148}$$

Since the Kirchhoff stress τ used in the viscoelastic law is usually related to the true strain $\varepsilon_{true} = \ln(F)$, this leads to

$$\varepsilon_{true} = \frac{t\varepsilon_0}{2}. \tag{II.149}$$

We now denote $\Sigma = \tau + \frac{A_0}{2}$, the equation (II.147) becomes

$$\dot{\Sigma} = -\frac{\Sigma^2}{\eta} + \left(\frac{A_0}{2\eta} + \varepsilon_0\right)\Sigma, \tag{II.150}$$

Bernouilli equation whose solution is

$$\Sigma = \frac{\frac{A_0}{2} + \eta\varepsilon_0}{1 + \frac{2\varepsilon_0\eta}{A_0}\exp\left(-t(\varepsilon_0 + \frac{A_0}{2\eta})\right)}. \tag{II.151}$$

Hence the Kirchhoff stress is

$$\tau = \frac{A_0\eta\varepsilon_0\left[\exp\left(t\left(\frac{A_0}{2\eta} + \epsilon_0\right)\right) - 1\right]}{A_0\exp\left(t\left(\frac{A_0}{2\eta} + \epsilon_0\right)\right) + 2\eta\epsilon_0}, \tag{II.152}$$

which is a growing function of time, and gives the Maxwell limit $\eta\varepsilon_0$ when t goes to infinity.

II.3.1.d Homogeneous damage

The damage criterion (II.142) does not enable us to exhibit an analytical value of the time t_e at which damage begins to grow. Yet, written as a function of time $f(t)$ for $\alpha = 0$

$$f(t) = w_1 - A_0[E^e(t) - \frac{1}{2}\ln(1 + 2E^e(t))], \tag{II.153}$$

we can see, by using (II.136) and the fact that the elastic deformation tends to $\frac{\eta\varepsilon_0}{A_0}$ when t goes to infinity, that the limit of f when t goes to infinity can be written as a function of the speed loading

$$g(\varepsilon_0) = w_1 - A_0\left[\frac{\eta\varepsilon_0}{A_0} + \frac{1}{2}\ln\left(1 + 2\frac{\eta\varepsilon_0}{A_0}\right)\right]. \tag{II.154}$$

g is a decreasing function of ε_0, $g(0) = w_1 > 0$ and g tends to minus infinity when the speed loading is large. Thus, there exists a speed ε_0^c for which the damage criterion is reached. We

can notice that this is exactly the same argument as the one that was one in small deformation in II.1.2.a, and this threshold speed value is therefore a particularity of the Maxwell rheological model, for both small and large deformation frameworks.

To compute the evolution of the damage during a traction test, we set the differential equation in terms of F^e. On one hand, we have from the damage criterion

$$1-\alpha = \frac{2w_1}{A_0\left[(F^e)^2 - 1 - \ln((F^e)^2)\right]} \tag{II.155}$$

and on the other hand we have from the viscous evolution law

$$\tau = L^v 2\eta = 2\eta\left(\frac{\dot{F}}{F} - \frac{\dot{F}^e}{F^e}\right). \tag{II.156}$$

Using the relation $\tau = A_0(1-\alpha)^2 E^e$, we get

$$A_0(1-\alpha)^2\frac{1}{2}((F^e)^2-1) = \eta\left(\varepsilon_0 - 2\frac{\dot{F}^e}{F^e}\right) \tag{II.157}$$

that leads to

$$\dot{F}^e = \frac{F^e}{2\eta}\left[\eta\varepsilon_0 - \frac{A_0}{2}(1-\alpha)^2((F^e)^2-1)\right] \tag{II.158}$$

in which we inject (II.155). We solve this equation numerically with the initial condition $F^e(0)=1$, we deduce the expression of α and of τ. An example is plotted on Figure II.17: on Figure II.17a, the evolution of the Kirchhoff stress is shown with respect to the time. On Figure II.17b, the evolution of the damage can be seen: it is first null then grows steadily until it reached the value 1. We remind that in order for a viscous material following a Maxwell law to damage, a condition on ε_0 has to hold: it should be such that the value of the critical stress be lesser than the limit value of the stress $\eta\varepsilon_0$.

II.3.1.e Damage localisation

We consider now a damage field which is not homogeneous on the bar any more. We invert the expression

$$\Pi = \frac{A(\alpha)}{2}\frac{(F^e)^2-1}{F} \tag{II.159}$$

in order to have the expression of F^e with respect to the stress Π, that we inject in the damage criterion, and we obtain

$$\frac{A'(\alpha)}{2}\left[\frac{F\ \Pi}{A(\alpha)} - \frac{1}{2}\ln\left(1+2\frac{F\ \Pi}{A(\alpha)}\right)\right] + w_1 - w_1\ell^2\alpha'' = 0 \tag{II.160}$$

When the bar is broken, Π is null on the bar, and the damage profile of the broken bar reduces to the expression

$$A_0\ell^2\alpha'' = w_1 \tag{II.161}$$

which is the same as in small deformation, for a linear elastic material and a Maxwell viscoelastic material.

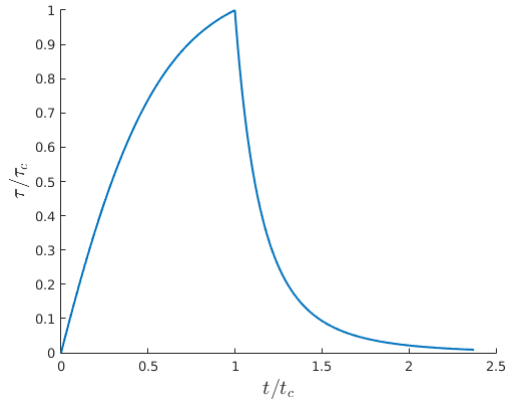

(a) Stress evolution.

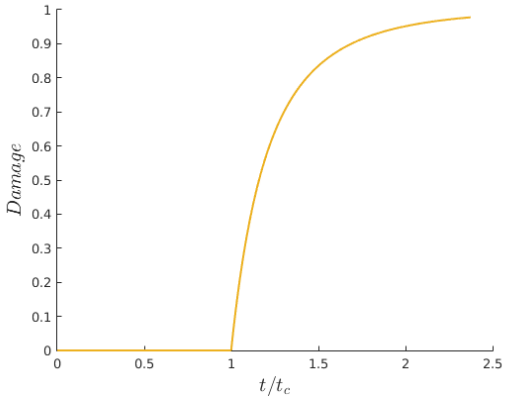

(b) Damage evolution.

Figure II.17: Homogeneous evolution of the Kirchhoff stress τ and the damage during a traction test for a Maxwell hyper-viscoelastic model.

II.3.1.f Numerical implementation

The numerical implementation of the one dimensional damaging hyper-viscoelasticity is a combination of the implementation of the visco-elasticity and of the 1D hyperelasticity. We have to solve successively three problems, of displacement, viscosity and damage, and we use again the strategy of alternate minimization. The damage problem is the same as previously seen, and the viscous and displacement problems are non linear problems.

We compare the numerical results of the Maxwell model with the analytical ones: at the same time, it enables to check the implementation of the hyperelastic problem seen in II.2 and the Maxwell hyper-viscoelastic problem. The homogeneous damage evolution is computed: a large enough internal length has to be chosen. The comparison of the analytical results and the numerical results is shown on Figure II.18. The two curves match nearly perfectly. Indeed, the time step has to be very small in order that the numerical results converge to the analytical ones.

II.3.2 Zener model

In the case of the Zener model, the elastic potential is the sum of two potentials: one is written with respect to the total deformation, to take into account the energy of the main spring, and the other is written with respect to the elastic deformation. Unlike small deformation, where the Zener and Poynting-Thomson model exhibit the same viscoelastic responses, there is a difference in the responses of these two models in large deformation. We use here the Zener model because it is a particular case of the generalized Maxwell model (with one branch) commonly used to model viscoelastic behaviours. The elastic potentials are again those of Ciarlet-Geymonat in 1D. We note A the rigidity of the main spring, and A^e the rigidity of

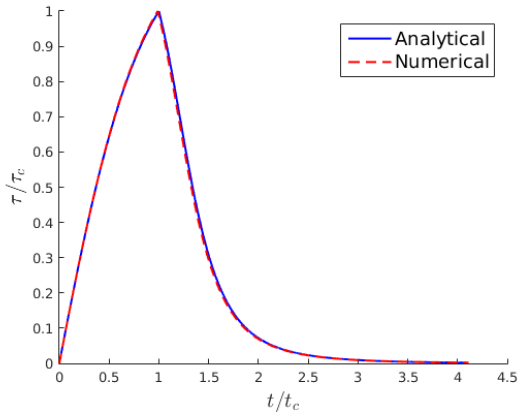

Figure II.18: Homogeneous damage evolution for a Maxwell hyper-viscoelastic model. Comparison of the analytical results obtained with MATLAB and of the numerical results obtained with FEniCS.

the spring in the Maxwell branch. The total hyperelastic potential is

$$\psi = \frac{A}{2}\left(E - \frac{1}{2}\ln(1+2E)\right) + \frac{A^e}{2}\left(E^e - \frac{1}{2}\ln(1+2E^e)\right) \tag{II.162}$$

Consequently, the first Piola-Kirchhoff stress is

$$\Pi = \frac{A^e E^e + AE}{F}. \tag{II.163}$$

The total energy of the material is

$$\begin{aligned}\mathscr{E}(u, F^v, \alpha) = \int_{\Omega_0} \frac{A^e(\alpha)}{2}\left[\frac{1}{2}\left(\frac{F^2}{(F^v)^2} - 1\right) - \frac{1}{2}\ln\left(\frac{F^2}{(F^v)^2}\right)\right] + \frac{A(\alpha)}{2}\left[\frac{1}{2}(F^2-1) - \frac{1}{2}\ln(F^2)\right] \\ + w(\alpha) + \frac{1}{2}w_1\ell^2(\alpha')^2 + 2\eta\frac{\Delta t}{2}\left(\frac{F^v - F^v_{i-1}}{\Delta t F^v_{i-1}}\right)^2 \mathrm{d}X.\end{aligned} \tag{II.164}$$

The Gâteaux derivative at point α in the direction $\beta \in \mathcal{D}_t$ gives the damage criterion in the bulk

$$\frac{A'(\alpha)}{2}\left(E(u) - \frac{1}{2}\ln(1+2E(u))\right) + \frac{A^{e\,\prime}(\alpha)}{2}\left(E^e - \frac{1}{2}\ln(1+2E^e)\right) + w'(\alpha) - w_1\ell^2\alpha'' \geq 0 \quad \text{in } \Omega_0 \tag{II.165}$$

and boundary conditions

$$\frac{\partial\alpha}{\partial n} \geq 0 \quad \text{on } \Omega_0. \tag{II.166}$$

The Gâteaux derivative of the total energy (II.164) at point u in the direction $v \in \mathcal{C}_0$ gives the equilibrium in the bulk

$$\mathrm{Div}(\Pi) = 0 \quad \text{in } \Omega_0. \tag{II.167}$$

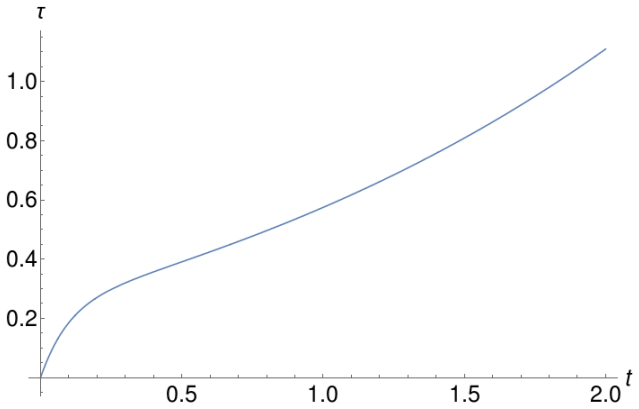

Figure II.19: Stress response with respect to time of a hyper-viscoelastic Zener material, with $A = 1, A^e = 10$ *and* $\eta = 0.5$*. Obtained with the numerical solving of the differential equation* (II.169).

Finally, the Gâteaux derivative of (II.164) at point F^v in the direction $\xi^v \in \mathcal{X}$ gives the viscous evolution law

$$L^v = \frac{1}{2\eta}\left(\tau - \frac{A}{2}(F^2 - 1)\right) \tag{II.168}$$

Combining (II.168) with (II.163) and $L^v = \dot{F}^v/F^v$ gives the differential equation that rules the viscous evolution

$$\dot{\tau} = (A + A^e + 2\tau)\frac{\dot{F}}{F} - \frac{1}{2\eta}\left(A + A^e + 2\tau - AF^2\right)\left(\tau - \frac{A}{2}(F^2 - 1)\right) \tag{II.169}$$

and can be solved numerically, as shown on Figure II.19. In this case, the deformation associated to the stress τ is again such that $F(t) = \exp(t\varepsilon_0/2)$.

When damage is added to the viscous evolution law, the equations become quite large and can only be studied numerically. The implementation follows the same method as for the Maxwell model. Since the results cannot be compared to analytical ones, there is no point in showing them here. It has been checked that the dissipated energy takes the desired value.

II.3.3 Conclusion

To conclude this part, we insist on two main points. First, the study of a 1D hyperelastic damaging bar has shown that the damage profile for a broken bar in the reference configuration is identical to the one obtained in small deformation, thus making the critical energies also identical. The difference is seen in the way the snap-back occurs, because the evolution of the stress for different values of maximum damage is different in small and large deformation.

Secondly, the analytical study of viscoelastic material, modelled by the Maxwell and Poynting-Thomson models, in small and large deformation, has revealed interesting properties. It turns out that for the Maxwell model, there is a threshold in the strain rate (related

to the material parameters) below which *homogeneous* damage cannot occur. Though for the Poynting-Thomson model, such a threshold for homogeneous damage does not exist, there is yet a condition on the strain rate, this time allowing for the *localisation* of damage. When the strain rate is close to the critical value, we observe a temporal regularization of the jump in the energies: damage occurs as a quasi-continuous process that grows first homogeneously, then localising on the bar. We can imagine that such a regularisation could happen for more strain rate values, if more branches with different relaxation times were added in the model, that would become a generalised Maxwell model.

CHAPTER III

NUMERICAL STUDY OF DAMAGE GRADIENT MODELS FOR LARGE DEFORMATION

Contents

This chapter deals with the numerical implementation of the gradient damage models in an academic finite element code in dimensions 2 and 3, and its application to standard tests. We will see that the use of these damage models is perfectly relevant in the framework of large deformation to model the initiation of cracks in sound material, but that numerical trouble inherent to the computation of large displacements have to be somehow overcome.

One of the first mention of the implementation and the use of the gradient damage models in large deformation can be found in the work of Del Piero, Lancioni and March in [13], in 2007. They reformulate the minimization problem in the context of finite elasticity, and perform numerical simulations in 2D with a compressible Neo-Hookean hyperelastic potential. Their work was followed by Miehe and Schänzel in 2014, in [50],when they used the so-called phase-field models to model the behaviour of rubbery polymers in a framework of rate-independent crack propagation. At the same time, Hesch and Weinberg [26] also worked with the phase-field models in finite deformation. In 2015, Henao, Mora-Corral and Xu used the gradient damage models to model the fracture in non linear elasticity in [24]. Their approach is more mathematical, and relies on the introduction of a non linear polyconvex energy. We can also cite the recent contributions of Kumar, Francfort and Lopez-Pamies in [33] where simulations with quasi-incompressible materials are performed, and Hesch and al. in [27].

III.1 Numerical implementation

The code that was used to carry out more heavy simulations is an academic finite element code resulting from the MEF++ project [16] of the GIREF research group. It was created in 1996 by the researchers of the GIREF team of the university of Laval in Quebec, in Canada. Since then, it has developed considerably, launching a parallelized version in 2003. Many problems of fundamental and applied research are solved, including optimisation, mesh adaptation in 2D and 3D, fluid (incompressible Navier-Stockes) and solid mechanics problems. In particular, it is able to solve problems of very large deformation in solid mechanics, and this is the reason it has been chosen.

III.1.1 Recall: displacement problem in large deformation

This section serves as a reminder of the necessary techniques needed in order to solve a non linear displacement problem in large deformation. First, a quick review of the existing hyperelastic laws is done, followed by a recall of the finite element method used in the resolution of a finite strain problem.

III.1.1.a Choice of the hyperelastic law

First, note that all the hyperelastic laws proposed here are isotropic, since in large deformation, anisotropy has to be treated by adding terms in the hyperelastic potential, and this is out of the scope of this work.

The choice of the hyperelastic potential is wide, and many laws have been created to reproduce the behaviour of elastomers under various types of solicitation (uni-axial, bi-axial, etc.) for large or very large deformation. A review of available models that have proven to be well representative of the behaviour of elastomers can be found in [44]. Figure III.1

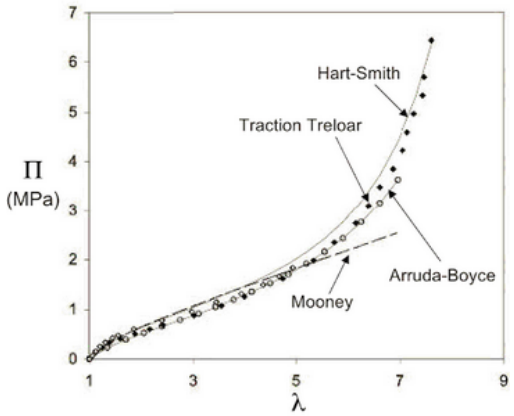

Figure III.1: Comparison between three hyperelastic laws (Mooney, Arruda-Boyce and Hart-Smith) and experimental results of Treloar, for a traction test. Nominal stress with respect to the elongation. Figure from [38].

shows the behaviour of the Mooney, Arruda-Boyce and Hart-Smith models, compared with the experimental results of Treloar for a uni-axial tension test. We can see that some models are better at predicting the behaviour of the material at large strains than others. For an example, the Mooney model is not able to render the hardening of a polymer that happens for elongations superior to 5.

Globally, hyperelastic models can be classified into two groups: the first are issued from physical considerations, while the second are issued from mathematical developments. The 8-chain model of Arruda and Boyce [5] introduced in 1993 belongs to the first family: it is based on the macromolecular structure of the rubber, and captures well the behaviour of rubber for uni-axial and bi-axial extension, uni-axial compression, plane strain compression and pure shear. More recently, the micro sphere model of Miehe, Göktepe and Lulei [48] was able to describe the elastic response of rubbery polymers at large strains from a micro-mechanically based network model. We can also cite the variational network-based model of Alicandro, Cicalese and Gloria [3], further studied in [22] by Gloria, Le Tallec and Vidrascu, or the tube model of Heinrich and Kaliske [23].

In the category of models issued from mathematical developments, we can cite the generalized Rivlin model, also called polynomial hyperelastic model, which is written as a function of the reduced two first invariants of right Cauchy-Green tensor $\boldsymbol{C}$

$$\psi = \sum_{p,q=0}^{N} C_{pq}(\bar{I}_1 - 3)^p(\bar{I}_2 - 3)^q + \sum_{m=1}^{M} D_m(J-1)^{2m}. \tag{III.1}$$

The C_{pq} parameters, where "p" is the power of the I_1-dependence of the strain energy density, and "p" is the power of the I_2-dependence of the strain energy density, are material constants related to the isochoric response of the material. The D_m are material constants related to the volumetric response. The number of terms in the expansion is determined by the application's accuracy requirements.

In the case $N = 1$ and $M = 1$, the Mooney-Rivlin material is obtained, that is written in 3 dimension

$$\psi = C_{10}(\bar{I}_1 - 3) + C_{01}(\bar{I}_2 - 3) + D(J-1)^2. \tag{III.2}$$

This is the potential we will work with in the following numerical tests. If the coefficient D which is equal to $\kappa/2$, κ the bulk modulus, is taken sufficiently large with respect to the coefficients C_{10} and C_{01}, the material is quasi-incompressible.

This Mooney-Rivlin law is polyconvex ([6]), which ensures the existence of at least one solution. The potential is decomposed additively into two parts resulting from purely isochoric deformation and volumetric deformation. Physically, it is motivated by the premise that the dilation and the deviatoric responses of rubber-like materials are sustained by different mechanisms. To obtained this decomposition, the deformation gradient tensor is decomposed as follows

$$\boldsymbol{F} = J^{1/3}\bar{\boldsymbol{F}} \tag{III.3}$$

and we can see that the determinant of $\bar{\boldsymbol{F}} = 1$, so that $\bar{\boldsymbol{F}}$ is the gradient deformation tensor associated to a volume preserving deformation. The hyperelastic potential of a Mooney-Rivlin law in 3D is therefore decomposed into an isochoric part and a volumetric part

$$\psi = w(\bar{I}_1, \bar{I}_2) + U(J), \tag{III.4}$$

where

$$w(\bar{I}_1, \bar{I}_2) = C_{10}(\bar{I}_1 - 3) + C_{01}(\bar{I}_2 - 3) \tag{III.5}$$

and

$$U(J) = \frac{\kappa}{2}(J-1)^2. \tag{III.6}$$

I_1 and I_2 are called reduced invariants: $\bar{I}_1 = J^{-2/3}I_1$ and $\bar{I}_2 = J^{-4/3}I_2$, with $I_1 = \mathrm{tr}\boldsymbol{C}$ and $I_2 = \frac{1}{2}((\mathrm{tr}\boldsymbol{C})^2 - \mathrm{tr}(\boldsymbol{C})^2)$.

III.1.1.b Variational formulations

This part is a recall of the way an inelastic problem can be solved numerically. It is essentially based on the finite element course of Fortin and Garon [17] from the university of Laval, and enables to understand the philosophy of the finite element code we have been working on.

The displacement field that has to be found is the solution of the equilibrium equation that can be written in the reference or the actual configuration. The choice of the configuration on which we will be working will be explained later, for now, let us just write the equilibrium equations in the initial configuration $\mathscr{C}_0$. We consider here only Dirichlet and Neumann boundary conditions, applied on respectively $\partial_D\Omega$ and $\partial_N\Omega$. The system that has to be solved on the reference configuration is therefore the following one

$$\begin{cases} -\nabla\cdot\boldsymbol{\Pi} = & f_0 & \text{in } \Omega_0 \\ \boldsymbol{\Pi}\cdot N = & h_0 & \text{on } \partial_N\Omega_0 \end{cases} \tag{III.7}$$

where f_0 are the body force in the reference configuration, and the second equation accounts for Neumann conditions. Such a formulation is called a total Lagrangian formulation. We can notice that in this formulation, the first Piola-Kirchhoff tensor plays the role of the Cauchy tensor $\boldsymbol{\sigma}$ in the deformed configuration. The variational formulation of this problem on the reference configuration $\mathscr{C}_0$ is

$$\int_{\Omega_0} \mathbf{\Pi}\cdot\mathrm{Div}(w)\ \mathrm{d}X = \int_{\partial_N\Omega_0} h_0 w \mathrm{d}S + \int_{\Omega_0} f_0 w\ \mathrm{d}X. \tag{III.8}$$

In most cases of large deformation, the material is nearly or totally incompressible, that is, its variation of volume is close to zero which gives $\det\boldsymbol{F} \simeq 1$. The formulation in pure displacement becomes unsuitable to compute the correct field of displacement. To overcome this problem, a mixed formulation is used: a second variable, named pressure, is introduced, and the pair (u, p) has to be found. The pressure is defined as follows

$$p = -\frac{1}{3}\mathrm{tr}(\boldsymbol{\sigma}), \tag{III.9}$$

and

$$p = -\kappa(J-1). \tag{III.10}$$

for the Money-Rivlin law (III.4).

A decomposition of the second Piola-Kirchhoff stress tensor is introduced

$$\boldsymbol{S} = \boldsymbol{S'} - pJ\boldsymbol{C}^{-1} \tag{III.11}$$

with $\boldsymbol{S'}$ the derivative of the isochoric part of (III.4)

$$\boldsymbol{S'} = 2\left(\frac{\partial w}{\partial \bar{I}_1}\frac{\partial \bar{I}_1}{\partial \boldsymbol{C}} + \frac{\partial w}{\partial \bar{I}_2}\frac{\partial \bar{I}_2}{\partial \boldsymbol{C}}\right) \tag{III.12}$$

Finally, the variational formulation of a mixed problem in large displacements is

$$\begin{cases} \displaystyle\int_{\Omega_0} \boldsymbol{S'}\cdot(\boldsymbol{F}^T\mathrm{Div}(w))\ \mathrm{d}X - \int_{\Omega_0} pJ\boldsymbol{F}^{-T}\cdot\mathrm{Div}(w)\ \mathrm{d}X = \int_{\partial_N\Omega} h_0 w\ \mathrm{d}S + \int_{\Omega_0} f_0 w\ \mathrm{d}X \\ \displaystyle\int_{\Omega_0} (J-1)q\ \mathrm{d}X + \int_{\Omega_0} \frac{1}{\kappa} pq\ \mathrm{d}X = 0. \end{cases} \tag{III.13}$$

This formulation is non linear and has to be linearised. Because of this non linearity, the Newton method is often used to solve this problem (see *e.g.* Le Tallec [34]). We write

$$R_1((u,p),w) = \int_{\Omega_0} \boldsymbol{S'}\cdot(\boldsymbol{F}^T\mathrm{Div}(w))\ \mathrm{d}X - \int_{\Omega_0} pJ\boldsymbol{F}^{-T}\cdot\mathrm{Div}(w)\ \mathrm{d}X - \int_{\partial_N\Omega} h_0 w\ \mathrm{d}S - \int_{\Omega_0} f_0 w\ \mathrm{d}X \tag{III.14}$$

and

$$R_2((u,p),q) = \int_{\Omega_0} (J-1)q\ \mathrm{d}X + \int_{\Omega_0} \frac{1}{\kappa} pq\ \mathrm{d}X. \tag{III.15}$$

Starting from an approximation (u_0, p_0) of the displacement and the pressure, we look for a correction (δ_u, δ_p) such that

$$\begin{cases} R_1((u_0+\delta_u, p+\delta_p), w) = & 0 \\ R_2((u_0+\delta_u, p+\delta_p), q) = & 0 \end{cases} \tag{III.16}$$

and this system has to be linearised with respect to both the variables u and p.

$$\begin{cases} \dfrac{\partial R_1((u_0,p_0),w)}{\partial u}\delta u - \displaystyle\int_{\Omega_0} \delta_p J\boldsymbol{F}^{-T}(u_0)\cdot\mathrm{Div}(w)\mathrm{d}X = & -R_1((u_0,p_0),w) \\ \quad -\displaystyle\int_{\Omega_0} qJ\boldsymbol{F}^{-T}(u_0)\cdot\mathrm{Div}(\delta_u)\mathrm{d}X - \int_{\Omega_0}\frac{1}{\kappa}\delta_p q\mathrm{d}X = & -R_2((u_0,p_0),q) \end{cases} \tag{III.17}$$

In order to decrease the size of the non linear systems that has to be solved, a common technique is the penalisation technique. Within specific conditions, it enables to eliminate the variable p from the system. This method is very efficient when the pressure is discretized with discontinuous polynomials from one element to another. Most frequent cases are the linear or continuous approximations by element.

On a element K, the linearised formulation (III.17) becomes, under matricial form

$$\begin{bmatrix} A^K & B^{K^T} \\ B^K & M^K \end{bmatrix} \begin{bmatrix} \delta_u^K \\ \delta_p^K \end{bmatrix} = - \begin{bmatrix} R_1^K \\ R_2^K \end{bmatrix} \tag{III.18}$$

where the elementary matrices are directly defined by (III.17). When p is discontinuous on the elements, the matrix M^K is of dimension 1 by 1 and is vol/κ. Consequently we have

$$\delta_p^K = \frac{-\kappa}{\mathrm{vol}(K)}\left(\int_K J(\boldsymbol{F}^{-T}(u_0)\cdot\nabla_X\delta_u)\mathrm{d}X + \int_K (J-1)\mathrm{d}X - \frac{p^K}{\kappa}\mathrm{vol}(K)\right). \tag{III.19}$$

We exposed briefly in this part how the displacement problem is solved in the code used for the simulations.

III.1.2 Damage problem

The damage problem is the same as was seen in the first chapter, except that it has now to be defined in higher dimensions. The dissipated energy density is again the sum of a dissipated energy during a homogeneous process of damage and a dissipated energy during the localisation of damage

$$s(\alpha, \nabla\alpha) = w(\alpha) + \frac{1}{2}w_1\ell^2\nabla\alpha\cdot\nabla\alpha \tag{III.20}$$

with

$$w(\alpha) = w_1\alpha. \tag{III.21}$$

The dissipated energy on the structure is therefore

$$\mathscr{S}(\alpha, \nabla\alpha) = \int_{\Omega_0} \left(w(\alpha) + \frac{1}{2} w_1 \ell^2 \nabla\alpha \cdot \nabla\alpha \right) \mathrm{d}X. \tag{III.22}$$

At that point, a question that arises is: is this energy on the reference configuration sufficient to render the rupture in large deformation? Following the analysis of [25], if we add a term equivalent to a surface energy accounting for the stretching of the surfaces of the body, including the cracks, it does not make a considerable difference in the numerical results. We will consequently make the choice of working in the reference configuration with a dissipated energy which is the same as in small deformation. With this definition, the rupture energy G_c that is usually defined will have a meaning only in the reference configuration.

In order to use the damage models, we have to set the dependency of the stress-strain law to the damage parameter α. In 1D, for both small and large deformation, we have seen that it was chosen such that the material rigidity would depend on α *via* a decreasing function of α. In higher dimensions, in large deformation, we chose to put this dependency directly in front of the hyperelastic potential, as was done *e.g.* in [32]

$$\psi(\boldsymbol{F}, \alpha) = a(\alpha)\psi_0(\boldsymbol{F}) \tag{III.23}$$

where $a(\alpha)$ is a quadratic function of α

$$a(\alpha) = (1-\alpha)^2. \tag{III.24}$$

For a Mooney-Rivlin hyperelastic potential for an example, it takes the form

$$\psi(\boldsymbol{F}, \alpha) = C_{10}(1-\alpha)^2(\bar{I}_1 - 3) + C_{01}(1-\alpha)^2(\bar{I}_2 - 3) + \frac{\kappa_0(1-\alpha)^2}{2}(J-1)^2. \tag{III.25}$$

With the formula (III.25), we can see that when the damage reaches the value 1, both the isochoric part and the volumetric part become zero: the two material coefficients of the law are null, as is the compressibility coefficient. For the latter, this means that in the zone where the material is damaged, it becomes compressible.

Note that written in that way, our models do not make any difference between tension and compression in the way rupture occurs. In 2009, Amor, Marigo and Maurini [4] proposed a volumetric-deviatoric split model so that only the tension would play a role in the fracture of the structure. In 2010, Miehe, Hofacker and Welschinger [49] introduced a spectral model that separates tension and compression. In our case, compression tests will not be performed, and this is why no special decomposition is used.

We now briefly detail the variational formulation of the damage problem. The total energy of the structure in the reference configuration is

$$\mathscr{E}(u, \alpha) = \int_{\Omega_0} \left((1-\alpha)^2 \psi_0(\boldsymbol{F}, \alpha) + w_1 \alpha + \frac{1}{2} w_1 \ell^2 \nabla\alpha \cdot \nabla\alpha \right) \mathrm{d}X. \tag{III.26}$$

The variational formulation for a test function β is

$$\int_{\Omega_0} \left(-2(1-\alpha)\psi_0(\boldsymbol{F},\alpha)\beta + w_1\beta + w_1\ell^2\nabla\alpha\cdot\nabla\beta\right) \mathrm{d}X. \tag{III.27}$$

Moreover, since the problems are solved in correction, that is, the variable is decomposed as the sum of a previously calculated value and a correction that has to be found

$$\alpha = \alpha_0 + \delta\alpha, \tag{III.28}$$

we inject this expression in the variational formulation and we get

$$\int_{\Omega_0} \left((w_1 - 2\psi_0)\beta + 2\psi_0\alpha_0\beta + w_1\ell^2\nabla\alpha_0\cdot\nabla\beta + 2\psi_0\delta\alpha\beta + w_1\ell^2\nabla(\delta\alpha)\cdot\nabla\beta\right) \mathrm{d}X. \tag{III.29}$$

The terms that contribute to the elementary matrix are

$$2\psi_0\delta\alpha\beta + w_1\ell^2\nabla(\delta\alpha)\cdot\nabla\beta, \tag{III.30}$$

and the ones that are in the residue are

$$(w_1 - 2\psi_0)\beta + 2\psi_0\alpha_0\beta + w_1\ell^2\nabla\alpha_0\cdot\nabla\beta \tag{III.31}$$

because α_0 is already known.

Contrary to the library FEniCS that automatically computes the gradient and the Hessian of the objective energy (the energy to be minimised), with MEF++ we have to give the terms that will construct the vector gradient and the Hessian matrix. We see that the gradient vector can be directly assembled from the residue, and the Hessian matrix from the matrix.

To solve the damage problem, a non linear bound constrained solver has to be used. The TAO optimization software library (contained in the PETSc libraries) is chosen. For each time step, the lower bound has to be updated so that it corresponds to the value of the damage found in the previous time step.

One of the advantages of such a choice of the damage laws ((III.23) and (III.24)) is that the objective function that has to be minimised is a quadratic function of α, the gradient is linear, and the Hessian is constant. Hence, numerical methods conceived for this type of minimisation can be used. We use a GPCG method (gradient projected conjugate gradient algorithm), that is a conjugate-gradient based method for bound-constrained minimization. It assumes that the objective function is quadratic and convex, therefore, it evaluates the objective function, the gradient, and the Hessian only once.

III.1.3 Remark: implementation with the FEniCS library

In the chapter II, all the 1D numerical examples were done with the library FEniCS. Yet, gradient damage models were also implemented in higher dimensions in the library. Using the demonstration of hyperelasticity available with the open source library, and adding damage,

the implementation does not require many efforts, and this is why it is not detailed here: it still consists in a loop during which the displacement problem and the damage problem are solved successively. Yet, in order to be able to withstand very large displacements, a finite element code has to be very robust, and specific methods to help the convergence of the non linear solver have to be used. Moreover, solving a non linear problem is quite slow, compared to a linear problem, and it the use of parallel solving becomes highly recommended. Most of non linear solvers available in FEniCS do not work in parallel, and the ones that do, are not very robust for this type of problems. For all these, reasons, the academic code MEF++ was usually preferred over the FEniCS library.

III.2 2D simulations

The code allows the user to set conditions of plain strain in order to perform 2D simulations. It is also possible to use axi-symmetric conditions. In this case, we first make sure that the axial symmetry is lost before we use this hypothesis. In this section, though, we will focus on a 2D plate submitted to uni-axial traction, that can be seen as a simple extension of the 1D bar under traction studied in II.2.3.

III.2.1 General considerations

Relation between the critical stress and the internal length

An elongation λ is applied on the right boundary of a 2D plate, and the normal displacement on the left is blocked. For a purely incompressible material, the gradient deformation tensor under conditions of plain strain is

$$\boldsymbol{F} = \begin{bmatrix} \lambda & 0 & 0 \\ 0 & \dfrac{1}{\lambda} & 0 \\ 0 & 0 & 1 \end{bmatrix} \tag{III.32}$$

where the elongation λ is equal to $1+u'$. The damage criterion of an incompressible Mooney-Rivlin material is

$$C'_{10}(\alpha)(I_1 - 3) + C'_{01}(\alpha)(I_2 - 3) + w'(\alpha) = 0 \tag{III.33}$$

where $I_1 = \lambda_1^2 + \lambda_2^2 + \lambda_3^2$ and $I_2 = \lambda_1^2\lambda_2^2 + \lambda_2^2\lambda_3^2 + \lambda_3^2\lambda_1^2$.
Thus we have

$$C_{10}(\lambda^2 + \frac{1}{\lambda^2} - 2) + C_{01}(\lambda^2 + \frac{1}{\lambda^2} - 2) = \frac{w_1}{2}, \tag{III.34}$$

and the critical stress is

$$\lambda_c = \sqrt{\frac{C + \sqrt{C^2 - 4}}{2}}, \quad \text{with} \quad C = 2 + \frac{w_1}{2(C_{10} + C_{01})}. \tag{III.35}$$

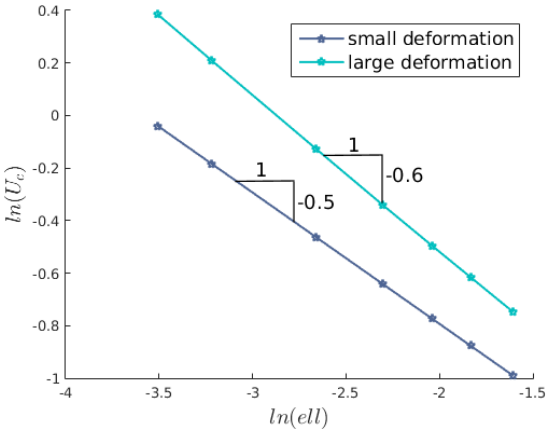

Figure III.2: Comparison of the relation between the critical displacement U_c and the internal length ℓ for small and large deformation.

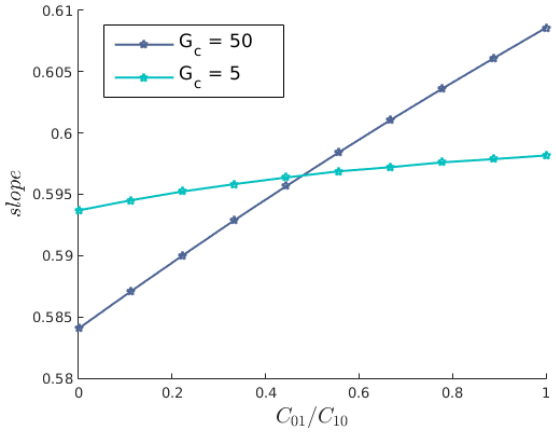

Figure III.3: Comparison between the slopes of the linear fitting of the curves $U_c = f(\ell)$ for two different values of G_c, with respect to the ratio of the Mooney-Rivlin coefficients.

To compare with small deformation, we write the elastic energy with the Lamé coefficients

$$\psi(\boldsymbol{\varepsilon}) = \frac{\lambda}{2}(\mathrm{tr}\boldsymbol{\varepsilon})^2 + \mu \mathrm{tr}(\boldsymbol{\varepsilon}^2) \tag{III.36}$$

which reduces to

$$\psi(\boldsymbol{\varepsilon}) = \mu \mathrm{tr}(\boldsymbol{\varepsilon}^2) \tag{III.37}$$

for incompressible materials, with the condition $\mathrm{div}(u) = 0$. Finally, the damage criterion is

$$4\mu_0(\lambda - 1)^2 - w_1 = 0 \tag{III.38}$$

with the relation $\mu = 2(C_{10} + C_{01})$. Since $\lambda - 1 = u$, and $w_1 = G_c/(c_w \ell)$ in the numerical simulations, it is easy to see that the critical load U_c is the inverse of a square function of the internal length

$$U_c = \sqrt{\frac{G_c}{4\mu_0 c_w \ell}}. \tag{III.39}$$

At equivalent deformation, the stress with a Hooke's law is higher than for a hyperelastic material. So the critical stress is reached for lowest values of displacement in small deformation. Moreover, Figure III.2 shows that the relation between the internal length and the critical displacement are not the same in small and large deformation. In small deformation, we have seen that the critical displacement u_c is a function of $1/\ell^{0.5}$. A linear approximation of the logarithmic curve of U_c with respect to ℓ in large deformation obtained with (III.34) shows that U_c is a function of $1/\ell^{0.6}$.

In large deformation, Figure III.3 shows that for small values of G_c, *i.e.* for small values of critical displacement, the relation between the critical displacement and the internal length

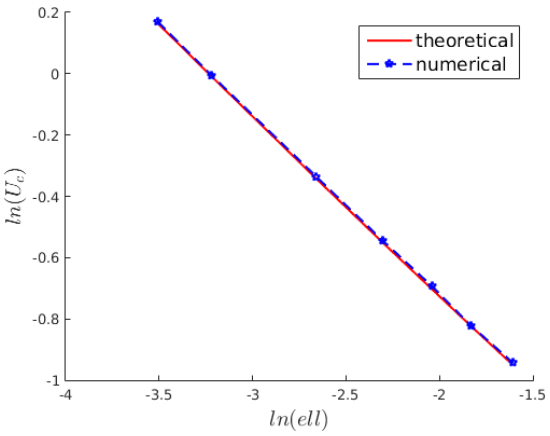

Figure III.4: Relation between the internal length ℓ and the critical displacement for two different bulk modulus, and comparison with the theoretical values.

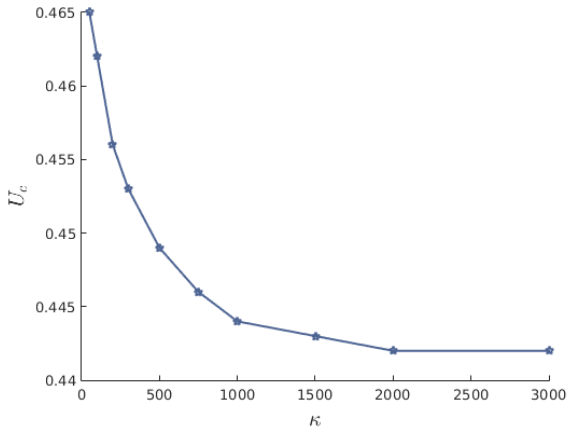

Figure III.5: Critical displacement with respect to the compressibility of the material: the critical displacement tends to a fixed value when the material becomes quasi-incompressible.

does not depend strongly on the ratio between the two Mooney-Rivlin coefficients. For larger values of G_c, this dependency increases, but nonetheless stays very small. The approximation $U_c \sim 1/\ell^{0.6}$ is therefore valid for any parameters of the model.

Simulations were performed on 2D plates, for different values of G_c so that the critical displacement would be either small or large. Various internal lengths were also tested, and the results displayed on Figure III.4 show a very good agreement between the theoretical and numerical values. The bulk modulus being chosen much greater than the Monney-Rivlin coefficients, the material is quasi-incompressible, and there is no significant difference in the values of the critical loads for $\kappa = 100$ and $\kappa = 1000$. The results are also quasi identical when a quadratic function of u is used, or when a structured mesh is used.

On Figure III.5, the critical displacement is plotted with respect to the compressibility κ: the more incompressible the material is, the sooner it breaks, and when the value of κ is big enough, a constant critical stress is obtained. Here, the theoretical critical displacement for a purely incompressible material is 0.4383, and there is 0.08% of error with the numerical results.

Boundary conditions on the displacement

For simplicity, the boundary conditions on the displacement are called Dirichlet conditions when the displacement is imposed. They are in fact conditions of Robin type with penalisation values so that the results are the same as for Dirichlet conditions.

Convergence in the alternate minimisation

One of the difficulties that may arise during the computation of a test, is that the convergence in the alternate minimisation is too fast, *i.e.* that the damage grows and reaches its maximum value too quickly. This triggers convergence problems of the displacement problem, because it is as if a substantial loading was imposed all of a sudden on the structure. In this situation, the non linear solver has troubles converging to the solution.

To prevent a growing of the damage that is too fast, we used mainly two techniques. The first consists in calculating the difference in two successive maximum values of α in the alternate minimisation: if this difference is larger than a given threshold, the damage vector is replaced by a combination of its previous value weighted by a chosen parameter. The second way to reduce the convergence of the damage problem is to multiply the Hessian matrix (which is a constant) by a scalar so that the convergence is slowed down. An example is given in Figure III.6 where a comparison is made on two plates submitted to traction with the same material and numerical parameters, except that in one case, the Hessian matrix is multiplied by 2. Figure III.6a shows that if the Hessian matrix is untouched, the damage reaches a value close to 1 very quickly, and the calculation (depending on the tolerance) can be made in 20 iterations. If the Hessian matrix is multiplied by 2, the convergence is smoother, and it takes more iterations to converge on α, which is exactly the aim of this method. Figure III.6b illustrates these explanations: at a given time step of the alternate minimisation (here, the 20th), the damage profile found with an untouched Hessian matrix is much more advanced (in terms of final result) than the one found if the Hessian is multiplied by 2. In the end of the alternate minimisation, the damage profiles are quasi identical. We could argue that since more iterations are required to converge in the alternate minimisation when the Hessian is multiplied, this is in fact a loss of time. Yet, since the displacement problem converges much more easily when the damage does not grow too quickly, there is no loss of time, and it even accelerates the convergence. In this particular case, the calculations with the natural Hessian took 168 seconds while the calculations with a doubled Hessian took 164 seconds.

Residual stiffness

The numerical parameter k_{res} ensures that the problem remains elliptic and solvable when the damage becomes close to one. In large deformation, it becomes essential in order to help the convergence of the non linear solver of the displacement problem. In our simulations, its value is usually $1e-03$, which could be thought rather large. Yet, tests were done, and showed that this value does not have an influence either on the rupture energy value or the maximum value of α, as can be seen in Table III.1.

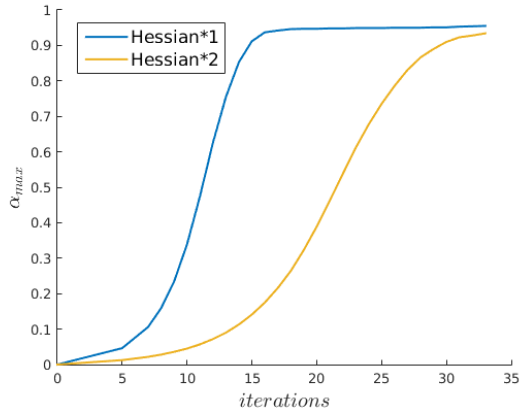

(a) Maximum value of damage with respect to the numbre of iterations in the alternate minimisation.

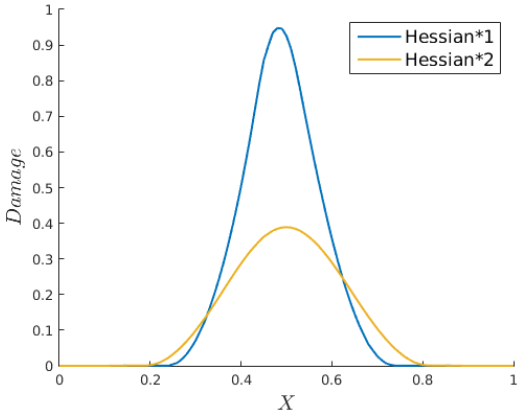

(b) Comparison of the damage profiles at the twentieth time step of the alternate minimisation.

Figure III.6: Comparison of the evolution of damage during the alternate minimization when the Hessian matrix is multiplied by 1 or 2. Case of a 2D plate under uni-axial tension with a ratio $\ell/L = 0.16$.

k_{res}	$1e-3$	$1e-04$	$1e-05$	$1e-06$
G_c	1.022	1.027	1.027	1.027
α_{max}	0.970	0.973	0.973	0.973

Table III.1: 2D plate under uni-axial traction. Rupture energy and maximum value of damage for different values of k_{res}.

L	H	C_{10}	C_{01}	κ	ℓ	G_c	k_{ell}	tol	h
1.0	0.1	10	5	100	0.10	50	1e-3	1e-4	0.01

Table III.2: Geometrical, material and numerical parameters for a 2D plate submitted to traction.

III.2.2 Particular case of a 2D plate under uni-axial traction

Data settings

We show now one example of a 2D plate submitted to uni-axial traction. The two components of the displacement on its left end are blocked, and the x component of the displacement is imposed as a growing function of time while the y component is also blocked. The geometric parameters are summarized in Table III.2: the length of the plate is 1, its height is 0.1.

The displacement is chosen as linear, the pressure is constant on each element, and a penalised formulation is used to solve the displacement-pressure problem. A Mooney-Rivlin law is used, and the compressibility coefficient κ is ten times greater than the first coefficient of the Mooney-Rivlin law C_{10}. This ratio could be chosen higher to ensure a higher incompressibility, but the results in terms of fracture would not be very different, and the calculation would be much more tricky. This is why we chose such values, so that the quasi-incompressible behaviour of the material would still be taken into account, but not to the detriment of the computational cost and numerical simplicity.

The damage problem is the same as previously defined: the hyperelastic potential is multiplied by a function of α, so that it is null when α reaches the value 1. The internal length is one tenth of the length of the plate, and the mesh size is ten times smaller than the internal length. The residual stiffness is chosen large enough to help the convergence of results, and the alternate minimisation should stop when a tolerance of 1e-4 on α is reached.

Results

A quasi-static test is performed, and since the plate is plain, without any micro defects that would trigger stress concentration, it breaks suddenly when the critical stress is reached. This can be seen on Figure III.7 which shows the evolution of the energies during the test. During the hyperelastic phase, the dissipated energy is zero because there no damage in the structure, and the total energy is equal to the elastic energy. When the plate breaks, there is a sudden drop of the elastic energy that goes close to zero while the dissipated energy jumps the its value G_c. At the end of the test, the total energy is 11.70, the elastic energy is 0.86 and the dissipated energy is 10.84. Because of the normalisation of the damage problem, this energy should be equal to 10 and we have an error of approximately 8.4%

The damage is well localised on the broken plate, and simulations with other meshes have shown that it is mesh independent. Figure III.8 shows the damage in the reference

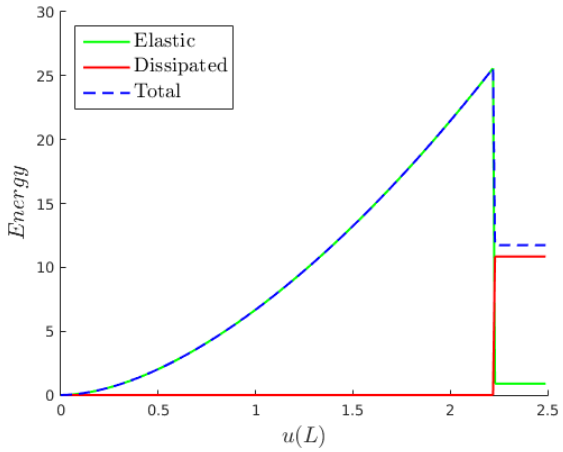

Figure III.7: Evolution of the energies during a traction test on a 2D plate. After a purely hyperelastic phase with no dissipated energy, the plate suddenly breaks and the energy jumps.

configuration on the plate, and on a lineout in order to extract the damage profile.

When the plate is broken, the deformation is not uniform any more. Before it breaks, if the deformation in the plate is of the order of 200%, when it is broken, the deformation concentrates on the zone where α is close to 1, on a very few mesh elements. On this elements, the deformation is therefore very large, it can go up to 2000%. This demonstrates the necessity of having a very robust finite element code, designed for very large deformation.

The displacement in the reference configuration can be seen on Figure III.9. It is clearly separated in two parts, so that the deformation is concentrated in the middle of the sample, where the damage is close to its maximum value 1. Figure III.10 shows the displacement in the deformed configuration, at the beginning of the alternate minimisation, and at the end. Due to the constraint of quasi-incompressibility, the middle zone that is tremendously stretched has to be very thin, and we can see that the mesh elements suffer a huge deformation in this zone.

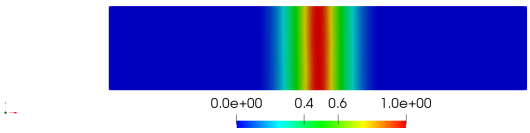

(a) Damage on the plate in the reference configuration.

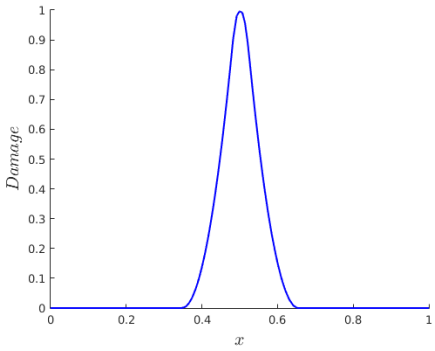

(b) Damage profile obtained from an x-line.

Figure III.8: Damage profile of the broken 2D plate. The damage is well localised in the middle of the sample.

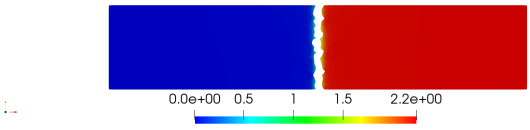

(a) Displacement on the plate in the reference configuration.

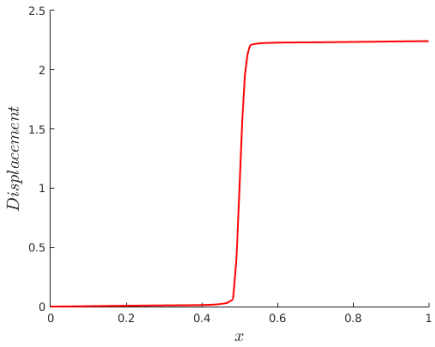

(b) Displacement on a x-line.

Figure III.9: Displacement profiles in the broken 2D plate. The displacement is separated in two phases with the deformation concentrated in the middle of the plate.

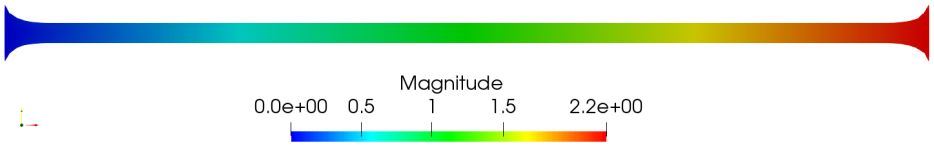

(a) $u(L)/L = 0.43$

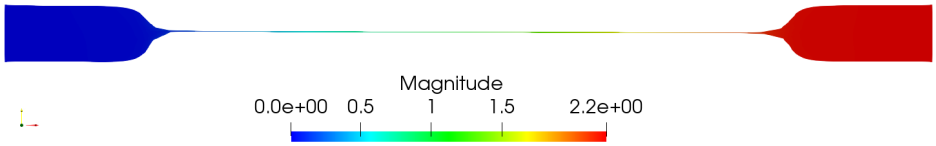

(b) $u(L)/L = 0.59$

Figure III.10: Displacement in the deformed configuration of a 2D plate under uni-axial traction, at the beginning and the end of the alternate minimisation.

III.3 3D simulations

Data settings

After the verification of the implementation of the gradient damage models in a 2D setting, a 3D example is tested. The chosen geometry is a hourglass-shaped specimen, as can be seen on Figure III.11: its length is 0.7, its radius in the ends 0.3 and in the middle 0.12. The curve is obtained using an example of a 2D axi-symmetric stenosis following a cosine function ([59]). The geometry and the mesh are generated in 3D by the software GMSH. An algorithm of 3D optimization of the mesh elements is used in order to ensure a good quality of the elements. The mesh is made of tetrahedral elements, randomly generated, and it is refined in the strangle part of the sample, so that the biggest elements are of size 0.021 and the smallest 0.017. All these geometrical parameters can are written in the Table III.3. In the end, the structure is composed of 162000 elements, and the mesh can be seen in Figure III.11b.

The problem consists of a specimen submitted to uni-axial traction: the left extremity is clamped using Dirichlet boundary conditions on the three components of the displacement, a growing x displacement is imposed on the right extremity and the two other components of the displacement are blocked. Dirichlet boundary conditions of zero damage are imposed on the two extremities of the sample, because we expect it to damage in its middle part.

The displacement field is taken as linear, and the pressure is constant by element so that a penalised formulation can be used. The damage is linear. Because of the very large strains in the damaged zones, and of the supplementary difficulty induced by the third dimension, it is essential to use a linear search to optimize the convergence of the non linear solver. A

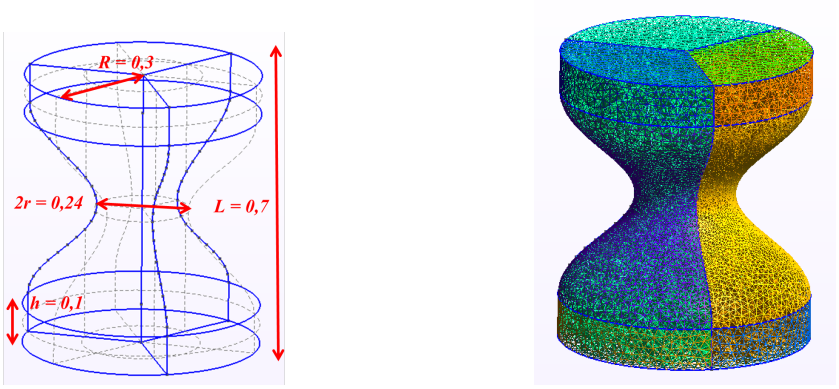

(a) Geometry. *(b) Mesh.*

Figure III.11: Hourglass-shaped specimen: 3D geometry and mesh generated with GMSH.

L	R	r	C_{10}	C_{01}	κ	ℓ	G_c	k_{ell}	tol	h
0.7	0.3	0.12	10	5	70	0.15	10	1e-4	1e-5	0.017 -> 0.021

Table III.3: Geometrical, material and numerical parameters for a 3D hourglass-shaped specimen submitted to traction.

condition of non distortion of the mesh is also imposed, so that if a mesh element becomes too deformed, the correction is diminished.

The main parameters used for this simulation are summarised in the table III.3. The ratio of the compressibility coefficient and the first coefficient of the Mooney-Rivlin law is 7. Because of the difficulties in performing simulations with damage in large deformation, it is complicated to use high compressibility coefficients.

Results

Because of the geometry of the specimen, there is a stress concentration on the borders of its strangle part, and this is therefore the zone where the damage occurs first. Figure III.12 shows the evolution of the damage on the middle plane of the sample, for three different loadings: when damage first occurs, it is only on the boundaries, and the middle part is sound. Then the damage progressively diffuses towards the center while it increases, and after some time, it is uniform on the slice.

The evolution of the energies during the test also show the continuous evolution of damage. Figure III.13 shows that there is no jump of the total energy: after a purely hyperelastic phase, damage begins to grow which makes the elastic energy decrease. At the end of the test, when the damage has reached the value one in its middle part, the elastic energy is close to zero and the total energy is nearly the dissipated energy.

Figure III.14 shows the damage and the displacement at the end of the test, in the

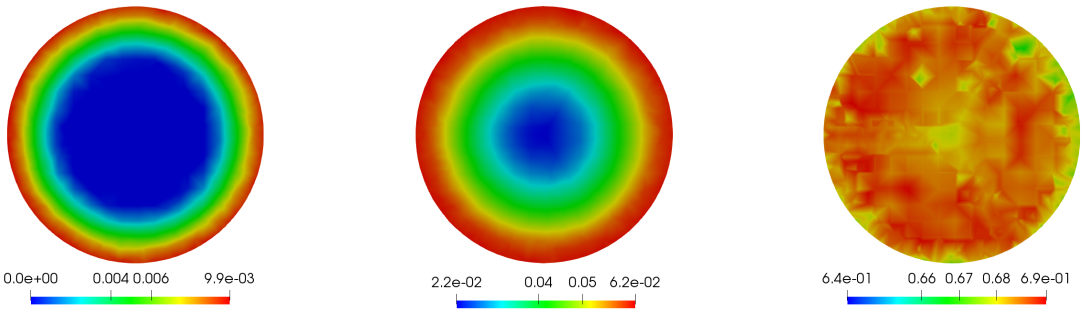

(a) $u(L)/L = 0.29$ (b) $u(L)/L = 0.36$ (c) $u(L)/L = 0.59$

Figure III.12: Slice in the middle plane of the hourglass-shaped specimen submitted to traction. The damage initiates on the borders then grows slowly and diffuses toward the center, until it becomes homogeneous in the plane.

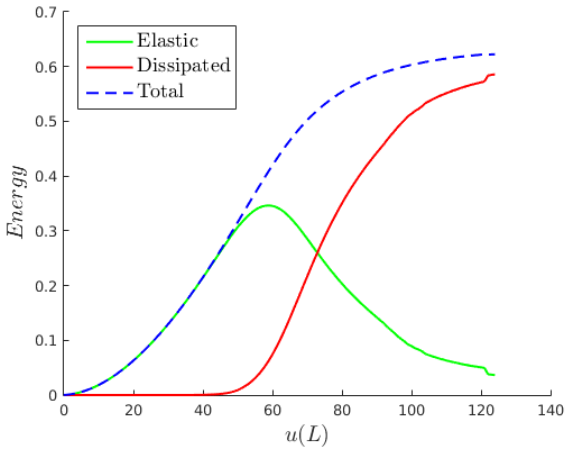

Figure III.13: Evolution of the energies during a traction test on a 3D hourglass-shaped specimen. After a purely hyperelastic phase with no dissipated energy, damage begins to develop progressively in the structure making the elastic energy decrease. When the damage is very high (>0.95), the total energy is mainly made of the dissipated energy.

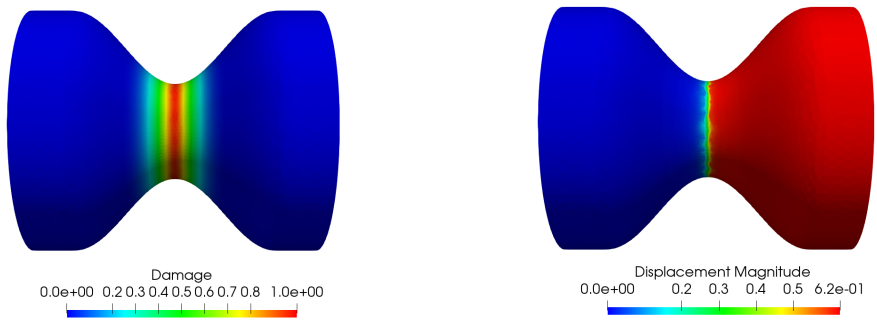

(a) Damage. *(b) Displacement.*

Figure III.14: Hourglass-shaped specimen submitted to traction. Damage and displacement in the reference configuration.

reference configuration. The damage is localised in the strangle part of the sample, and the displacement is clearly separated in two parts: three is no deformation on the left and right side of the sample, only the broken zone is concerned. The deformation is therefore very important in this zone, and this usually triggers problems for the numerical computation of the displacement field.

Finally, Figure III.15 shows successive states of the displacement field of the sample in the deformed configuration. As damage develops, the extremities of the sample relax and the deformation concentrates in the middle part. This zone is very deformed, and the mesh is distorted. Due to the robust code, the displacement problem is able to converge, even with very deteriorated elements.

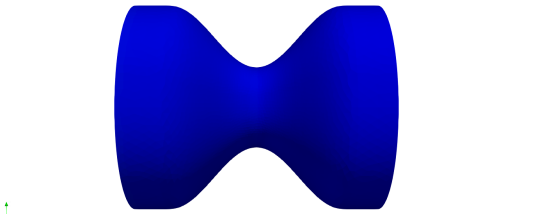

(a) $u(L) = 0$

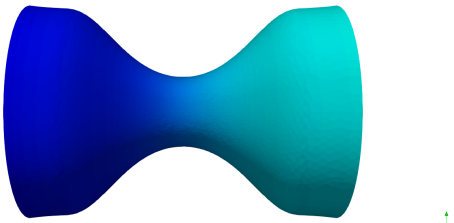

(b) $u(L) = 0.15$

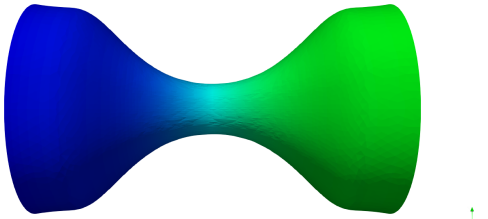

(c) $u(L) = 0.3$

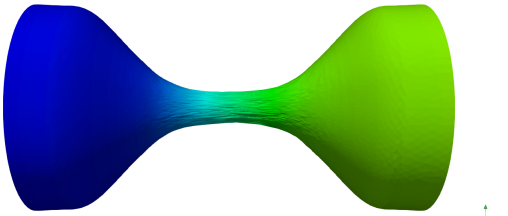

(d) $u(L) = 0.4$

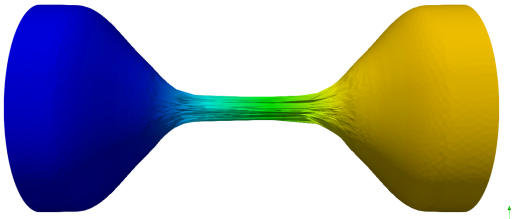

(e) $u(L) = 0.5$

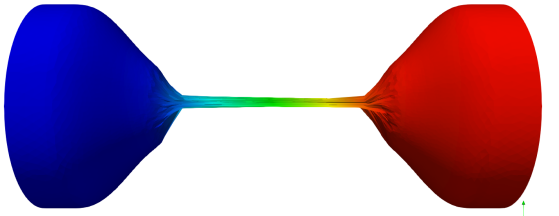

(f) $u(L) = 0.62$

Figure III.15: Hourglass-shaped specimen submitted to traction. Displacement in the deformed configuration for growing loading.

III.4 Conclusion

The gradient damage models are perfectly able to model the rupture of sound, quasi-incompressible structures in large deformations. The results obtained are qualitatively good, and for the most part are similar to the ones that can be obtained when performed in small deformation. The numerical difficulties associated to the computation of damage lies more in the non linear nature of the displacement problem than in the damage problem itself.

Indeed, one drawback of the Lagrangian methods to solve problems of large deformation is the appearance of very deformed elements of the mesh during the loading. These elements can lead to numerical instabilities or convergence problems. One solution is the mesh adaptivity that enables to optimise the quality of the mesh if necessary. Moreover, if the quality of the mesh in the sensitive regions is improved, it usually leads to a better precision of the results. [40] gives an example of the use of this technique in a finite element code.

Besides this mesh adaptivity, another, or complementary solution, lies in the continuation process (see for an example the implementation of such a technique in [36]). Numerical continuation methods are very efficient to improve the convergence, especially around the bifurcation points and limit points, and reduce the computational costs.

Many techniques exist in the industrial world to render the damage problem more easy to solve once the crack has been initiated. The strength of the damage gradient models is more in their ability to initiate damage in perfectly sound structures without the need to introduce artificial defects. When the damage has reached a great enough value - sufficient to think that the structure will break where it is damaged, it is justified to contemplate using another technique to deal with the broken or quasi-broken material, like the X-FEm method for an example.

CHAPTER IV

DAMAGE INITIATION IN ZONES OF HIGH HYDROSTATIC PRESSURE

Contents

It has been noticed, see *e.g.* in the analysis of Poulain and al. [35], that for some polymers, damage initiates in zones of high hydrostatic pressure, and not in zones of high

strain. Yet, the damage laws used in Chapter III are not suitable to model this kind of rupture for incompressible materials. Kumar, Francfort and Lopez-Pamies [33] were the first to address this fault of the gradient damage models. To remedy it, they add an external driving force, in the damage criterion, that is proportional to the pressure. In doing so, they are perfectly able to initiate damage in zones of high pressure, but do not stay within the confine of a variational setting of the damage problem. Their work is hence at the origin of the developments below, and while we aim at the same result, *i.e.* damage initiation in zones of high pressure, the method used are different, since we chose to stay in a variational setting.

Therefore, this chapter aims, in a variational setting, at finding damage laws that fulfil the two following conditions:

- When $\alpha = 0$, the material has to be incompressible
- The hydrostatic pressure has to intervene in the damage criterion, so that depending on the damage parameters, damage can initiate either where the hydrostatic pressure is maximum, or where the deviatoric stress is maximum.

The reasoning will be done in small deformation for the sake of clarity, but can easily be extended to large deformation.

IV.1 Motivations

IV.1.1 Take micro defects into account

Let us consider a full disk made of an incompressible material, submitted to a pressure on its boundary. To preserve its volume, there cannot be any deformation of the disk, and the deformation energy is therefore zero. Without any deformation energy, the critical energy for rupture can not be reached, and the material does not damage, even if the pressure inside is very high.

Let us now consider a disk, with a hole in its center of radius a, such that the displacement imposed on its boundary is a function of a loading parameter t: $u = t\dfrac{a}{r}$. The deformation is $\varepsilon_r = -t\dfrac{a}{r^2}$ and $\varepsilon_\theta = t\dfrac{a}{r^2}$. The radial stress is

$$\sigma_r = -p + 2\mu\varepsilon_r \tag{IV.1}$$

and the hoop stress is

$$\sigma_\theta = -p + 2\mu\varepsilon_\theta. \tag{IV.2}$$

The equilibrium equation gives

$$-\frac{\mathrm{d}p}{\mathrm{d}r} + 4\mu t\frac{a}{r^3} - 4\mu t\frac{a}{r^3} = 0, \tag{IV.3}$$

and therefore p is a constant

$$p = -2\mu\frac{t}{a}. \tag{IV.4}$$

The energy of this structure is the integral over the domain of the elastic energy

$$\mathscr{E} = \int_a^\infty \mu\boldsymbol{\varepsilon}\cdot\boldsymbol{\varepsilon}\ 2\pi r\ \mathrm{d}r, \tag{IV.5}$$

and finally

$$\mathscr{E} = \frac{\pi a^2 p^2}{2\mu}. \tag{IV.6}$$

Thus, in the case of a disk with a hole of radius a in its center, the surface of the defect πa^2 plays a role in the expression of the energy.

Let us now consider that the structure can be damaged, and let us write the strain energy density as the sum of the elastic energy and the dissipated energy

$$W(\boldsymbol{\varepsilon}, \alpha) = \mu(\alpha)\boldsymbol{\varepsilon}\cdot\boldsymbol{\varepsilon} + w(\alpha). \tag{IV.7}$$

The damage criterion is

$$\mu'(\alpha)\boldsymbol{\varepsilon}\cdot\boldsymbol{\varepsilon} + w'(\alpha) \geq 0. \tag{IV.8}$$

Since $\boldsymbol{\varepsilon}\cdot\boldsymbol{\varepsilon} = 2t^2a^2/r^4$, it can be written with respect to the pressure using (IV.4)

$$\frac{\mu'(\alpha)}{2\mu(\alpha)^2}p^2\frac{a^4}{r^4} + w'(\alpha) \geq 0. \tag{IV.9}$$

When the damage initiates in $r = a$, the damage criterion written in $\alpha = 0$ gives

$$\frac{\mu'(0)}{2\mu(0)^2}p^2 + w'(0) = 0. \tag{IV.10}$$

This expression shows that the damage models usually used are able to detect the presence of micro defects, and initiate damage around it, though they are not able to initiate damage when there is no defect in an incompressible material, for which the deformation energy is null.

To illustrate the calculations, Figure IV.1 shows how a defect can affect the initiation of damage and the rupture pattern of a material. The simulations are performed for a compressible material of Poisson coefficient $\nu = 0.3$, in order to be able to apply a radial displacement on the boundary of the disk. Dirichlet boundary conditions of no damage are applied on the borders of the disk.

For a full disk, a three-branch crack suddenly appears (for more information on the shape of the cracks, see [47]). For a disk with a defect whose size is small compared to the internal length, the defect does not affect the final rupture pattern. Yet, it changes the initiation of damage, because as small as the defect be, it triggers stress concentration on its edges, and therefore the critical stress is reached in this region, and axi-symmetric damage develops on the edges of the defect. If the defect and the internal length are of comparable sizes, we can see that the rupture pattern is affected by the presence of the defect.

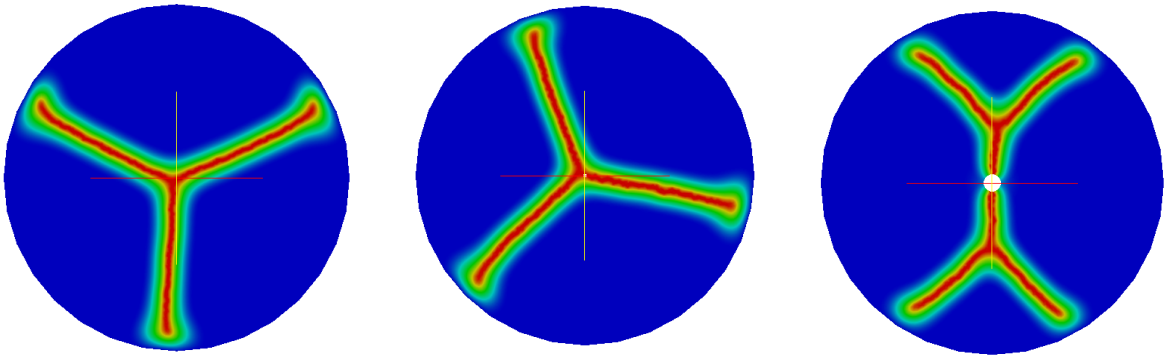

(a) No micro-hole. (b) Micro-hole of radius $r_i = 0.01$. (c) Micro-hole of radius $r_i = 0.05$.

Figure IV.1: Rupture of a compressible disk of radius $r_e = 1$ under radial loading. The internal length is $\ell = 0.1$. When the defect is small compared to the internal length, it does not affect the rupture pattern.

IV.1.2 Properties of the desired model

Purely incompressible material

In a purely incompressible case, the strain tensor reduces to its deviatoric part $\boldsymbol{\varepsilon} = \boldsymbol{\varepsilon}^D$. For a local evolution of damage, the strain energy density is

$$W(\boldsymbol{\varepsilon}, \alpha) = \mu(\alpha)\boldsymbol{\varepsilon}\cdot\boldsymbol{\varepsilon} + w(\alpha), \tag{IV.11}$$

and the damage criterion

$$\mu'(\alpha)\boldsymbol{\varepsilon}\cdot\boldsymbol{\varepsilon} + w'(\alpha) \geq 0 \tag{IV.12}$$

can be re-written with respect to the deviatoric stress $\boldsymbol{\sigma}^D = \boldsymbol{\sigma} + p\boldsymbol{I}$

$$\frac{\mu'(\alpha)}{(2\mu(\alpha))^2}\boldsymbol{\sigma}^D\cdot\boldsymbol{\sigma}^D + w'(\alpha) \geq 0. \tag{IV.13}$$

The expression (IV.16) shows that the damage criterion brings out only the deviatoric part of the stress, and that the hydrostatic pressure does not play any part in the initiation of damage. Hence, with this formulation, whatever the value of the pressure, the damage will only initiate where the deformations are the highest.

Penalisation of the incompressibility

In numerical experiments, a very widespread way to deal with the incompressibility of a material is to write the elastic potential under a penalised form

$$\psi(\boldsymbol{\varepsilon}) = \mu\boldsymbol{\varepsilon}^D\cdot\boldsymbol{\varepsilon}^D + \frac{\kappa}{2}(\mathrm{tr}\boldsymbol{\varepsilon})^2, \tag{IV.14}$$

where the compressibility coefficient κ is a penalisation coefficient that has to be great enough to ensure that, due to minimisation reasons, the part in $\mathrm{tr}(\varepsilon)$ stay small enough. Writing the damage criterion with the laws used in the chapter III

$$\mu(\alpha) = \mu_0(1-\alpha)^2, \quad \kappa(\alpha) = \kappa_0(1-\alpha)^2 \tag{IV.15}$$

gives

$$\frac{\mu'(\alpha)}{(2\mu(\alpha))^2}\boldsymbol{\sigma}^D{\cdot}\boldsymbol{\sigma}^D + \frac{\kappa'(\alpha)}{2}\frac{p^2}{\kappa(\alpha)^2} + w'(\alpha) \geq 0. \tag{IV.16}$$

and with $\alpha = 0$

$$\frac{\boldsymbol{\sigma}^D{\cdot}\boldsymbol{\sigma}^D}{2\mu_0} + \frac{p^2}{\kappa_0} = w_1. \tag{IV.17}$$

We can see that it is precisely with high values of κ_0, that the hydrostatic pressure is eliminated from the damage criterion, and the damage laws previously used are not able to model the initiation of damage due to hydrostatic pressure in quasi-incompressible materials.

To overcome this problem, we change the dependency of the compressibility coefficient to the damage, and write it this way

$$\kappa(\alpha) = \frac{\kappa_e}{\alpha + \eta}, \tag{IV.18}$$

where η is a numerical parameter that ensures the quasi-incompressibility of the material

$$\kappa_0 = \frac{\kappa_e}{\eta}, \tag{IV.19}$$

such that κ_0 is still a penalisation coefficient.

This damage law meets well the first expectation displayed in the introduction of this chapter, namely an incompressible behaviour of the material when $\alpha = 0$. In order to check whether the hydrostatic pressure plays a role in the damage criterion with such a model, we write the strain energy density, derived with respect to α, and written for $\alpha = 0$

$$-\frac{\boldsymbol{\sigma}^D{\cdot}\boldsymbol{\sigma}^D}{2\mu_0} - \frac{p^2}{2\kappa_e} + w'(\alpha) = 0. \tag{IV.20}$$

Unlike the coefficient κ_0, κ_e is not a penalisation coefficient, and can take any value in the range $(0, \infty)$. Depending on the ratio between μ_0 and κ_e, it is now possible to initiate damage in zones of pressure.

IV.2 Inextensible 1D bar

Such a model can be studied in a unidimensional framework. An inextensible bar of length L is submitted to an imposed displacement U. Its energy is such that there cannot be a deformation if there is no damage

$$\psi(\varepsilon, \alpha) = \begin{cases} 0 & \text{if } \alpha = 0 \text{ and } \varepsilon = 0 \\ +\infty & \text{if } \alpha = 0 \text{ and } \varepsilon \neq 0 \\ \dfrac{1}{2}E(\alpha)\varepsilon^2 & \text{if } \alpha > 0 \end{cases} \tag{IV.21}$$

and the rigidity is a function of α, so that it is infinite when $\alpha = 0$

$$E(\alpha) = \frac{k}{2}\left(\frac{1}{D(\alpha)} - 1\right) \quad \text{if } \alpha > 0, \tag{IV.22}$$

where

$$D(\alpha) = 1 - (1-\alpha)^2. \tag{IV.23}$$

The local dissipated energy of damage is also written with respect to $D(\alpha)$

$$w(\alpha) = \frac{\sigma_c^2}{k} D(\alpha). \tag{IV.24}$$

IV.2.1 Analytical study

IV.2.1.a Homogeneous response

First of all, we study the case of homogeneous states of damage, *i.e.* when the damage is uniform on the bar. In that case, the deformation is also uniform: $\varepsilon = U/L$. The damage criterion is therefore

$$-\frac{1}{2}E'(\alpha)\varepsilon^2 = w'(\alpha), \tag{IV.25}$$

and can be re-written with respect to D

$$-\frac{\mathrm{d}E}{\mathrm{d}D}\varepsilon^2 = 2\frac{\mathrm{d}w}{\mathrm{d}D} \tag{IV.26}$$

so that

$$\varepsilon^2 = -2\frac{\dfrac{\mathrm{d}w}{\mathrm{d}D}}{\dfrac{\mathrm{d}E}{\mathrm{d}D}} = 2\frac{\sigma_c^2}{k}\frac{D^2}{\dfrac{k}{2}}. \tag{IV.27}$$

Finally, we have the expression of the deformation with respect to D

$$\varepsilon = \varepsilon_c D, \quad \varepsilon_c = \frac{2\sigma_c}{k}. \tag{IV.28}$$

We inject this expression in the expression of the stress

$$\sigma = E(\alpha)\varepsilon = \frac{k}{2}\left(\frac{1}{D} - 1\right)\varepsilon = \frac{k}{2}\left(\frac{\varepsilon_c}{\varepsilon} - 1\right)\varepsilon, \tag{IV.29}$$

and we finally have

$$\sigma = \sigma_c\left(1 - \frac{\varepsilon}{\varepsilon_c}\right). \tag{IV.30}$$

We can see that if a displacement is imposed on an inextensible bar, it damages as soon as the load is applied. For a null deformation, the stress has the value of the critical stress σ_c, and the stress reaches zero when the imposed displacement is $\varepsilon_c L$. This behaviour can be seen on Figure IV.2.

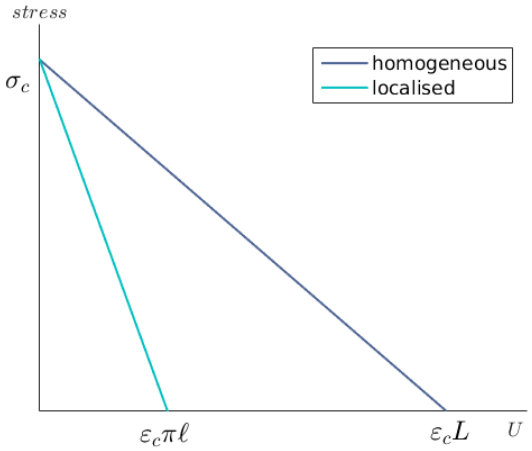

Figure IV.2: Homogeneous and localised responses of an inextensible bar of length L under traction with an imposed displacement U.

IV.2.1.b Localised response

Damage profile

The total energy is

$$\mathscr{E}(u,\alpha) = \int_0^L \left(\psi(u',\alpha) + w(\alpha) + w_1 \ell^2 (\alpha')^2\right) \mathrm{d}x. \tag{IV.31}$$

The damage criterion written in the stress space with $S(\alpha) = 1/E(\alpha)$ is therefore

$$\frac{1}{2} S'(\alpha)\sigma^2 + \frac{2\sigma_c^2}{k}\ell^2 \alpha'' = w'(\alpha), \tag{IV.32}$$

that can be integrated over the bar

$$\frac{1}{2} S(\alpha)\sigma^2 + \frac{\sigma_c^2 \ell^2}{k}(\alpha')^2 = w(\alpha). \tag{IV.33}$$

We multiply by k and introduce D

$$\sigma_c^2 \ell^2 (\alpha')^2 = \sigma_c^2 D(\alpha) - \frac{k}{2}\frac{2}{k}\frac{D(\alpha)}{1-D(\alpha)}\sigma^2 = \frac{D(\alpha)}{1-D(\alpha)}\left[\sigma_c^2(1-D(\alpha)) - \sigma^2\right] \tag{IV.34}$$

and

$$\ell^2 (\alpha')^2 = \frac{D(\alpha)}{1-D(\alpha)}(D_\sigma - D(\alpha)) \tag{IV.35}$$

where $D_\sigma = 1 - \dfrac{\sigma^2}{\sigma_c^2}$. Finally, using the chain rule

$$\alpha' = \frac{\mathrm{d}\alpha}{\mathrm{d}x} = \frac{\mathrm{d}\alpha}{\mathrm{d}D}\frac{\mathrm{d}D}{\mathrm{d}x} = D' \frac{1}{2(1-\alpha)} = \frac{D'}{2\sqrt{1-D}} \tag{IV.36}$$

we inject (IV.36) in (IV.35) and obtain the differential equation that governs the evolution of D

$$\ell^2 D'^2 = 4D(D_\sigma - D). \tag{IV.37}$$

The solution of this equation is

$$D(x) = D_\sigma \cos^2\left(\frac{(x - x_0)}{\ell}\right), \tag{IV.38}$$

and the damage profile of α on the bar is

$$\alpha(x) = 1 - \sqrt{1 - D(\alpha(x))}. \tag{IV.39}$$

An example is plotted on Figure IV.3, for different values of stress in $(0, 1)$.

Displacement

The displacement can be calculated as the integral over the bar of the deformation $\varepsilon = S\sigma$

$$U = \int_0^L S\sigma \mathrm{d}x = \int_0^L \sigma \frac{2}{k} \frac{D}{1 - D} \mathrm{d}x \tag{IV.40}$$

In order to integrate with respect to D, we replace $\mathrm{d}x$ by $\dfrac{\mathrm{d}x}{\mathrm{d}D}\mathrm{d}D$, with

$$\begin{aligned} \frac{\mathrm{d}D}{\mathrm{d}x} &= 2D_\sigma \cos\left(\frac{(x - x_0)}{\ell}\right) \sin\left(\frac{(x - x_0)}{\ell}\right) \frac{1}{\ell} \\ &= \frac{2}{\ell}\sqrt{D_\sigma^2 \cos^2\left(\frac{(x - x_0)}{\ell}\right) \sin^2\left(\frac{(x - x_0)}{\ell}\right)} \\ &= \frac{2}{\ell}\sqrt{DD_\sigma \sin^2\left(\frac{(x - x_0)}{\ell}\right)} = \frac{2}{\ell}\sqrt{D(D_\sigma - D)} \end{aligned} \tag{IV.41}$$

U becomes

$$U = 2\int_0^{D_\sigma} \frac{\sigma}{k} \ell \frac{D}{1 - D} \frac{\mathrm{d}D}{\sqrt{D(D_\sigma - D)}}, \tag{IV.42}$$

and after changing $\theta = D/D_\sigma$

$$U = 2\frac{\sigma}{k}\ell \int_0^1 \sqrt{\frac{\theta}{1 - \theta}} \frac{D_\sigma}{1 - \theta D_\sigma} \mathrm{d}\theta. \tag{IV.43}$$

Finally, this gives

$$U = 2\frac{\sigma}{k}\ell\pi\left(-1 + \frac{1}{\sqrt{1 - D_\sigma}}\right) = \frac{2}{k}\ell\pi\left(-\sigma + \sqrt{\frac{\sigma^2}{1 - D_\sigma}}\right) = \frac{2}{k}\ell\pi(\sigma_c - \sigma). \tag{IV.44}$$

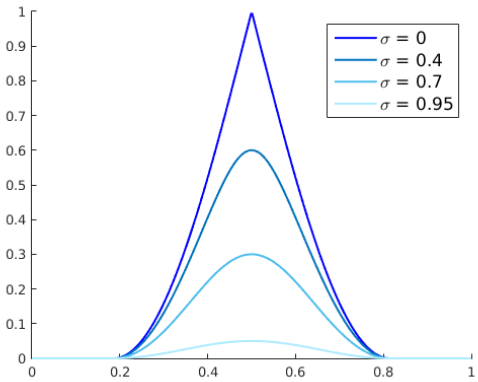

Figure IV.3: Damage profiles for different values of stress of an inextensible bar.

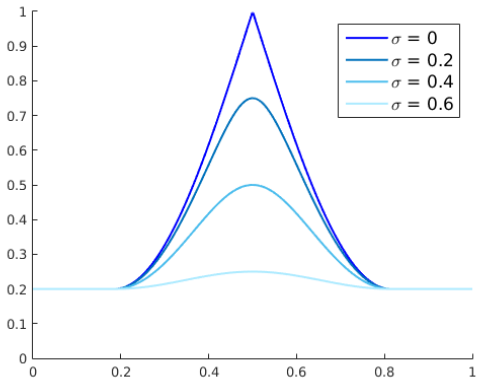

Figure IV.4: Mixed response for different values of stress of an inextensible bar.

Writing with $\varepsilon_c = 2\dfrac{\sigma_c}{k}$, we have

$$U = \pi \ell \varepsilon_c \left(1 - \frac{\sigma}{\sigma_c}\right), \tag{IV.45}$$

and $\sigma = 0$ when $U = \pi\ell\varepsilon_c$. The comparison between the homogeneous and localised responses of σ with respect to U are shown on Figure IV.2. Because of the condition $\pi\ell < L$, σ always decreases faster when the damage localises than when it is homogeneous. Besides, we can see that with the chosen models (IV.21), (IV.22), (IV.24) and (IV.23), the localised response does not have a snap-back: the localisation of damage is a continuous process during the loading.

IV.2.1.c Mixed response

Damage profile

Depending on the choice of the parameters, it can happen that the bar damages in two phases: a first phase during which damage develops homogeneously, and a second phase during which damage localises. The problem is now to find the expression of the damage on the bar, such that

$$\alpha(x) = \begin{cases} \alpha_0 & \text{on } \Omega \setminus \ I_d \\ \alpha(x) & \text{on } I_d. \end{cases} \tag{IV.46}$$

The damage criterion (IV.32) is integrated over the domain, and gives

$$-\frac{\sigma_c^2}{k}\ell^2(\alpha')^2 = w(\alpha) - w(\alpha_0) - \frac{1}{2}(S(\alpha) - S(\alpha_0))\sigma^2), \tag{IV.47}$$

which is

$$-\frac{\sigma_c^2}{k}\ell^2(\alpha')^2 = \frac{\sigma_c^2}{k}(D - D_0) - \frac{1}{k}\left(\frac{1}{1-D} - \frac{1}{1-D_0}\right)\sigma^2. \tag{IV.48}$$

We note $D_\sigma = 1 - \dfrac{\sigma^2}{\sigma_c^2}\dfrac{1}{1-D_0}$, and (IV.48) becomes

$$-\frac{\sigma_c^2}{k}\ell^2(\alpha')^2 = \frac{\sigma_c^2}{k}\frac{D-D_0}{1-D}(D_\sigma - D). \tag{IV.49}$$

Injecting (IV.36) gives

$$\ell^2 D'^2 = 4(D-D_0)(D_\sigma - D), \tag{IV.50}$$

and deriving it leads to

$$\ell^2 D'' + 4D = 2D_\sigma + 2D_0 \tag{IV.51}$$

whose solution is

$$D(x) = \frac{D_\sigma + D_0}{2} + C_1 \cos\left(\frac{2x}{\ell}\right) + C_2 \sin\left(\frac{2x}{\ell}\right). \tag{IV.52}$$

With the conditions $D(x_0 \pm d) = D_0$, $D'(x_0 \pm d) = 0$, and d such that $D(x_0) = 1$, we have

$$D(x) = \begin{cases} D_0 & \text{if } |x - x_0| \geq \dfrac{\pi\ell}{2} \\ D_\sigma \cos^2\left(\dfrac{x-x_0}{\ell}\right) + D_0 \sin^2\left(\dfrac{x-x_0}{\ell}\right) & \text{if } |x-x_0| < \dfrac{\pi\ell}{2} \end{cases} \tag{IV.53}$$

and an example with $\alpha_0 = 0.2$ can be seen on Figure IV.4.

Displacement

The displacement associated to a mixed state of damage is the integral over the bar of the deformation. The bar can be decomposed into two parts: one on which the damage is homogeneous, and the other on which the damage is localised. The latter is of size $\pi\ell$. As was done in the localised case, the integration is made with respect to D

$$\begin{aligned} U &= \int_0^L S\sigma \mathrm{d}x = S_0\sigma(L-\pi\ell) + 2\int_{D_0}^{D_\sigma} \sigma \frac{2}{k}\frac{D}{1-D}\frac{\ell \mathrm{d}D}{2\sqrt{(D-D_0)(D_\sigma - D)}} \\ &= \varepsilon_c L \frac{D_0}{1-D_0}\frac{\sigma}{\sigma_c} + \frac{2\sigma\ell}{k(1-D_0)}\int_{D_0}^{D_\sigma}\sqrt{\frac{D-D_0}{D_\sigma - D}}\frac{\mathrm{d}D}{1-D}. \end{aligned} \tag{IV.54}$$

Finally,

$$U = \varepsilon_c L \frac{D_0}{1-D_0}\frac{\sigma}{\sigma_c} + \varepsilon_c \pi\ell\left(1 - \frac{\sigma}{(1-D_0)\sigma_c}\right). \tag{IV.55}$$

IV.2.1.d Energies

After finding the analytical expression of the damage evolution, for homogeneous, localised and mixed responses, we now want to determine the energies evolution.

Homogeneous solution

In the case of the homogeneous solution, the energy is the integral over the bar of the sum of the elastic energy density and the dissipated energy density $w(\alpha)$, and can be expressed with respect to the loading U, and the critical constants of the material

$$\mathscr{E}(u,D) = \frac{1}{2}S(D)\sigma^2 L + \frac{\sigma_c^2}{k}DL = \frac{1}{2}\sigma U + \frac{1}{2}\sigma_c\varepsilon_c\frac{U}{\varepsilon_c} = \sigma_c U - \frac{1}{2}\frac{\sigma_c U^2}{\varepsilon_c L}. \tag{IV.56}$$

Localised solution

For the localised solution, the energy is the integral over the bar of the elastic energy density, and the dissipated energy densities (local and non local). The dissipated energies are expressed with respect to the variable D, and the non local term had to be calculated. We have

$$D = \hat{D}(\alpha) = 1 - (1-\alpha)^2, \tag{IV.57}$$

therefore

$$\ell^2\nabla\alpha\cdot\nabla\alpha = \ell^2\frac{\nabla D\cdot\nabla D}{\hat{D}'(\alpha)^2} = \ell^2\frac{\nabla D\cdot\nabla D}{4(1-D)}. \tag{IV.58}$$

The energy is

$$\mathscr{E}(u,D) = \int_0^L \left(\frac{1}{2}\sigma u' + \frac{\sigma_c^2}{k}D + \frac{\sigma_c^2}{4k}\frac{\ell^2}{1-D}D'^2\right)\mathrm{d}x = \frac{1}{2}\sigma U + \frac{\sigma_c^2}{k}\int_0^L \left(D + \frac{\ell^2 D'^2}{4(1-D)}\right)\mathrm{d}x \tag{IV.59}$$

We inject (IV.37) that comes from the integration of the damage criterion in the non local case

$$\mathscr{E}(u,D) = \frac{1}{2}\sigma U + \frac{\sigma_c^2}{k}\int_0^L \left(D + \frac{D(D_\sigma - D)}{1-D}\right)\mathrm{d}x, \tag{IV.60}$$

and we use again (IV.41)

$$\mathscr{E}(u,D) = \frac{1}{2}\sigma U + \frac{\sigma_c^2}{k}\int_0^{D_\sigma} \left(\sqrt{\frac{D}{D_\sigma - D}} + \frac{\sqrt{D(D_\sigma - D)}}{1-D}\right)\mathrm{d}D. \tag{IV.61}$$

We have

$$\int_0^{D_\sigma} \sqrt{\frac{D}{D_\sigma - D}}\mathrm{d}D = \frac{D_\sigma \pi}{2}, \tag{IV.62}$$

and

$$\int_0^{D_\sigma} \frac{\sqrt{D(D_\sigma - D)}}{1-D}\mathrm{d}D = \frac{\pi}{2}\left(2 - 2\sqrt{1-D_\sigma} - D_\sigma\right) = \frac{\pi}{2}\left(2 - 2\frac{\sigma}{\sigma_c} - 1 + \frac{\sigma^2}{\sigma_c^2}\right) = \frac{\pi}{2}\left(1 - \frac{\sigma}{\sigma_c}\right)^2. \tag{IV.63}$$

Finally,

$$\mathscr{E}(u,D) = \sigma_c U - \frac{1}{2}\frac{\sigma_c U^2}{\pi\ell\varepsilon_c}. \tag{IV.64}$$

k	ℓ	G_c	c_w	σ_c	ε_c	η	tol
10	0.15	0.1	2.22	1.73	0.163	1e-3	1e-4

Table IV.1: Mechanical and numerical parameters of a FEniCS simulation of an inextensible bar under traction.

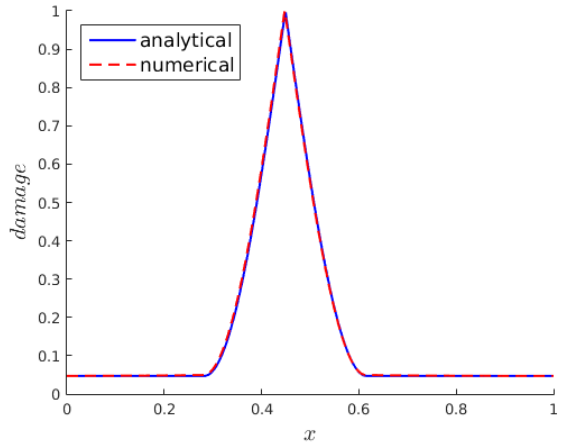

Figure IV.5: Comparison of the analytical and numerical mixed localised response of an inextensible bar under traction. The parameters of this simulation are given in Table IV.1.

IV.2.2 Numerical implementation

The numerical implementation of the above problem was done in the FEniCS library. The standard code for variational fracture in small deformation was used. We had to adapt the expression of the dissipated energy and the elastic energy to our case. Numerically, it is not possible to give an elastic energy that would be infinite when there is no damage. We introduced a parameter, η, that had to be small enough to ensure that the rigidity would be large enough when $\alpha = 0$

$$E(\alpha) = \frac{k}{2}\left(\frac{1}{D(\alpha+\eta)} - 1\right). \tag{IV.65}$$

To be able to observe mixed responses, we used periodic boundary conditions on the damage.

We first checked that the homogeneous response was the same as the analytical one, by using an internal length much greater than the length of the bar L. We then compared the numerical results of the localised and mixed responses with the analytical expressions. Figure IV.5 shows the perfect corroboration of the analytical and numerical results, for a mixed case (which consequently also validates the purely localised case).

Depending on the value of $\varepsilon_c \pi \ell$, the solution can be unstable, and a snap-back can appear. This is the case with the choice of parameters shown in Table IV.2: the internal length is very small, ant the critical deformation ε_c also. On Figure IV.8, the energies are plotted: we see that the damage develops homogeneously for most of the loading, and that at a given

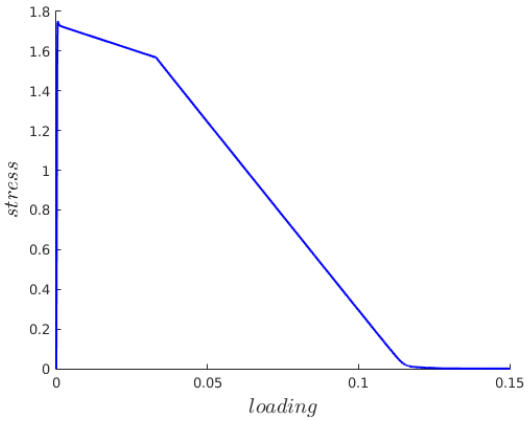

Figure IV.6: Stress evolution of an inextensible bar under traction with an imposed displacement. The parameters used for this simulation are displayed in Table IV.1.

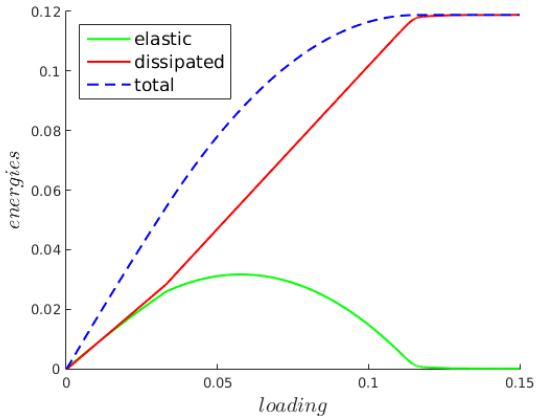

Figure IV.7: Energies evolution of an inextensible bar under traction with an imposed displacement. The parameters used for this simulation are displayed in Table IV.1.

k	ℓ	G_c	c_w	σ_c	ε_c	η	tol
10	0.015	0.1	2.22	1.73	0.052	1e-3	1e-4

Table IV.2: Mechanical and numerical parameters of a FEniCS simulation of an inextensible bar under traction.

critical displacement, the bar suddenly breaks, which results in a jump of the energies.

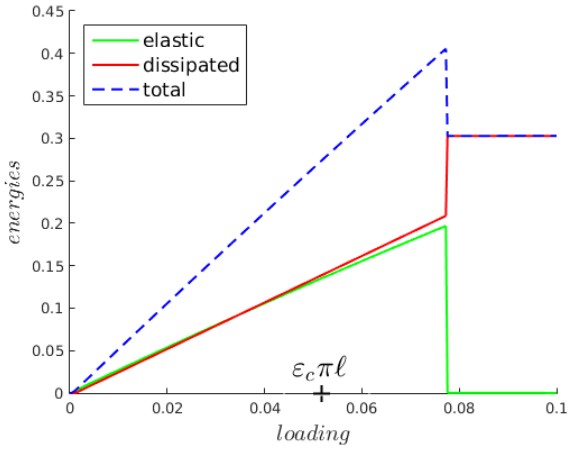

Figure IV.8: Energies evolution of an inextensible bar under traction with an imposed displacement. The parameters used for this simulation are displayed in Table IV.2.

IV.3 Extension to higher dimensions

The generalisation of the behaviour of an inextensible bar in higher dimensions is the incompressible behaviour of any structure of dimension $N > 1$.

IV.3.1 Numerical implementation

Displacement-pressure problem

It is well known that a pure displacement formulation is not adequate to solve an incompressible problem. As was explained in Chapter III, a mixed formulation has to be used. Since we are now working in small deformation, with the FEniCS library, it has to be re-written in this specific situation, and has to be able to deal with pure 2D formulations. We will call N the dimension of the space, that can be either 2 or 3. Again, we note p the hydrostatic pressure such that

$$p = -\frac{\mathrm{tr}\boldsymbol{\sigma}}{N}. \tag{IV.66}$$

Hooke's law gives

$$\begin{aligned} \mathrm{tr}\boldsymbol{\sigma} &= \mathrm{tr}\left[\lambda(\nabla{\cdot}u)\boldsymbol{I} + 2\mu\boldsymbol{\varepsilon}(u)\right] \\ &= (N\lambda + 2\mu)(\nabla \cdot u) \end{aligned} \tag{IV.67}$$

so

$$p = -\frac{N\lambda + 2\mu}{N}\nabla{\cdot}u. \tag{IV.68}$$

Since

$$\lambda = -\frac{2\mu}{3} + \kappa, \tag{IV.69}$$

p is therefore

$$p = -\left(\frac{2\mu(3-N)}{3N} + \kappa\right)\nabla\cdot u. \tag{IV.70}$$

We introduce σ^D the deviatoric part of the stress , such that

$$\boldsymbol{\sigma}^D = \boldsymbol{\sigma} - \frac{\mathrm{tr}\sigma}{N}\boldsymbol{I} \tag{IV.71}$$

$$\boldsymbol{\sigma}^D = 2\mu\boldsymbol{\varepsilon} - \frac{2\mu}{N}(\nabla\cdot u)\boldsymbol{I}. \tag{IV.72}$$

$\boldsymbol{\sigma}$ can be re-written with respect to u et p

$$\boldsymbol{\sigma} = 2\mu\boldsymbol{\varepsilon} - \frac{2\mu}{N}(\nabla\cdot u)\boldsymbol{I} - p\boldsymbol{I}. \tag{IV.73}$$

The equilibrium problem in dimension N takes the form of a system of two equations

$$\begin{cases} -\nabla\cdot\left[2\mu\boldsymbol{\varepsilon} - \dfrac{2\mu}{N}(\nabla\cdot u)\boldsymbol{I} - p\boldsymbol{I}\right] = & r \\ -\dfrac{1}{\dfrac{2\mu(3-N)}{3N} + \kappa}p - \nabla\cdot u = & 0. \end{cases} \tag{IV.74}$$

With the FEniCS library, a mixed formulation can be used by creating a mixed space, and the variational formulation has to be given as a left-hand side and a right-hand side member. In our case, with (v, q) the test functions associated to (u, p), in dimension 2, the left-hand side of the variational formulation is

$$\mathrm{lhs} = 2\mu(\alpha)\boldsymbol{\varepsilon}(u)\boldsymbol{\varepsilon}(v) - \mu(\alpha)\mathrm{div}(u)\mathrm{div}(v) - p\ \mathrm{div}(v) - q\ \mathrm{div}(u) - \frac{1}{\kappa(\alpha) + \dfrac{\mu(\alpha)}{3}}p\ q \tag{IV.75}$$

ant the right-hand side is

$$\mathrm{rhs} = f\ v, \tag{IV.76}$$

with f the internal forces.

Damage problem

The damage problem is given as an energy and its derivatives. The elastic potential

$$\psi(\boldsymbol{\varepsilon}) = \frac{1}{2}\boldsymbol{\sigma}\cdot\boldsymbol{\varepsilon} \tag{IV.77}$$

associated to the displacement-pressure formulation can be written with respect to p, $\nabla\cdot u$, or both p and $\nabla\cdot u$

$$\psi(\boldsymbol{\varepsilon}) = \mu\boldsymbol{\varepsilon}\cdot\boldsymbol{\varepsilon} - \frac{\mu}{N}(\nabla\cdot u)^2 - \frac{\kappa}{2}(\nabla\cdot u)^2 \tag{IV.78}$$

When the dependency of the damage is added to the energy (IV.78), we find the damage criterion (IV.20) by deriving with respect to α. Yet, a mixed formulation is used in order not to use the quantity $\nabla{\cdot}u$ which is close to zero when incompressibility is ensured, and leads to numerical imprecision when it is multiplied by the penalisation coefficient κ. Numerically, we want to be able to give the energy under the form (IV.78) in order to have the correct damage criterion, but without using $\nabla{\cdot}u$. The adopted solution consists in introducing the pressure, multiplied by κ which does not depend on α

$$\psi(\boldsymbol{\varepsilon},\alpha) = \mu(\alpha)\boldsymbol{\varepsilon}{\cdot}\boldsymbol{\varepsilon} - \frac{\mu(\alpha)}{N}(\nabla{\cdot}u)^2 - \frac{\kappa(\alpha)}{2}\left(\frac{1}{\frac{2\mu(3-N)}{3N}+\kappa}\right)^2 p^2. \tag{IV.79}$$

With this expression, the energy gives the damage criterion, and numerical troubles are avoided thanks to the introduction of the pressure. The gradient and Hessian of the damage problem are automatically computed from the total energy.

IV.3.2 2D plate under uni-axial traction

IV.3.2.a Analytical developments

Matched asymptotic expansion

In order to validate the variational formulation established, we need to perform simulations for configurations whose analytical solution is known. Let us consider the case of a 2D plate whose height H is small compared to its length L. In other words, we parametrize it so that its ratio L/H is equal to a small parameter ϵ. Its coordinates are given as x_1 and x_2 coordinates. We set

$$y_1 = \frac{x_1}{\epsilon}, \tag{IV.80}$$

and develop the displacement (u_1, u_2) and the pressure p around ϵ.

$$\begin{cases} u_1^\epsilon(x) = u_1^0(y_1,x_2) & +\epsilon u_1^1(y_1,x_2) & +\epsilon^2 u_1^2(y_1,x_2) & +\ldots \\ u_2^\epsilon(x) = \frac{1}{\epsilon}u_2^{-1}(y_1,x_2) & +u_2^0(y_1,x_2) & +\epsilon u_2^1(y_1,x_2) & +\ldots \\ p^\epsilon(x) = \frac{1}{\epsilon^3}p^{-3}(y_1,x_2) & +\frac{1}{\epsilon^2}p^{-2}(y_1,x_2) & +\frac{1}{\epsilon}p^{-1}(y_1,x_2) & +\ldots \end{cases} \tag{IV.81}$$

We define

$$\boldsymbol{s}^\epsilon = 2\mu\boldsymbol{e}(u^\epsilon) \tag{IV.82}$$

with $\boldsymbol{e}(u^\epsilon)$ the deformation. After writing the incompressibility condition

$$\mathrm{div}(u^\epsilon) = 0, \tag{IV.83}$$

and the equilibrium equation

$$\mathrm{div}(2\mu\boldsymbol{e}(u^\epsilon)) + \nabla p^\epsilon = 0, \tag{IV.84}$$

we find the expressions of u_1^0, u_1^1, u_1^2, u_2^{-1}, u_2^0, u_2^1, p^{-3}, p^{-2}, and p^{-1} with respect to y_1 and x_2, and with undetermined constants.

A similar development in the vicinity of $x_2 = +1$ gives the expression of the displacement and the pressure. The two asymptotic expansions are matched, and finally give the expressions of the displacement and the pressure in the plate. The pressure is

$$p^\epsilon(x) = \frac{3}{2}\mu U \left(\frac{1-x_2^2}{\epsilon^3} + \frac{x_1^2}{\epsilon^3} + \frac{C_2}{\epsilon^2} + \frac{C_1}{\epsilon} \right), \tag{IV.85}$$

with C_1 and C_2 two undetermined constants.

Using the expression of the displacement, we can obtain the expression of the norm of the deviatoric stress, defined by

$$J^\epsilon(x) = \sqrt{(s_{11}^\epsilon)^2 + (s_{22}^\epsilon)^2 + 2(s_{12}^\epsilon)^2} \tag{IV.86}$$

and such that

$$J^\epsilon(x) = 3\sqrt{2}\mu \frac{U}{\epsilon^2} \sqrt{x_2^2 \frac{x_1^2}{\epsilon^2} + \epsilon^2 \left(1 - \frac{x_1^2}{\epsilon^2}\right)^2}. \tag{IV.87}$$

Using the expressions (IV.85) and (IV.87), we can deduce that the pressure reaches its maximum in $x_2 = 0$ and $x_1 = \pm\epsilon$, and the norm of the deviatoric stress reaches its maximum in $x_2 = \pm 1$ and $x_1 = \pm\epsilon$.

Damage initiation

In the case when there is damage, the strain work is

$$W(\boldsymbol{\varepsilon}, \alpha, \nabla\alpha) = \mu(\alpha)\boldsymbol{\varepsilon}^D{\cdot}\boldsymbol{\varepsilon}^D + \frac{\kappa(\alpha)}{2}(\mathrm{tr}\boldsymbol{\varepsilon})^2 + w(\alpha) + w_1\ell^2\nabla\alpha{\cdot}\nabla\alpha. \tag{IV.88}$$

The damage criterion is

$$\mu'(\alpha)\boldsymbol{\varepsilon}^D{\cdot}\boldsymbol{\varepsilon}^D + \frac{\kappa'(\alpha)}{2}(\mathrm{tr}\boldsymbol{\varepsilon})^2 + w'(\alpha) - 2w_1\ell^2\Delta\alpha \geq 0, \tag{IV.89}$$

that can be written in stress space and becomes

$$\mu'(\alpha)\frac{\boldsymbol{\sigma}^D{\cdot}\boldsymbol{\sigma}^D}{4\mu(\alpha)^2} + \frac{\kappa'(\alpha)}{2}\left(\frac{p}{\kappa(\alpha)}\right)^2 + w'(\alpha) - 2w_1\ell^2\Delta\alpha \geq 0. \tag{IV.90}$$

The damage criterion for the initiation of damage is obtained for $\alpha = 0$

$$\frac{\mu'(0)}{4\mu(0)^2}\boldsymbol{\sigma}^D{\cdot}\boldsymbol{\sigma}^D + \frac{\kappa'(0)}{2\kappa(0)^2}p^2 + w'(0) = 0. \tag{IV.91}$$

Using the following standard damage laws

$$\begin{cases} w(\alpha) = w_1\alpha \\ \mu(\alpha) = \mu_0(1-\alpha)^2 \\ \kappa(\alpha) = \kappa_e\dfrac{(1-\alpha)^2}{\alpha} \end{cases} \tag{IV.92}$$

gives the damage criterion for the initiation of damage

$$\frac{\boldsymbol{\sigma}^D \cdot \boldsymbol{\sigma}^D}{2\mu_0} + \frac{p^2}{2\kappa_e} = w_1, \tag{IV.93}$$

that can be written

$$\frac{\boldsymbol{\sigma}^D \cdot \boldsymbol{\sigma}^D}{2\tau_c^2} + \frac{p^2}{2p_c^2} = 1 \tag{IV.94}$$

with $\tau_c = \sqrt{\mu_0 w_1}$ and $p_c = \sqrt{\kappa_e w_1}$.

Since we know from (IV.87) and (IV.85) that the pressure and the square norm of the deviatoric stress are maximum on the lines $x_1 = \pm\epsilon$, we calculate the damage criterion (IV.94) on $x_1 = \pm\epsilon$, and we finally obtain its expression as a function $C(x_2)$

$$C(x_2) = x_2^4 + x_2^2\left(8\epsilon^2\frac{\kappa_e}{\mu_0} - 2\right) + 1 - \frac{8}{9}\frac{w_1\epsilon^6 p}{U^2\mu_0} = 0. \tag{IV.95}$$

The derivative of (IV.95) with respect to x_2 is null in $x_2 = 0$ and $x_2 = \sqrt{1 - 4\epsilon^2\kappa_e/\mu_0}$, and the criterion is maximum for $x_2 = 0$

$$C(0) = 1 - \frac{8}{9}\frac{w_1\epsilon^6\kappa_e}{U^2\mu_0^2}. \tag{IV.96}$$

In addition, the criterion evaluated in $x_2 = \pm 1$ gives

$$C(\pm 1) = 1 + 8\epsilon^2\frac{\kappa_e}{\mu_0} - 2 + 1 - \frac{8}{9}\frac{w_1\epsilon^6\kappa_e}{U^2\mu_0^2}. \tag{IV.97}$$

From (IV.96) and (IV.97), we can deduce that depending on the sign of the quantity $1 + 8\epsilon^2\frac{\kappa_e}{\mu_0} - 2$, the damage criterion can be reached in $x_2 = 0$ or $x_2 = \pm 1$. We therefore have a relation between the ratio of κ_e and μ_0 and the elongation of the plate that determines where damage initiates in the plate: if

$$\frac{\kappa_e}{\mu_0} > \frac{1}{8\epsilon^2}, \tag{IV.98}$$

damage initiates in $x_2 = \pm 1$, otherwise it initiates in $x_2 = 0$.

IV.3.2.b Numerical application

Test without damage

Using the implementation described in IV.3.1, we verify that the analytical and numerical results are in agreement. First, a linear elastic calculation is made, using the parameters given in Table IV.3. The parameter ϵ is 0.1: smaller values have been tested, for which the analytical developments should be more precise, but in the meantime, they lead to numerical imprecision because they trigger very high values of the pressure. The chosen value is therefore a good compromise between the analytical and numerical precision.

L	H	ϵ	h	μ_0	η
2.0	0.2	0.1	0.003	1.0	1e-4

Table IV.3: Parameters of a FEniCS simulation of a 2D plate, in linear elasticity only (no damage). h is the cell size.

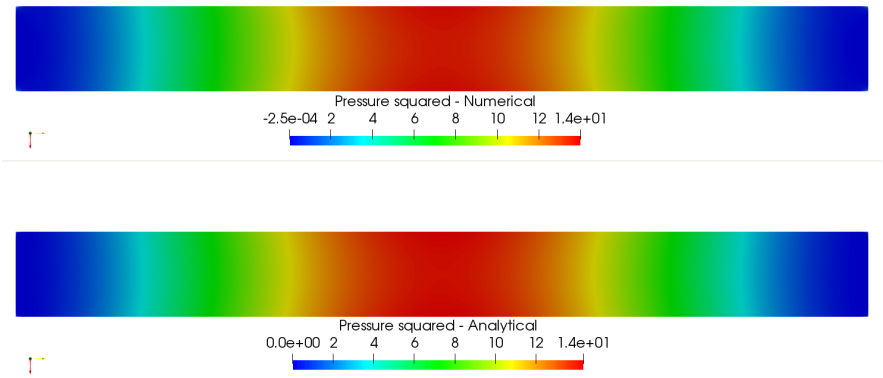

Figure IV.9: Comparison between the numerical and the analytical results of the pressure squared for a plate submitted to traction. The analytical expression of the pressure is given by (IV.85). Numerical tests are performed with $\epsilon = 0.1$ and $\mu_0 = 1.0$.

The results are displayed on Figure IV.9 and show the pressure squared for the numerical (top) and analytical (bottom) calculations. A visible difference lies in the minimum value of p^2: while it is 0 for the analytical results, it is of the order e-04 for the numerical results, which is due to the numerical imprecision. The analytical expressions do not render the stress concentration that can be observed in the angles of the sample, as can be seen more easily on Figures IV.10, which displays lineouts of the pressure p on the lines $x_1 = \epsilon$ and $x_1 = 0$. On the line $x_1 = 0$, the analytical and numerical results are very close, and on the line $x_1 = \epsilon$, they differ only on the extremities, where the numerical results exhibit a stress concentration. Globally, the tests performed validate both the numerical implementation and the analytical developments.

Analytical and numerical damage criterion

In this part, we compare the analytical and numerical values of the damage criterion, and study how the repartition of the pressure and the deviatoric stress influence the initiation of damage. On Figure IV.11a, the expression of $(\boldsymbol{\sigma}\cdot\boldsymbol{\sigma})/\mu_0 + p^2/\kappa_e$ is plotted, for different values of κ_e, using $\epsilon = 0.1$. The results are in agreement with the condition (IV.98): if $\kappa_e/\mu_0 \geq (8\epsilon^2)^{-1}$, damage initiates in $x_2 = \pm 1$, where the deviatoric stress is the highest. If $\kappa_e/\mu_0 = (8\epsilon^2)^{-1}$, the damage criterion is reached both in $x_2 = \pm 1$ and $x_2 = 0$, and if

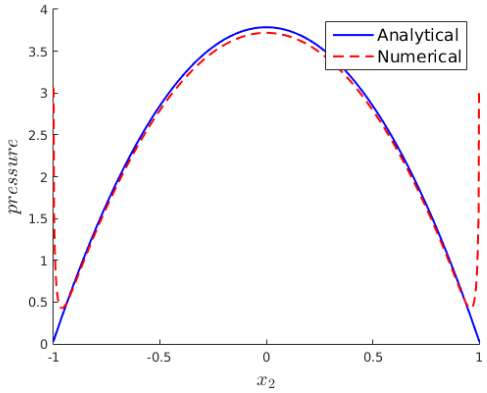

(a) Pressure p on the line $x_1 = \epsilon$.

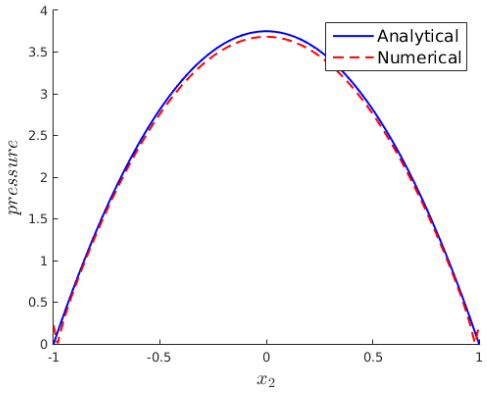

(b) Pressure p on the line $x_1 = 0$.

Figure IV.10: Comparison between the numerical and the analytical results of the pressure on respectively the lines $x_1 = \epsilon$ and $x_1 = 0$ for a plate submitted to traction. The analytical expression of the pressure is given by (IV.85). Numerical tests are performed with $\epsilon = 0.1$ and $\mu_0 = 1.0$.

L	H	ϵ	ℓ	h	μ_0	η
1.0	0.1	0.1	$H/10$=0.01	0.004	1.0	$\kappa_e/1000$

Table IV.4: Parameters of a FEniCS simulation of a damaging 2D plate submitted to uniaxial traction.

$\kappa_e/\mu_0 \leq (8\epsilon^2)^{-1}$, damage initiates in the middle ($x_2 = 0$), where the pressure is the highest.

Yet, we have seen on Figure IV.10a, that the numerical results show a stress concentration in the edges, that do not appear in the analytical expression. Therefore, we can expect the numerical damage criterion to be slightly different than the analytical one. On Figure IV.11b, a comparison is made between the analytical and numerical damage criterion, in the case $\kappa_e/\mu_0 = 1.0$ and $\epsilon = 0.1$. We can see that indeed, the damage criterion is not maximum in the same zones: because of the numerical stress concentration on $x_2 = \pm 1$, the criterion is reached in the edges, while the analytical developments foresee a damage initiation in the middle.

Tests with damage

Numerical simulations with damage are performed for various values of κ_e. The parameters used for these simulations are listed in Table IV.4. We keep the value of 0.1 for ϵ. The quasi-incompressibility of the material is ensured by the fixed value of $\kappa_0 = \kappa/\eta = 1000$: since κ_e varies for the needs of the tests, the numerical parameter η is also changed to keep a fixed ratio of the compressibility coefficient κ_0. The internal length is one tenth of the height of the rectangle, and the mesh size is $h = \ell/2.5$. The mesh is not refined more, because of

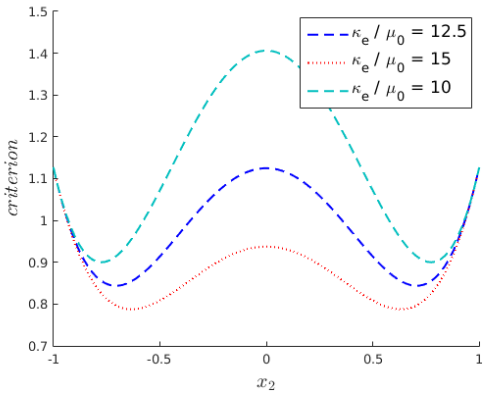

(a) Three different values of κ_e are tested to make the ratio κ_e/μ_0 vary. If $\kappa_e/\mu_0 = 12.5 = 1/(8\epsilon^2)$, the damage criterion is maximum in the middle and on the edges.

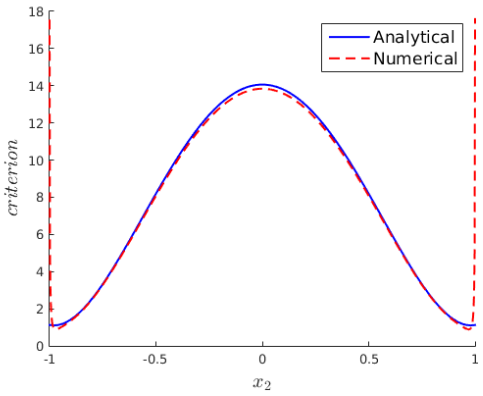

(b) Comparison between the analytical and numerical value of the damage criterion, for $\kappa_e/\mu_0 = 1.0$. The analytical results show that the damage criterion is reached in the middle, while the numerical results show that it is reached on the edges.

Figure IV.11: Damage criterion for the 2D plate under traction on the line $x_1 = \epsilon$, for $\epsilon = 0.1$, $\mu_0 = 1.0$.

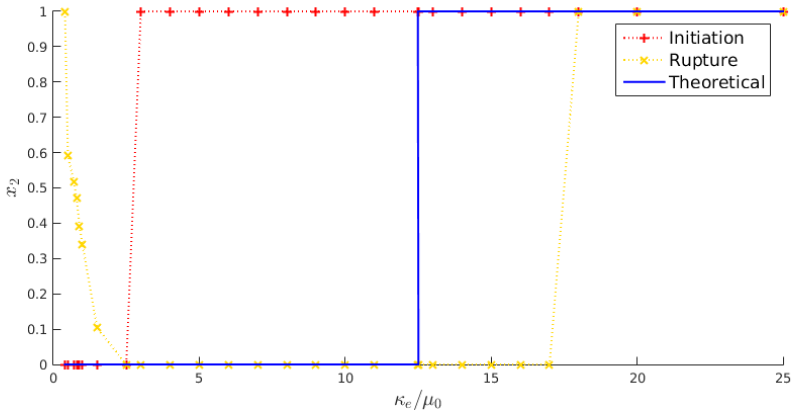

Figure IV.12: Comparison of the analytical prevision of the initiation of damage (blue), and the numerical results (damage initiation and rupture). The tests are performed for different values of κ_e/μ_0.

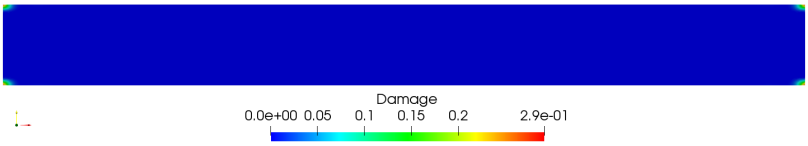

(a) Initiation of damage in the four corners. $U = 0.007$.

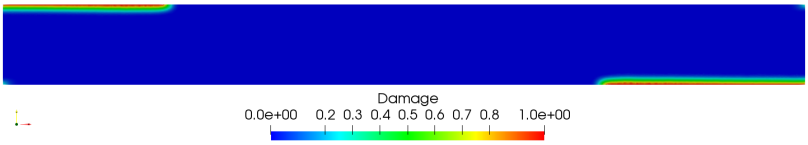

(b) Rupture in two corners. $U = 0.0072$.

Figure IV.13: Damage and rupture of a 2D plate submitted to uni-axial traction. $\kappa_e = /\mu_0 = 20$.

the cost of the simulations that is already quite high. No boundary conditions of damage are applied.

As was explained above, the initiation of damage can occur either in $x_2 = \pm 1$ or $x_2 = 0$, always on the lines $x_1 = \pm\epsilon$. We have seen that due to the numerical stress concentration, damage may occur in $x_2 = \pm 1$ when the theoretical development predicts it to occur in $x_2 = 0$. The results displayed on Figure IV.12 show that this is the case: in the simulations (yellow), damage initiates on the edges, for relatively small values of κ_e (*i.e.* values such that $\kappa_e/\mu_0 < 1/8\epsilon^2$). Yet, an interesting phenomenon then takes place: for this values of κ_e, while damage initiates in the corners, the rupture –when α_{max} is very close to 1, occurs in the middle (red).

Although the analytical damage criterion only gives us the place where damage first initiates, and not the place where rupture occurs, we can observe on Figure IV.12 that the numerical results as for the place where rupture occurs, are closer to the analytical calculations for damage initiation than the numerical results for the initiation. Eventually, the numerical stress concentration that triggers a different initiation of damage, disappears when damage grows.

An example of a simulation performed with the parameters given in Table IV.4, and with $\kappa_e/\mu_0 = 20$ can be seen on Figure IV.13: in this situation, damage initiates in the four corners, and rupture occurs in two of the corners. The process of rupture is brutal: damage jumps from 0.29 to 1.0 from one time step to another. The rupture pattern is not always similar to the one of Figure IV.13b. In some cases, two cracks appear on the corners of the same line $x_1 = \pm\epsilon$.

Figure IV.14 shows the results obtained with $\kappa_e/\mu_0 = 17$. In this case, damage first begins in the corners of the plate, but the rupture occurs in the middle of the sample. Again, rupture is brutal: damage jumps from 0.3 to 1.0. In all the situations when rupture occurs

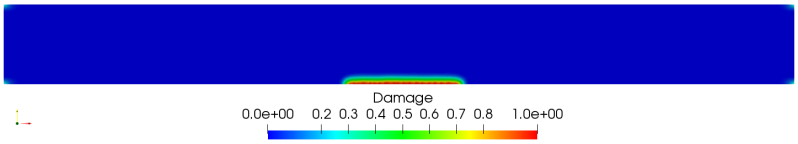

Figure IV.14: Damage and rupture of a 2D plate submitted to uni-axial traction. $\kappa_e = /\mu_0 = 17$, $U = 0.0072$.

in the middle of the edges, there is always only one crack, either on top or on the bottom of the plate.

Finally, an example with a ratio $\kappa_e/\mu_0 = 1.0$ is shown on Figure IV.15. The damage is taken for six growing time steps, and the scale changes on each image. We can see that damage first begins in the middle of the rectangle, where the pressure is high. It then widens, and after some time steps, four distinct spots of damage appear (Figure IV.15c). Finally, two of these four spots continue to develop, and lead to rupture on opposite sides of the rectangle (Figures IV.15d to IV.15f).

IV.3.3 Test inducing bi-axiality

IV.3.3.a Geometry

After validation of the mixed implementation with damage, tests that would enhance the role of the pressure had to be performed. We had to find simple geometries such that the loading would trigger pressure development, as well as deviatoric stresses, but not in the same zones of the sample. We chose to work on the geometry displayed on Figure IV.16: it is made of a rectangle of length L and height H, minus two half circles of diameter $D = H$. On the green boundary, a null displacement on the two components is imposed, while a growing x displacement is imposed on the red opposite boundary. The top and bottom edges are free of stress. Dirichlet boundary conditions of null damage are imposed on the green and red boundaries.

With such a geometry, zones of high pressure and high deviatoric stresses appear in different zones, as can be observed on Figure IV.17. The pressure is very high near the poles of the half-circles and has a conic shape, while the deviatoric part of the stress is high in the middle and on four borders, which could be seen as an x-shape.

The boundary conditions on α are such that there is no damage on the boundaries, and consequently we can expect that when the damage should initiate in zones of high deviatoric stresses, it would then develops in the middle of the sample, and not and the edges. This choice is based on the fact that we want to observe damage initiation and rupture in the bulk, and not on the boundaries, that would rather correspond to delamination.

Thus, the values of the pressure and the deviatoric stress that are of interest are situated on the x-line of $y = 0$. Figure IV.18a shows a lineout of theses quantities and it is very

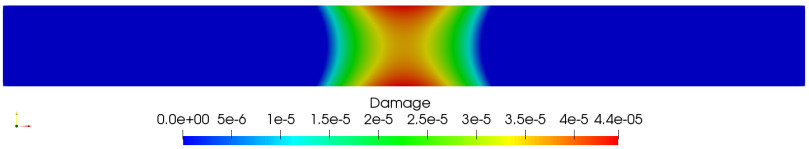

(a) $U = 0.0018$.

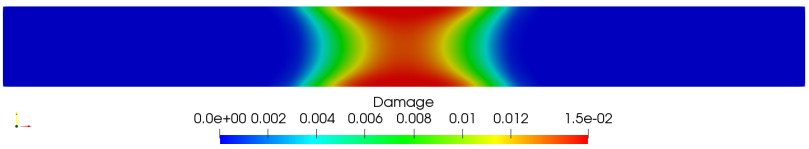

(b) $U = 0.0028$.

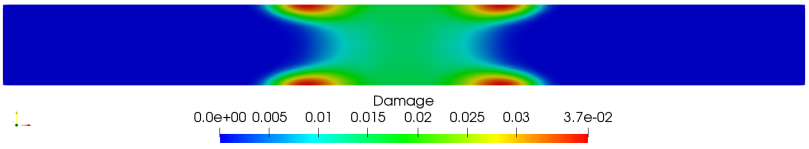

(c) $U = 0.0034$.

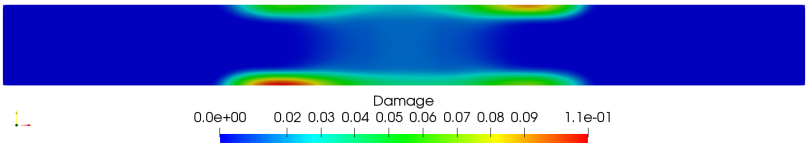

(d) $U = 0.0046$.

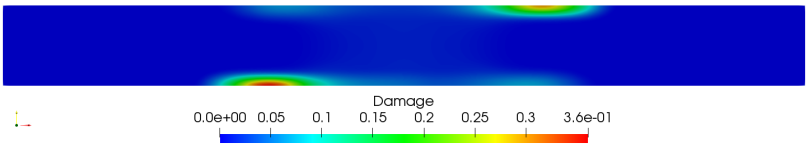

(e) $U = 0.0058$.

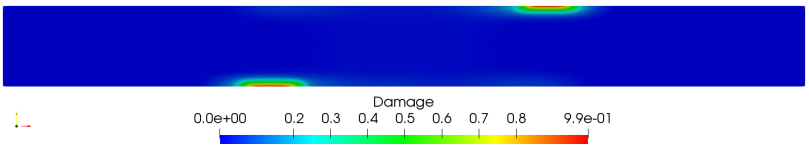

(f) $U = 0.007$.

Figure IV.15: Damage and rupture of a 2D plate submitted to uni-axial traction. $\kappa_e = /\mu_0 = 1.0$. *In order to improve visibility, the scale is changed between each image.*

clear that the pressure reaches its maximum on the edges, and the deviatoric part in the middle. The damage criterion (IV.20) is a combination of these quantities divided by μ_0 and κ_e. Therefore, the damage will always be reached either on the edges or in the middle, as is shown on Figure IV.18b where the criterion is plotted for different ratios of κ_e/μ_0. There is a special case when the damage criterion is very flat, and we can expect the damage to initiate in any zone of the line.

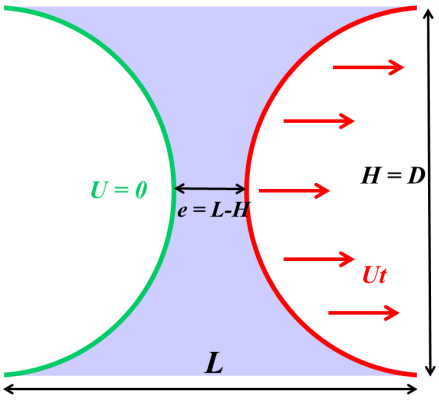

Figure IV.16: Geometry of a 2D sample

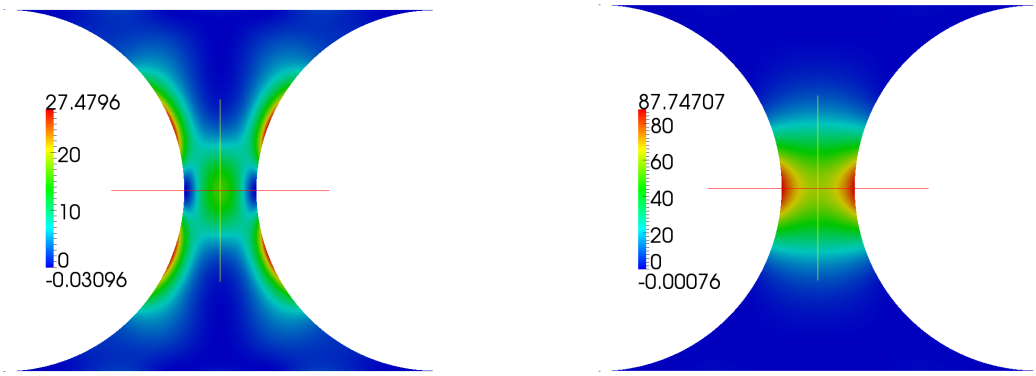

(a) Pressure squared. *(b) Square norm of σ^D.*

Figure IV.17: Repartition of the hydrostatic pressure and the deviatoric stress on a sample at a given time step.

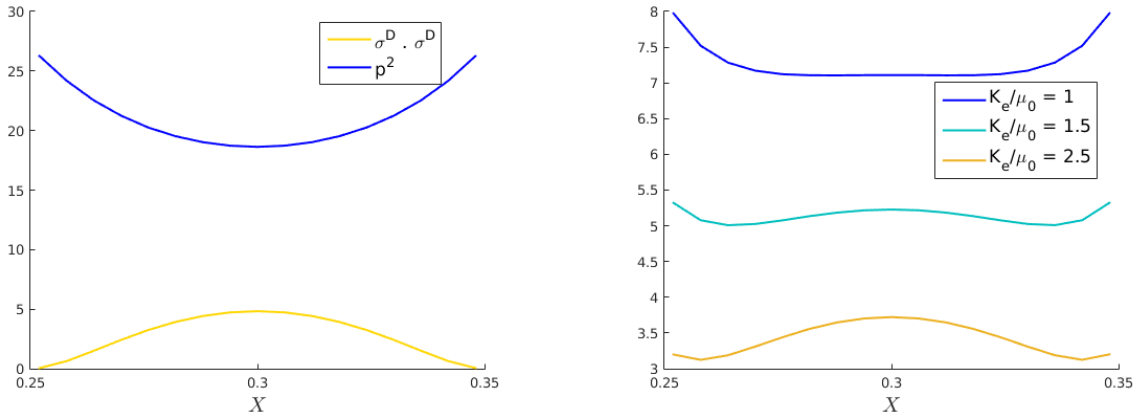

(a) Lineout of the pressure squared (blue) and the square norm of the deviatoric stress (yellow).

(b) Lineout of the damage criterion (IV.20) for three ratios of κ_e/μ_0.

Figure IV.18: Lineout on $y = 0$ of Figure IV.17 at a given time step.

IV.3.3.b Results

After performing simulations in linear elasticity in order to be able to predict where the damage would initiate, simulations with damage were done. The geometry was chosen such that $L = 0.6$, $H = 0.5$ and $e = L - H = 0.1$. The ratio e/D was then of 0.2. The internal length was chosen as one tenth of the gap between the half circles, and the mesh size was one fourth of the internal length. μ_0 was fixed to the value 3.3, and the coefficient κ_e was taken in a range of order ten. The parameter η that ensures quasi-incompressibility was 1e-3: when trying to figure out the best value for η, we noticed that too small values (of order 1-4,5, etc) lead to numerical imprecision. All these parameters are listed in Table IV.5. In order to bring out the main features of the new damage model that we proposed for $\kappa(\alpha)$, we investigated the influence of various parameters on the damage initiation and the rupture patterns.

Influence of G_c

Since we are working in linear elasticity, the ratio of the maximum value of the pressure on the deviatoric stress is constant with respect to the loading. Consequently, for a fixed value of κ_e and μ_0, the damage initiation and the rupture pattern are the same in the reference configuration, whatever the load at which damage and rupture occur. In small deformation, G_c does not play any role on the zone where damage initiates, and we are free to chose small values of G_c to perform our simulations.

L	H	e/D	ℓ	h	μ_0	κ_e	η	tol
0.6	0.5	0.2	e/10	$\ell/4$	3.3	?	1e-3	1e-4

Table IV.5: Parameters of a FEniCS simulation of a specimen IV.16 under uni-axial traction. The value of κ_e changes in order to study its influence over the results.

Influence of ℓ

Another material parameter that has to be investigated is the internal length and its influence on the damage initiation and rupture. ℓ controls the width of the damage band, but if its value stays small enough regarding the gap between the two half circles, it does not have any significant influence on the results, except that it does change the time for which damage and rupture occur.

Influence of κ_e

Now that we are free to chose any value of G_c and ℓ without risking to interfere with the results, we can study the new parameter that was introduced with the model, κ_e. We use the parameters listed in Table IV.5, and all are fixed except κ_e. First, we studied its influence on the critical elongations for which damage and rupture occur. This elongation in the gap is defined as

$$\lambda_g = \frac{e + U_t}{e} \tag{IV.99}$$

where U_t is the imposed displacement on the right boundary (see IV.16). The results are displayed on Figure IV.19, and show several trends. First, when κ_e increases, the elongation for which damage begins to initiate increases. This is consistent with the damage criterion and the linear elastic study that was made and showed that the maximum value of the pressure was always greater that the one of the deviatoric stress: when κ_e increases, the influence of the pressure in the damage criterion decreases, and the deviatoric part has to be greater, hence the bigger elongation.

If this trend is easily understandable, this is not the case for the evolution of the critical elongation for rupture: Figure IV.19 shows indeed that the critical elongation first decreases when κ_e increases, and after reaching a minimum, it increases. It seems natural that it could indeed not decrease forever since the critical elongation for rupture has to be greater that the critical elongation for rupture. The minimum is reached for a value $\kappa_e/\mu_0 = 1.5$ and corresponds to the value for which damage begins to develop in the zone of deviatoric stress. This curve can therefore be decomposed in two phases: for $\kappa_e/\mu_0 < 1.5$, the damage and the rupture happen in zones of high pressure, while for $\kappa_e/\mu_0 \geq 1.5$, the damage and rupture happen in zones of deviatoric stress. Figure IV.20 gives some more hints about the phenomenon that takes place: for rupture due to deviatoric stress, there are only one or two time steps between the moment when damage initiates and a crack appears, and we have a

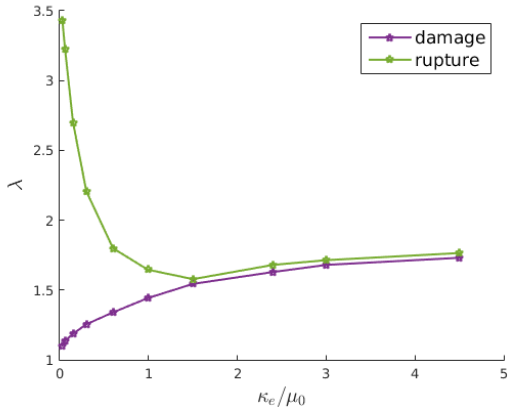

Figure IV.19: Elongation of the gap for which damage initiates (purple) and fracture occurs (green), for different ratios of κ_e/μ_0.

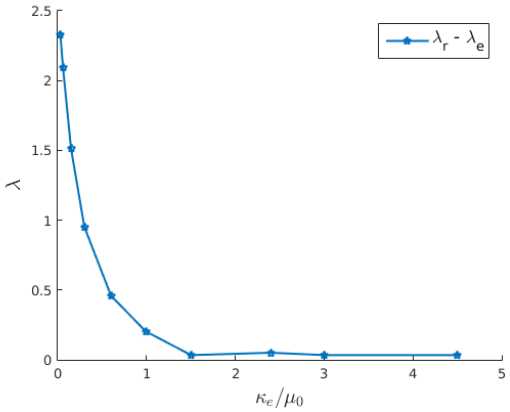

Figure IV.20: Difference between the elongation of the gap for which rupture occurs and damage initiates, for different ratios of κ_e/μ_0.

typical case of brittle fracture. On the contrary, when rupture happens in zones of pressure, the rupture is not sudden, and the damage develops progressively. The smaller κ_e is, the more the pressure plays a role in the initiation of damage, and the less the rupture can be qualified of "brittle". These curves enabled us to see that for incompressible materials, two mechanisms of damage exist that lead to two different types of rupture: one is brittle fracture while the other is the fracture triggered by high hydrostatic pressures. The latter is usually referred to in the literature as "hydrostatic damage".

To bolster the explanations above, we plotted on Figure IV.21 the difference between two successive values of the maximum damage, when 1 is reached. The curve can be decomposed in three distinct parts: in yellow, the points that correspond to brittle fracture (from on time step to the other, damage jumps from 0 to 1), in red, the points that correspond to hydrostatic damage, and in yellow, points for which we will have an explanation later. For the hydrostatic and brittle fracture, the results match the ones of the curves IV.19 and IV.20: the more time it takes for damage to go from zero to one, the less there is a jump when a crack appears.

In order to illustrate the influence of the coefficient κ_e over the initiation of damage and the rupture, we go back to the values used on Figure IV.18b and perform simulations to verify that our predictions were accurate. This figure shows that for a ratio $\kappa_e/\mu_0 = 1$, damage initiates in zones of high hydrostatic pressure, for $\kappa_e/\mu_0 = 1.5$, damage can initiate at any point on the line $y = 0$ and for $\kappa_e/\mu_0 = 2.5$, damage initiates in zones of high deviatoric stress. The results of the simulation are displayed on Figures IV.22, IV.23, and IV.24 respectively, and the initiation of damage meets perfectly well our expectancies. As for the rupture pattern, it is in adequacy with the initiation: a crack appears where the damage initiated. On these figures, the damage scale changes between the initiation of damage and the rupture (left and

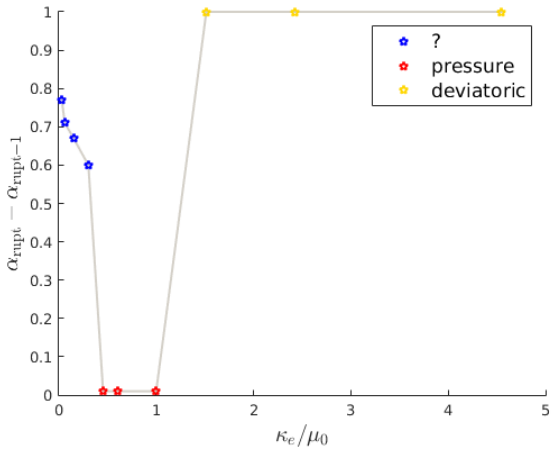

Figure IV.21: Difference of the values of the maximum damage between the time step for which $\alpha_{max} = 1$ and its previous time step. For an example, in yellow, points for which the difference is 1, that means that from one time step to another, damage suddenly went from 0 to 1, and the rupture process is essentially due to the deviatoric part of the stress. On the contrary, in red, points for which damage grew very smoothly, accounting for the pressure.

right). The irreversibility constraint is applied, and there is no healing in this situation. On Figure IV.22, we observe the development of two spots of damage near the poles of the half circles, followed by a loss of symmetry when rupture occurs which is likely due to minimisation reasons: one crack rather than two minimise better the energy of the sample. The case shown on Figure IV.23 is a perfect example of the pressure and the deviator having an influence over the initiation of damage. In that situation, we are not able to predict where the sample will break (near the poles or in the middle), and only experiments or numerical tests can show the outcome of the test.

There is a situation that deserves a closer eye on it, that happens for small values of κ_e - respectively to μ_0. In the case where $\kappa_e = \mu_0$, we have seen in the damage criterion and on Figure IV.18b that the damage initiates in the zones of high pressure. So there is no reason *a priori* to chose values of κ_e such that $\kappa_e/\mu_0 < 1$, unless we want to enhance the role of the pressure. In that case, we have observed that the damage does indeed initiate in the zones of high pressure, but that after some time steps, it also develops in the middle of the sample to finally generate a crack in the middle of the sample. These steps can be seen on Figure IV.25.

To conclude this study on the parameter κ_e, we first recall that this parameter has been introduced for the needs of a model that would allow the pressure to play a role in the initiation of damage. This parameter does not, in any case, control the incompressible behaviour of the material, since this task is devoted to the η parameter that keeps a fixed ratio $\kappa_0 = \kappa_e/\eta$. The only role of κ_e appears in the damage criterion, and it controls the influence

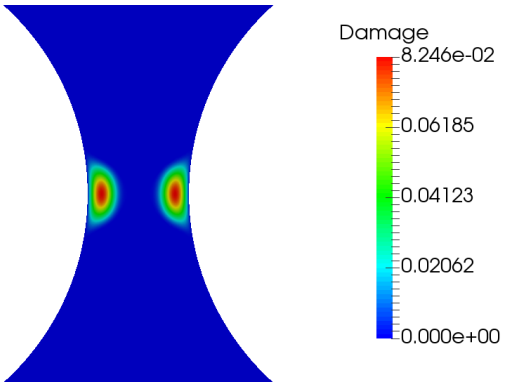

(a) Initiation near the poles.

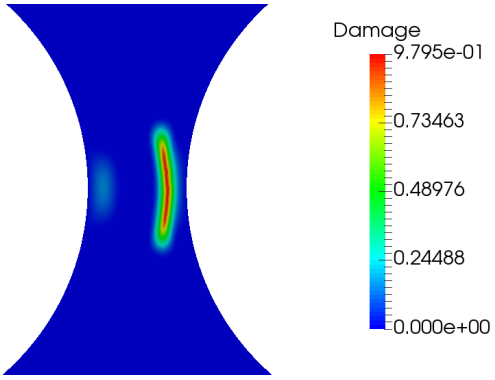

(b) Rupture near the poles.

Figure IV.22: $\kappa_e/\mu_0 = 1.0$.

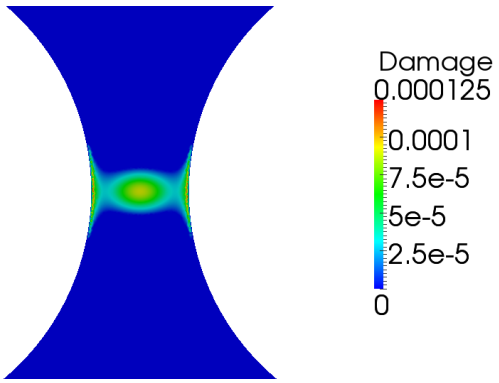

(a) Initiation near the poles and in the middle.

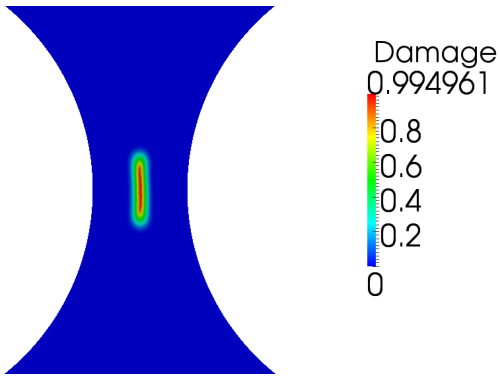

(b) Rupture in the middle.

Figure IV.23: $\kappa_e/\mu_0 = 1.5$.

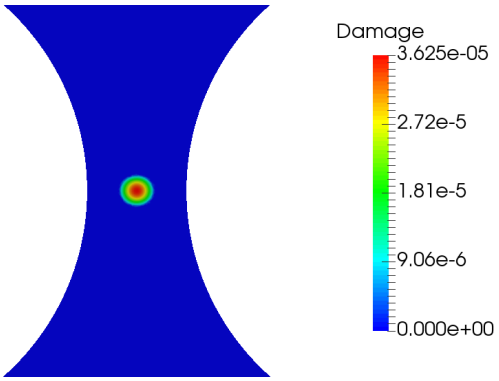

(a) Initiation in the middle.

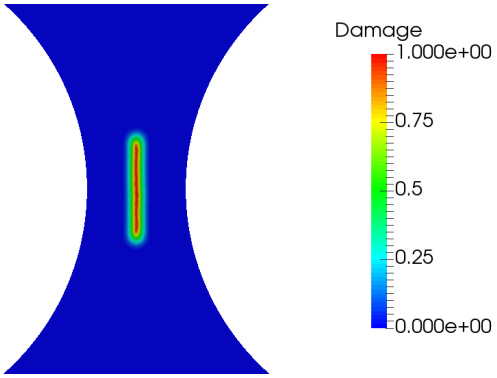

(b) Rupture in the middle.

Figure IV.24: $\kappa_e/\mu_0 = 2.5$.

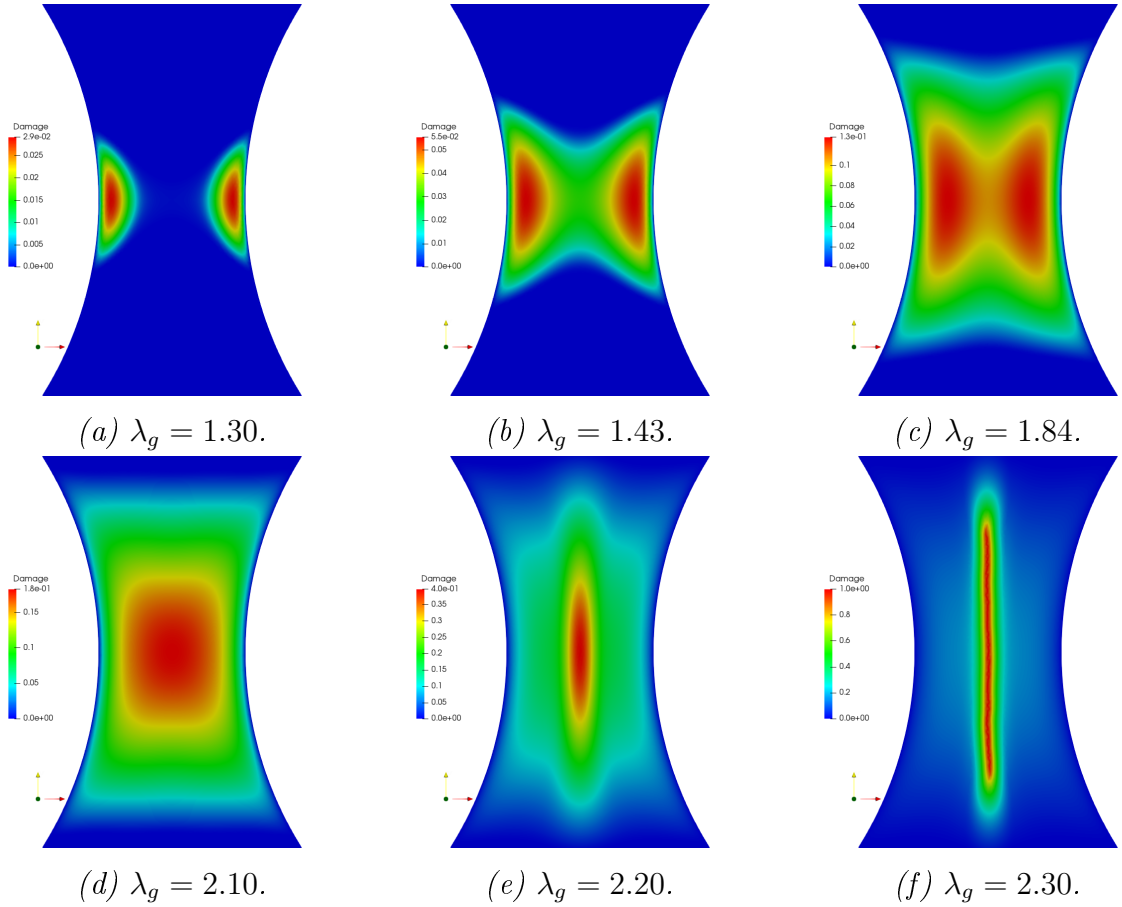

(a) $\lambda_g = 1.30$. (b) $\lambda_g = 1.43$. (c) $\lambda_g = 1.84$.

(d) $\lambda_g = 2.10$. (e) $\lambda_g = 2.20$. (f) $\lambda_g = 2.30$.

Figure IV.25: Case with $\kappa_e/\mu_0 = 1/3$. The damage initiates in the zones of high hydrostatic pressure, develops progressively towards the zone of high deviatoric stress, and a crack finally appears in the middle of the specimen.

of the pressure in it. Its physical meaning is hardly justifiable, because it is not *a priori* a physical parameter of a material. Thus, it has to be calibrated so that simulations concord with experiments, and this is the aim of the next section.

IV.4 Comparison with experiments

In 1984, Gent and Park [21] produced experiments to show two failures phenomena of elastomers, the cavitation and the debonding. The used specimens containing one or two rigid inclusions and observed the formation of cavities near the poles of the inclusions. This famous experiment has been revisited very recently by Poulain, Lefèvre, Lopez-Pamies and Ravi-Chandar in [56]. In their work, they use various PDMS elastomer samples containing two rigid inclusions, and they study the nucleation of cavities and their transition to cracks when a quasi-static load is applied. In this section, we will compare our numerical simulations to their results for a PDMS composition of 45:1 which does not exhibit strong hardening in

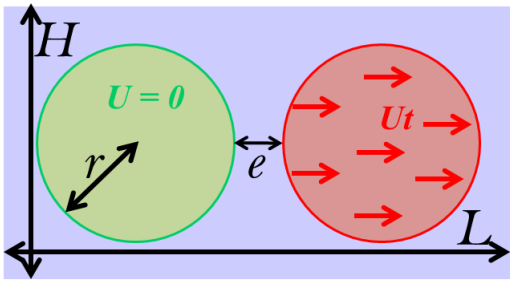

(a) Geometry: the length and height of the plate are fixed. The ratio $e/(2r)$ can be varied. The displacement U_t is applied on the right inclusion.

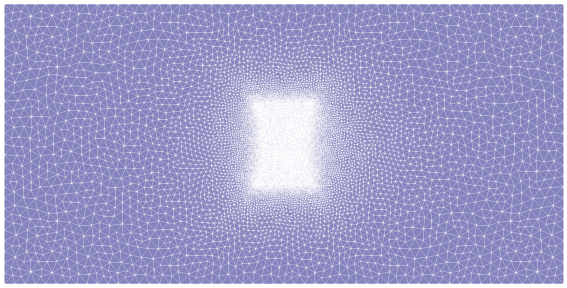

(b) Mesh: the zone between the two inclusions is refined, and the size of the mesh elements is determined from the size of the internal length.

Figure IV.26: Geometry, boundary conditions and mesh of a 2D plate with rigid inclusions.

L	H	e	$D = 2r$	ℓ	h	μ_0	κ_e	η	tol
0.8	0.4	0.063	0.3	e/10	$\ell/4$	3.3	3.3	1e-3	1e-4

Table IV.6: FEniCS simulation of a specimen IV.26 under uni-axial traction.

uni-axial tension for stretches below 4. The ratio of the gap between the two inclusions and the diameter of the beads was 0.210.

We will restrict our comparison to the initiation of damage and the transition to cracks. Healing is out of the scope of this work because the irreversibility condition of the damage evolution precisely prevents this kind of phenomenon, and more complex theories are required to treat it. It was done recently by Kumar, Francfort and Lopez-Pamies in [33].

To be the closest to the real conditions of the experiment, we use a 2D geometry shown on Figure IV.26 made of a rectangle of dimension $L \times H$ containing two circles of diameter $D = r$. The gap between the two circles is e, and the mesh in this zone is refined. The geometrical, mechanical and numerical parameters of the "matrix" are listed in Table IV.6. The inclusions are also made of an elastic material whose rigidity is one hundred times the one of the matrix. The ratio e/D is equal to 0.21 in order to have the same as in the experiment we want to compare with. In the experiments of [56], the beads are directly glued into metallic grips to facilitate the hold of the specimen in the test machine clamps. We therefore applied boundary conditions on the rigid inclusions, and not on the left and right boundaries of the specimen. In addition, this enables us to quantify very precisely the elongation in the gap between the two inclusions.

In the experiments of both Gent and Park, and Poulain, Lefèvre, Lopez-Pamies and Ravi-Chandar, the nucleation of damage happens at the poles of the inclusions, and not between them. This information enables us to chose κ_e such that the pressure will be preferred over the deviatoric stress in the initiation of damage. This is why in Table IV.6, $\kappa_e = \mu_0$.

A quasi-static test is performed, and the results for successive time steps are shown on Figure IV.27. Two spots of damage first develop symmetrically at the poles of the inclusions (Figures IV.27a and IV.27b), and the maximum value of the damage is around 1.5e-01. At this stage, the spots of damage already have different shapes when seen in the reference configuration or the deformed configuration. In a second phase (Figures IV.27c and IV.27d), one spot continues growing while the second stops growing, and the maximum value of the damage in the bigger spot is now around 3.7e-01. The smaller spot of damage does not decrease or heal, because the irreversibility condition is enforced. The image could yet give this impression because the damage scale is changed between two time steps. In the last images (Figures IV.27e and IV.27f), damage in the right spot reaches the value 1, and a crack has appeared in the reference configuration. In the deformed configuration, the crack has a conical shape. In the following time steps that are not displayed here, the crack grows until the specimen is broken into two pieces.

The comparison between the experimental results and the numerical tests can be done with Figure IV.27f and Figure IV.28. We cannot expect the results to be quantitatively the same because in one case, polymers are used, and in the other case, a linear elastic material is used. Yet, qualitatively, we can see that they are very close: in the deformed configuration, both exhibit a cone-shape cavity whose base is along the pole of one inclusion. This cone-shape cavity is in fact a crack when seen in the reference configuration. We can deduce that to obtain the same results, we need to nucleate a vertical crack near the pole of the inclusions.

In the experiments of [56], a second cone-shaped cavity appears after the first one during the loading. In our simulations, we do not observe such a behaviour: after a crack has appeared near one of the poles, it grows catastrophically and leads to rupture. There are many explanations to this phenomenon, one of them is that the sample used in the experiments may not be perfectly symmetric, or the matrix not entirely homogeneous.

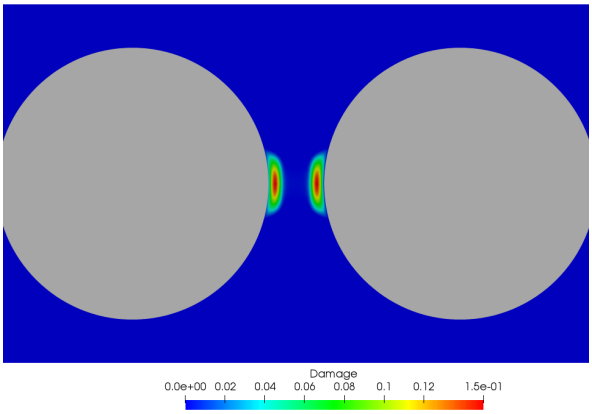

(a) Reference configuration – $\lambda_g = 1.83$.

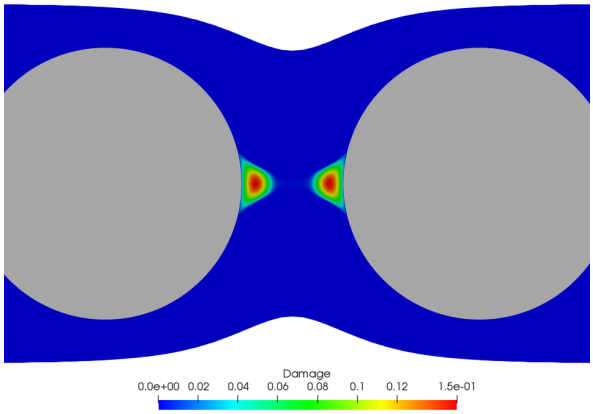

(b) Deformed configuration – $\lambda_g = 1.83$.

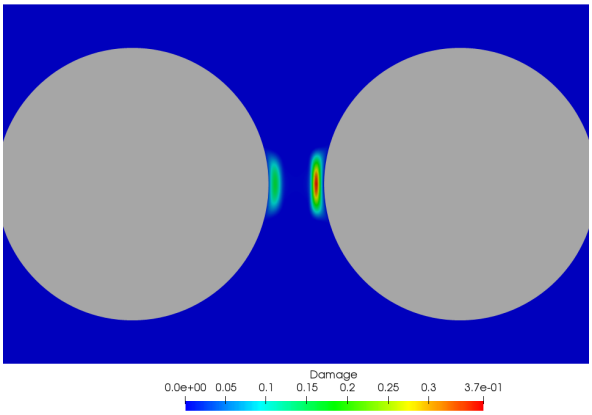

(c) Reference configuration – $\lambda_g = 1.90$.

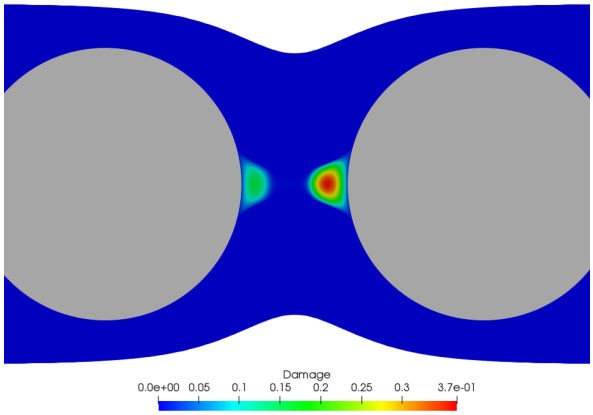

(d) Deformed configuration – $\lambda_g = 1.90$.

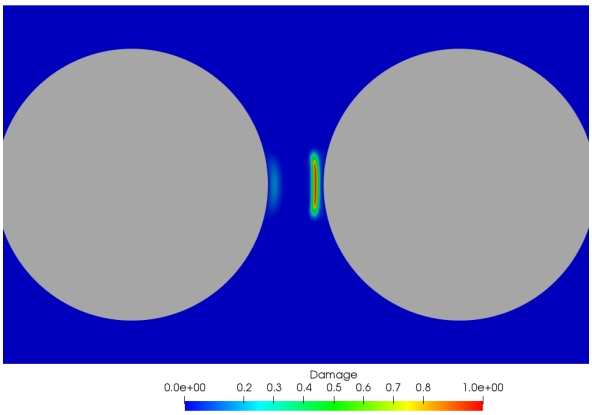

(e) Reference configuration – $\lambda_g = 1.92$.

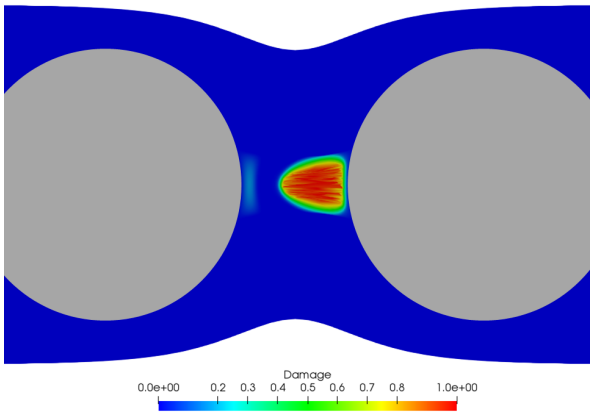

(f) Deformed configuration – $\lambda_g = 1.92$.

Figure IV.27: Rupture of a linear elastic specimen with two rigid inclusions under traction. Damage in the initial and actual configurations for different loading states.

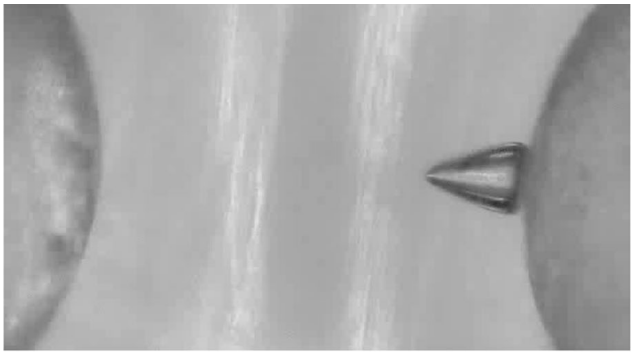

Figure IV.28: Image from the experiments of [56], taken during the traction test on a PDMS matrix containing two rigid beads. The image shows the nucleation of a cone-shaped hole, for an elongation of the gap between the beads of $\lambda_g = 2.92$. Later in the experiment, a second cone-shaped cavity forms on the pole of the left bead, that grows catastrophically while the first one heals, and leads to the rupture of the specimen.

IV.5 Large deformation

These experiments were also carried out in large deformation, with the MEF++ [16] code already used in the Chapter III. In this code, the variational formulation of the problem has to be decomposed into pieces called "formulation terms". With the new damage law for $\kappa(\alpha)$, the displacement problem is not changed, but the variational formulation of the damage problem is slightly different.

The volumetric term in the hyperelastic potential is now

$$U(J,\alpha) = \frac{\kappa_e}{2(\alpha+\eta)}(J-1)^2 \tag{IV.100}$$

whose derivative at point α in an admissible direction β is

$$U'(J,\alpha)(J,\beta) = -\frac{\kappa_e}{2(\alpha+\eta)^2}\beta(J-1)^2. \tag{IV.101}$$

Replacing $(J-1)$ by $p/\kappa(\alpha)$ eliminates the coefficient η and finally gives

$$U'(J,\alpha)(J,\beta) = -\frac{p^2}{2\kappa_e}\beta \tag{IV.102}$$

which is a formulation term very easy to implement. As for the isochoric part of the Mooney-Rivlin hyperelastic energy, if we write for $\alpha = 0$

$$\psi_0 = \psi_{iso_0} + U_0(J) = C_{10}(\bar{I}_1 - 3) + C_{01}(\bar{I}_2 - 3) + \frac{\kappa_0}{2}(J-1)^2, \tag{IV.103}$$

we can express ψ_{iso_0} with respect to ψ_0 and p

$$C_{10}(\bar{I}_1 - 3) + C_{01}(\bar{I}_2 - 3) = \psi_0 - \frac{p^2}{2\kappa_0}. \tag{IV.104}$$

L	H	e/D	ℓ	h	κ_0	κ_e	C_{10}	C_{01}	k_{ell}	tol
0.6	0.5	0.2	0.02	$\ell/4$	100	3.3	1.32	0.33	1e-3	1e-4

Table IV.7: Parameters of a 2D simulation carried out in large deformation on a U-shaped geometry IV.16.

Keeping in mind that the relation between the two coefficients C_{10} and C_{01} of the Mooney-Rivlin law and the Lamé coefficient is μ: $\mu = 2(C_{10} + C_{01})$, we use parameters that are equivalent to the ones used in small deformation.

We use once more the geometry IV.16, with the material and numerical parameters listed in Table IV.7. κ_e is taken such that the ratio $\kappa_e/(2(C_{10} + C_{01})) = 1$. The influence of the parameters of the models having already been treated in the framework of small deformation, it is not useful to do it again, and this is why we chose to show only one example of a typical result in large deformation on Figure IV.29. The results are shown in the reference and deformed configuration, and are similar to those obtained in small deformation. The spots of damage and the crack in the reference configuration become cone-shaped in the deformed configuration. We can notice that this cone is sharper than the one in IV.27f obtained in small deformation, and corresponds better to the cavity shown on Figure IV.28.

Remark: tests were also performed with the geometry of a 2D plate containing rigid inclusions (see Figure IV.26a) submitted to uni-axial traction. The results are very similar to the ones displayed on Figure IV.29, and especially the crack in the deformed configuration that exhibits the same sharp cone shape.

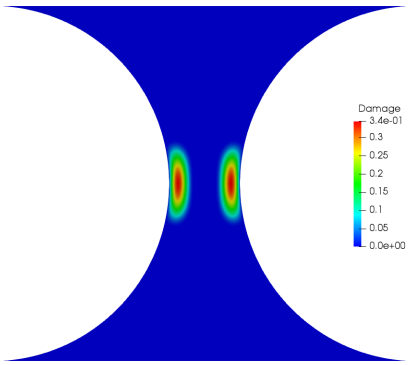

(a) Reference configuration – $\lambda_g = 2.3$.

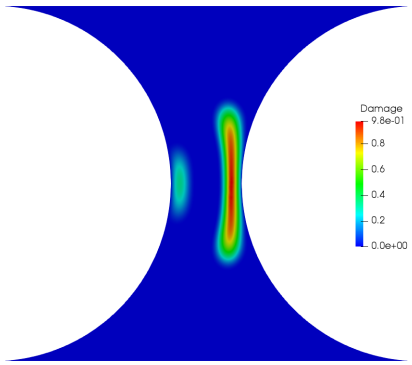

(b) Reference configuration – $\lambda_g = 2.4$.

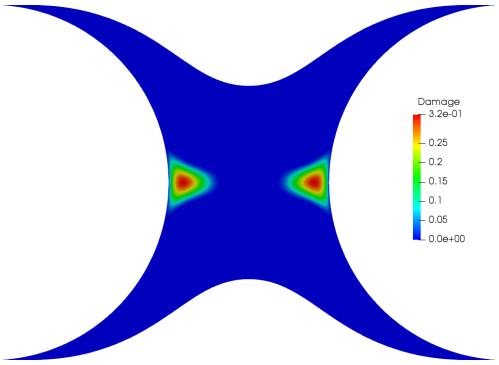

(c) Deformed configuration – $\lambda_g = 2.3$.

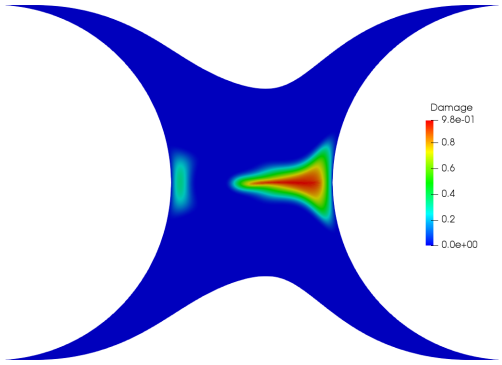

(d) Deformed configuration – $\lambda_g = 2.4$.

Figure IV.29: Rupture of a U-shaped specimen in large deformation under traction. Damage in the initial and actual configurations, for two successive time steps.

IV.6 Conclusion

In this chapter, a new, simple model has been introduced to remedy to the absence of the hydrostatic pressure in the initiation of damage. This model relies on the calibration of a parameter, called κ_e, whose value determines which one of the deviatoric stress, or the hydrostatic pressure, contributes to the onset of damage. In this model, although they do not follow the same law, both the shear constant and the compressibility coefficient depend on the same damage variable, α. Yet, some research on the damage and rupture of polymers have shown that the cavitation damage and the damage due to the deviatoric part of stress are two distinct phenomena, and that one do not affect the other. Let us cite for an example Dorfmann, Füller and Ogden in [14] who conducted experimental studies on this topic, and noticed that "the shear modulus is likewise unchanged by cavitation".

An idea to continue this work could be to separate these two damage phenomena, and to introduce two different damage variables, as is seen in the field of composite materials, where different damage variables are introduced to model the matrix damage, the delamination and the fibres damage. In that case, a material subjected to a pure hydrostatic loading would only have its compressibility coefficient diminished by damage, while a material under uni-axial loading would suffer damage only in its shear coefficient.

CHAPTER V

CAVITATION PHENOMENON

Contents

In this chapter, we investigate a very famous damage process in elastomers: the cavitation phenomenon, that is an inherently non linear phenomenon that cannot be modelled with linear elasticity. After a recall of the works done is this area by the pioneers Gent and Lindley, and the followers, we analyse the hyperelastic bifurcation of a sphere made of a compressible isotropic Neo-Hookean material submitted to a radial displacement on its boundaries. The classical study of the second derivative of the total energy is done, to be able to obtain the expression of the critical load at which cavitation may occur. We then study the coupling of the damage and the cavitation phenomenon that are considered as two different processes, even if they might lead to the same results in some cases. A 2D numerical study completes this analytical investigation and enforces the results obtained.

V.1 Motivations and state of the art

Among the many numerical simulations that were performed in order to verify that the gradient damage models are relevant in large deformation, one was inspired from Henao and its study of void nucleation [25] [60]. Starting from his work, we tried to perform the same kind of tests, with slightly different damage functions, and by taking into account the irreversibility of the damage process during a quasi-static loading. Some simulations showed promising results, and brought out the void nucleation.

We begin this chapter by a recall of the main results that can be found in the literature, in chronological order.

1958: Gent and Lindley [20]

In their paper of 1958, Gent and Lindley conducted experiments on natural rubber to observe its internal rupture, and measure the pressure for which internal flaws appeared. They proposed a criterion for the onset of cavitation, by considering an "extremely small cavity, sufficiently small for the region around it to be treated as an infinitely thick spherical shell". They used an incompressible Neo-Hookean potential of the form $\psi = C(I_1 - 3)$, and gave the relation between the traction acting at infinity P_m and the elongation of the inner surface λ

$$P_m = C\left(5 - \frac{4}{\lambda} - \frac{1}{\lambda^4}\right). \tag{V.1}$$

This expression predicts a limiting value of P_m at which λ becomes infinite, thereby making the cavity become infinitely large. According to this criterion, the theoretical critical pressure acting at infinity is $P_{crit} = 5C = 5\mu/2$, and it is found to be in good agreement with their experiments.

1982: Ball [7]

Most of the theoretical developments on the cavitation phenomenon was provided by Ball in its paper [7]. He studied a class of bifurcation problems for the equations of non linear elasticity, both for the incompressible and compressible cases, and for radial boundary displacement or traction problems. Unlike Gent and Lindley that considered a infinite domain containing a cavity of finite size, Ball considered a *full* unit sphere in which a cavity develops. In order to carry out its analysis, Ball made several restrictive assumptions, notably on the hyperelastic potentials, that prevent them to be very representative of the hyperelastic behaviours observed in reality. In the case of incompressible Neo-Hookean potentials, the bifurcation analysis of Ball leads to the same critical value of Gent and Lindley, because, as noted by Ball, "an infinitesimal hole in a finite piece of material behaves like a finite hole in an infinite expanse of material".

1968-1992: Horgan and co.

For incompressible material, the constraint of no volume change gives radial deformations of the form

$$r^n = R^n + A^n \tag{V.2}$$

where $A \geq 0$ is a constant that has to be determined. If $A = 0$, the sphere (or disk) remains solid in the reference configuration, if $A > 0$, a cavity of radius A has formed in the center of the body, and it is assumed to be traction free.

Although the results of Ball for incompressibility are quite complete, they are less extended for compressibility. Indeed, in contrast to incompressible material, it is not possible, in general, to determine analytical solutions that describe cavitation for compressible material, because the non linear differential equation of equilibrium has to be solved.

For compressible material, however, explicit analytical solutions describing cavitation have been provided by Horgan and Abeyaratne in the case of Blatz-Ko material, see [29]. Besides, in [28], Horgan also gave an explicit solution for a so-called compressible *generalised Varga material* of the form

$$r^3(R) = k_1(R^3 - A^3) + A^3\lambda^3 \tag{V.3}$$

where λ is the applied elongation, and k_1 is a constant related to the critical elongation.

Horgan and Polignone also made a review on cavitation [30] in 1995, presenting the results in cases of compressibility or incompressibility, isotropy or anisotropy, for various hyperelastic potentials. For compressible materials, non radially symmetric solutions have been studied, as well as solutions in elastodynamics. For incompressible materials, they cite the works done with finite strain plasticity, elastodynamics, or rate dependence.

Lopez-Pamies and co.

The works presented above are all relatively old, and a new contribution was brought by Lopez-Pamies and co. in the years 2010. Among their many contributions (*e.g.* [43] or [51]), we will cite [42], where Lopez-Pamies studied the onset of cavitation for compressible, isotropic hyperelastic solids subjected to non symmetric loading conditions. He worked on a specimen containing a cylindrical inhomogeneity much smaller than the specimen, and restricted its attention to in-plane pure stretch loadings so that the problem is essentially a 2D one. He established a closed-form criterion for the onset of damage that is written with respect to the stored-energy function $\phi(\lambda_1, \lambda_2)$, with λ_1 and λ_2 the two principal elongations

$$\frac{\dfrac{\partial\phi}{\partial\lambda_1}(\lambda_1,\lambda_2) - \dfrac{\partial\phi}{\partial\lambda_2}(\lambda_1,\lambda_2)}{\lambda_1 - \lambda_2} = 0 \tag{V.4}$$

V.2 Hyperelastic bifurcation

In this section, the cavitation phenomenon is studied as a bifurcation problem. After establishing the equilibrium equation, and a trivial solution that satisfies it, the stability of the solution is studied. The choice of a compressible Neo-Hookean material results from the fact that it has been shown numerically (see [42]), that although incompressible Neo-Hookean material subjected to hydrostatic pressure do not exhibit cavitation (see [7]), compressible do. Moreover, the Neo-Hookean potential is the simplest hyperelastic potential that can pretend to model the hyperelastic behaviour of a material, but to our knowledge, no exact analytical solutions regarding the onset of cavitation have been found up to now.

V.2.1 Equilibrium equation

Let us consider a sphere of made of an isotropic *compressible* Neo-Hookean material whose hyperelastic potential is decomposed into an isochoric and a volumetric part

$$\psi = C(\bar{I}_1 - 3) + D(J-1)^2 \tag{V.5}$$

where $D = \kappa/2$, with κ the compressibility coefficient, $\bar{I}_1 = J^{-2/3} I_1$ is the first reduced invariant of the left Cauchy-Green tensor $\boldsymbol{B} = \boldsymbol{F}\cdot\boldsymbol{F}^T$. We note R the radius in the reference configuration, such that $R_i \leq R \leq R_e$ and r the radius in the deformed configuration. This sphere is submitted to an elongation λ on its boundary, such that there exists a function f such that

$$f(R) = r. \tag{V.6}$$

For spherical problems, the deformation tensor

$$\boldsymbol{F} = \begin{bmatrix} \dfrac{\partial f}{\partial R} & 0 & 0 \\ 0 & \dfrac{f}{R} & 0 \\ 0 & 0 & \dfrac{f}{R} \end{bmatrix}, \tag{V.7}$$

and the dilatation tensor is

$$\boldsymbol{B} = \begin{bmatrix} \left(\dfrac{\partial f}{\partial R}\right)^2 & 0 & 0 \\ 0 & \left(\dfrac{f}{R}\right)^2 & 0 \\ 0 & 0 & \left(\dfrac{f}{R}\right)^2 \end{bmatrix}, \tag{V.8}$$

that leads to the expressions of the invariants

$$J = \det(\boldsymbol{F}) = \frac{\partial f}{\partial R}\left(\frac{f}{R}\right)^2 \tag{V.9}$$

$$I_1 = \mathrm{tr}(\boldsymbol{B}) = \left(\frac{\partial f}{\partial R}\right)^2 + 2\left(\frac{f}{R}\right)^2 \tag{V.10}$$

$$I_3 = \det(\boldsymbol{B}) = \left(\frac{\partial f}{\partial R}\right)^2 \left(\frac{f}{R}\right)^4. \tag{V.11}$$

In the compressible case, the Cauchy stress $\boldsymbol{\sigma}$ is

$$J\boldsymbol{\sigma} = 2CJ^{-2/3}\left(\boldsymbol{B} - \frac{1}{3}I_1\boldsymbol{I}\right) + 2D\ J(J-1)\boldsymbol{I}. \tag{V.12}$$

The radial component of the equilibrium equation in spherical coordinates in the actual configuration is

$$\frac{\partial \sigma_{rr}}{\partial r} + 2\frac{\sigma_{rr} - \sigma_{\theta\theta}}{r} = 0, \tag{V.13}$$

with σ_{rr} the radial stress, and $\sigma_{\theta\theta}$ the hoop stress. By injecting into the equilibrium equation (V.13), we obtain a differential equation that governs the evolution of f

$$\begin{aligned} f''(R)\left[A\left(\frac{f(R)}{R}\right)^2 + \frac{8C}{3J^{5/3}}f'(R)\right] =& -2\frac{f(R)}{R^3}\left(f'(R)R - f(R)\right)\left(Af'(R) - \frac{4C}{3J^{5/3}}\right) \\ & - 2\frac{f'(R)}{f(R)}(\sigma_{rr} - \sigma_{\theta\theta}) \end{aligned} \tag{V.14}$$

with

$$A = -\frac{\sigma_{rr}}{J} - \frac{4C}{3J^{8/3}}\left(B_{11} - \frac{I_1}{3}\right) + \frac{2D}{J}(2J-1). \tag{V.15}$$

By injecting (V.12) into (V.14), we get

$$A = \frac{-6C}{J^{8/3}}\left(B_{11} - \frac{I_1}{3}\right) + 2D \tag{V.16}$$

and (V.12) gives

$$\sigma_{rr} - \sigma_{\theta\theta} = 2CJ^{-5/3}(B_{11} - B_{22}). \tag{V.17}$$

This equation can be solved numerically. The problem is a boundary problem with the following conditions

$$\begin{cases} f''(R) = g(f'(R), f(R), R) \\ f(R_e) = r_e \\ \sigma_{rr}(R_i) = 0. \end{cases} \tag{V.18}$$

The second equation of the above system stands for the imposed displacement, and thus r_e is known. The third equation of (V.18) requires the use of a shooting method in order to find the value of $r_i = f(R_i)$ such that the radial interior stress is null. In order to be able to numerically observe a bifurcation, a micro-hole is introduced into the sphere, whose internal radius R_i is of the order of one percent of the external radius R_e.

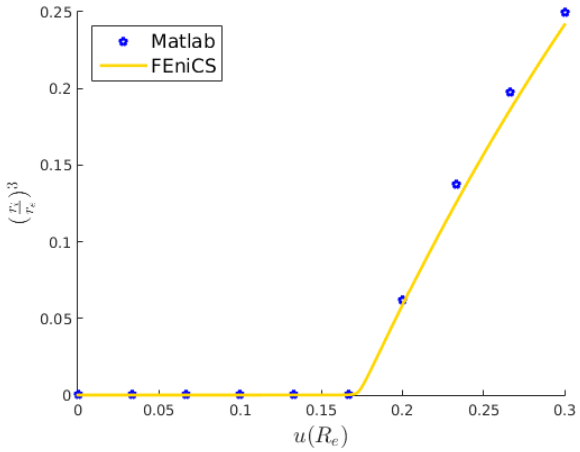

Figure V.1: Axi-symmetric equilibrium solution of a Neo-Hookean sphere with a micro-hole submitted to a radial displacement on its boundary. Volume fraction of cavity with respect to the imposed displacement. Both the finite element library FEniCS and the MATLAB function bvp4c are able to render the bifurcation of the solution.

The MATLAB bvp4c function for boundary value problems is used to solve this equation, and the solution is shown on Figure V.1 by blue dots: we plot the volume fraction of cavity defined by

$$v_f = \left(\frac{r_i}{r_e}\right)^3 \tag{V.19}$$

with respect to the imposed displacement on the external radius $u(R_e)$. We can see clearly that the curve can be decomposed into two phases: during the first one, the volume fraction of cavity stays close to zero, which means that the micro-hole introduced in the middle of the sphere does not grow. This regime corresponds to the one of small deformation. But after a given load is exceeded, the volume fraction of cavity increases significantly, and the micro-hole cannot be considered of negligible size any more.

This solution obtained with MATLAB is also compared to the one obtained with finite element in the FEniCS library, for an axi-symmetric problem (yellow line on Figure V.1). We can see that also in this case, the bifurcation of the solution appears clearly. In addition, the results of MATLAB and FEniCS are very close, and the results are therefore validated.

On Figure V.2, results for two different initial internal radii R_i are plotted. They are obtained with FEniCS, and show that the smallest the micro-hole in the sphere is, the more we tend towards a purely bifurcated solution. Figure V.2b, that displays the radial stress in R_e $\sigma_{rr}(R_e)$, shows that cavitation has an influence on the value of the radial stress: the stress grows until it reaches a critical value, and then decreases as the micro-hole develops.

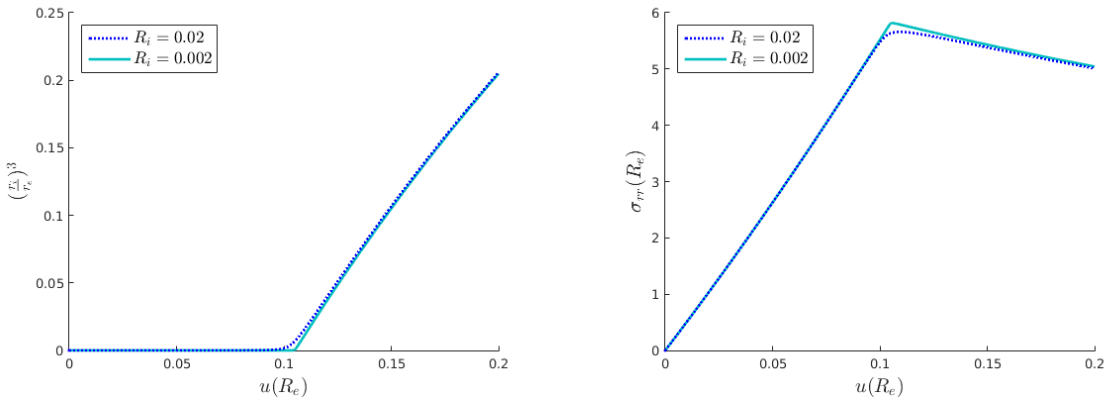

(a) Volume fraction of hole with respect to the displacement in R_e.

(b) Radial stress on the hole with respect to the displacement in R_e.

Figure V.2: Bifurcation of the solution for a sphere submitted to a radial elongation, for two different values of internal radius $R_i = 2\%R_e$ or $R_i = 0.2\%R_e$. The smallest the hole, the more pronounced is the bifurcation.

V.2.2 Stability of the equilibrium equation

Figure V.1 has shown that numerical calculations are able to render the cavitation phenomenon, and we now want to determine analytically the expression of the bifurcation, using the standard approach of the loss of ellipticity of the solution. We work in dimension N that can be either 2 or 3. The Neo-Hookean hyperelastic potential is therefore

$$\psi = C(J^{-2/N} I_1 - N) + D(J-1)^2. \tag{V.20}$$

V.2.2.a Second derivative of the total energy

To be able to calculate the second derivative of the energy functional, we need the following directional derivatives, at a point u in an admissible direction v

$$\boldsymbol{F}'(u)(v) = \boldsymbol{\nabla} \boldsymbol{v}, \tag{V.21}$$

$$J'(u)(v) = J \ \mathrm{tr}(\boldsymbol{F}^{-1} \cdot \boldsymbol{\nabla} \boldsymbol{v}), \tag{V.22}$$

$$I_1'(u)(v) = 2\mathrm{tr}(\boldsymbol{F}^T \cdot \boldsymbol{\nabla} \boldsymbol{v}), \tag{V.23}$$

$$\bar{I_1}'(u)(v) = -\frac{2}{N} \bar{I_1} \mathrm{tr}(\boldsymbol{F}^{-1} \cdot \boldsymbol{\nabla} \boldsymbol{v}) + 2J^{-2/N} \mathrm{tr}(\boldsymbol{F}^T \cdot \boldsymbol{\nabla} \boldsymbol{v}), \tag{V.24}$$

and

$$(\boldsymbol{F}^{-1})'(u)(v) = -\boldsymbol{F}^{-1} \cdot \boldsymbol{\nabla} \boldsymbol{v} \cdot \boldsymbol{F}^{-1}. \tag{V.25}$$

Without any external forces, the potential energy of the structure is the integral over the reference domain of the hyperelastic potential (V.20)

$$\mathscr{E}(u) = \int_{\Omega_0} \left(C(\bar{I_1} - N) + D(J-1)^2 \right) \mathrm{d}X. \tag{V.26}$$

with $\bar{I}_1 = J^{-2/N} I_1$. Its derivative at point u in the direction v is

$$\mathscr{E}'(u)(v) = \int_{\Omega_0} \left\{ 2C \left[-\frac{1}{N} \bar{I}_1 \mathrm{tr}(\boldsymbol{F}^{-1}\cdot\boldsymbol{\nabla v}) + J^{-2/N} \mathrm{tr}(\boldsymbol{F}^{T}\cdot\boldsymbol{\nabla v}) \right] + 2D(J^2 - J)\mathrm{tr}(\boldsymbol{F}^{-1}\cdot\boldsymbol{\nabla v}) \right\} \mathrm{d}X, \tag{V.27}$$

rewritten, by using $\mathrm{tr}(\boldsymbol{A}\cdot\boldsymbol{B}) = \boldsymbol{A}:\boldsymbol{B}$ for two second order tensors $\boldsymbol{A}$ and $\boldsymbol{B}$ where : is the double contracted product

$$\mathscr{E}'(u)(v) = \int_{\Omega_0} \left\{ 2C \left(J^{-2/N} \boldsymbol{F}\cdot\boldsymbol{F}^{T} - \frac{1}{N} \bar{I}_1 \boldsymbol{I} \right) + 2D(J^2 - J)\boldsymbol{I} \right\} \cdot \boldsymbol{F}^{-T} : \boldsymbol{\nabla v} \, \mathrm{d}X. \tag{V.28}$$

The expression in the brackets of (V.28) is the expression of the Kirchhoff stress tensor $\boldsymbol{\tau} = J\boldsymbol{\sigma}$ with $\boldsymbol{\sigma}$ the Cauchy stress for a Neo-Hookean material given in (V.12). Applying the divergence formula, and using the relation $\boldsymbol{\Pi} = J\boldsymbol{\sigma}\boldsymbol{F}^{-T}$, we find the equilibrium equation in the reference configuration

$$\mathrm{Div}\ \Pi = 0 \quad \text{on } \Omega_0. \tag{V.29}$$

The second derivative of (V.26) gives

$$\begin{aligned} \mathscr{E}''(u)(v)(v) = \int_{\Omega_0} & \left(\frac{4}{N^2} C\ \bar{I}_1 + 2D(2J^2 - J) \right) \left(\mathrm{tr}(\boldsymbol{F}^{-1}\cdot\boldsymbol{\nabla v}) \right)^2 \\ & - \frac{8}{N} C\ J^{-2/N} \mathrm{tr}(\boldsymbol{F}^{-1}\cdot\boldsymbol{\nabla v})\ \mathrm{tr}(\boldsymbol{F}^{T}\cdot\boldsymbol{\nabla v}) \\ & \left(\frac{2}{N} C\ \bar{I}_1 - 2D(J^2 - J) \right) \mathrm{tr}(\boldsymbol{F}^{-1}\cdot\boldsymbol{\nabla v}\cdot\boldsymbol{F}^{-1}\cdot\boldsymbol{\nabla v}) \\ & 2C\ J^{-2/N} \mathrm{tr}(\boldsymbol{\nabla v}\cdot\boldsymbol{\nabla v}^{T}). \end{aligned} \tag{V.30}$$

V.2.2.b Stability of the solution f_0 for $R_i = 0$

In the case of a full domain ($R_i = 0$), a solution of the equilibrium problem is

$$f_0(R) = r = \lambda R, \quad R \in (0, R_e) \tag{V.31}$$

where $\lambda = f(R_e)/R_e$ is the imposed elongation. This is known as the trivial solution for a pure dilatation problem. Starting from that solution, we seek the elongation λ such that the second derivative of the energy $\mathscr{E}$ is not positive any more, for any admissible radial field v. This gives the elongation for which the trivial solution is not stable any more. The gradient of a given kinematically admissible v field is

$$\boldsymbol{\nabla v} = \left[\mathrm{diag} \left(\frac{\partial v}{\partial R}, \frac{v}{R}, \ldots \right) \right] \tag{V.32}$$

where diag stands for a diagonal matrix. We have therefore, for axi-symmetric coordinates

$$\left(\mathrm{tr}(\boldsymbol{F}^{-1}\cdot\boldsymbol{\nabla v}) \right)^2 = \left(\frac{v'}{f'} + (N-1)\frac{v}{f} \right)^2, \tag{V.33}$$

$$\mathrm{tr}(\boldsymbol{F}^{-1}\cdot\boldsymbol{\nabla v})\ \mathrm{tr}(\boldsymbol{F}^{T}\cdot\boldsymbol{\nabla v}) = \left(\frac{v'}{f'} + (N-1)\frac{v}{f}\right)\left(f'v' + (N-1)\frac{f}{R}\frac{v}{R}\right), \tag{V.34}$$

$$\mathrm{tr}(\boldsymbol{F}^{-1}\cdot\boldsymbol{\nabla v}\cdot\boldsymbol{F}^{-1}\cdot\boldsymbol{\nabla v}) = \left(\frac{v'}{f'}\right)^2 + (N-1)\left(\frac{v}{f}\right)^2, \tag{V.35}$$

and

$$\mathrm{tr}(\boldsymbol{\nabla v}\cdot\boldsymbol{\nabla v}^{T}) = (v')^2 + (N-1)\left(\frac{v}{R}\right)^2. \tag{V.36}$$

With the trivial solution (V.31), the invariants are written with respect to the elongation λ

$$J = \lambda^N, \tag{V.37}$$

$$I_1 = N\ \lambda^2, \tag{V.38}$$

$$\bar{I}_1 = N. \tag{V.39}$$

We note

$$\begin{cases} a = \dfrac{4}{N^2}C\ \bar{I}_1 + 2D(2J^2 - J) \\ b = -\dfrac{8}{N}C\ J^{-2/N} \\ c = \dfrac{2}{N}C\ \bar{I}_1 - 2D(J^2 - J) \\ d = 2C\ J^{-2/N}. \end{cases} \tag{V.40}$$

so that the second derivative of the energy is written

$$\begin{aligned} \mathscr{E}''(u)(v)(v) = \int_{\Omega_0} & a\left(\mathrm{tr}(\boldsymbol{F}^{-1}\cdot\boldsymbol{\nabla v})\right)^2 + b\ \mathrm{tr}(\boldsymbol{F}^{-1}\cdot\boldsymbol{\nabla v})\ \mathrm{tr}(\boldsymbol{F}^{T}\cdot\boldsymbol{\nabla v}) \\ & + c\ \mathrm{tr}(\boldsymbol{F}^{-1}\cdot\boldsymbol{\nabla v}\cdot\boldsymbol{F}^{-1}\cdot\boldsymbol{\nabla v}) + d\ \mathrm{tr}(\boldsymbol{\nabla v}\cdot\boldsymbol{\nabla v}^{T}). \end{aligned} \tag{V.41}$$

a, b, c and d are functions of λ, after injecting (V.31)

$$\begin{cases} a = \dfrac{4}{N}C + 2D\lambda^N(2\lambda^N - 1) \\ b = -\dfrac{8}{N}\dfrac{C}{\lambda^2} \\ c = 2C - 2D\lambda^N(\lambda^N - 1) \\ d = \dfrac{2C}{\lambda^2}. \end{cases} \tag{V.42}$$

The second derivative of the potential energy is now the integral over one dimension of

$$\begin{aligned}\mathscr{E}''_\lambda(u_0)(v)(v) = 2\pi(N-1)\int_0^{R_e} & aR^{N-1}\left(\frac{(v')^2}{(f_0')^2} + (N-1)^2\frac{v^2}{f_0^2} + 2(N-1)\frac{vv'}{f_0 f_0'}\right) \\ & + bR^{N-1}\left((v')^2 + (N-1)^2\frac{v^2}{R^2} + 2vv'\left(\frac{f_0}{f_0'R^2} + \frac{f_0'}{f_0}\right)\right) \\ & + cR^{N-1}\left(\left(\frac{v'}{f_0'}\right)^2 + (N-1)\left(\frac{v}{f_0}\right)^2\right) \\ & + dR^{N-1}\left((v')^2 + (N-1)\frac{v^2}{R^2}\right).\end{aligned} \tag{V.43}$$

with $u_0 = f_0(R) - R$. It can be written

$$\mathscr{E}''_\lambda(u_0)(v)(v) = 2\pi(N-1)\int_{R_i}^{R_e}\left(R^{N-3}v^2Q_{11} + v'^2R^{N-1}Q_{22} + 2vv'R^{N-2}Q_{12}\right)\mathrm{d}R \tag{V.44}$$

where

$$\begin{cases} Q_{11} = (N-1)^2 a\dfrac{R^2}{f_0^2} + (N-1)^2 b + (N-1)c\dfrac{R^2}{f_0^2} + (N-1)d \\ Q_{22} = \dfrac{a}{(f_0')^2} + b + \dfrac{c}{(f_0')^2} + d \\ Q_{12} = (N-1)a\dfrac{R}{f_0 f_0'} + bR\left(\dfrac{f_0}{f_0'R^2} + \dfrac{f_0'}{f_0}\right) \end{cases} \tag{V.45}$$

that simplifies when injecting (V.31)

$$\begin{cases} Q_{11} = \dfrac{(N-1)^2 a}{\lambda^2} + (N-1)^2 b + \dfrac{(N-1)c}{\lambda^2} + (N-1)d \\ Q_{22} = \dfrac{a}{\lambda^2} + b + \dfrac{c}{\lambda^2} + d \\ Q_{12} = \dfrac{(N-1)a}{\lambda^2} + 2b. \end{cases} \tag{V.46}$$

Under matricial form, (V.44) is

$$\mathscr{E}''_\lambda(u_0)(v)(v) = 2\pi(N-1)\int_{R_i}^{R_e}\left[\begin{pmatrix} R^{(N-3)/2}\,v \\ R^{(N-1)/2}\,v' \end{pmatrix}^T \begin{pmatrix} Q_{11} & Q_{12} \\ Q_{21} & Q_{22} \end{pmatrix}\begin{pmatrix} R^{(N-3)/2}\,v \\ R^{(N-1)/2}\,v' \end{pmatrix}\right]\mathrm{d}R, \tag{V.47}$$

in which

$$\mathscr{Q}_\lambda = \begin{pmatrix} Q_{11} & Q_{12} \\ Q_{21} & Q_{22} \end{pmatrix} \tag{V.48}$$

contains only terms that depend on λ. The determinant of $\mathscr{Q}_\lambda$ shows that there exists a λ_c such that

$$\det(\mathscr{Q}_{\lambda_c}) = 0 \tag{V.49}$$

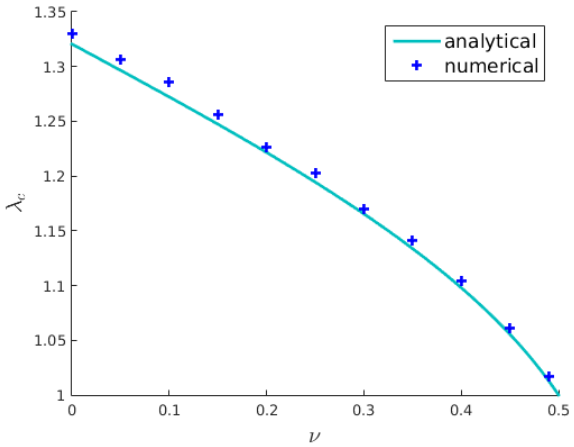

Figure V.3: Comparison of the values of the critical elongation for which cavitation occurs when calculated from an instability criterion with a full sphere (analytical solution (V.50)) and calculated via the numerical simulation of a sphere with a micro-hole submitted to traction.

and the matrix $\mathscr{Q}_\mu$ is not positive definite for $\mu > \lambda_c$. The solution of (V.49) is

$$\lambda_c = \frac{\sqrt[N]{\sqrt{\frac{8C+D}{D}} + 1}}{\sqrt[N]{2}}. \tag{V.50}$$

Thus, for an elongation $\lambda > \lambda_c$, the trivial solution of dilation becomes unstable for a compressible Neo-Hookean material. We have determined an exact analytical solution of the critical load for which cavitation occurs in compressible Neo-Hookean materials. Remarkably, this solution happens to be quite simple, much more than what could have been augured.

The analytical expression of the critical load for cavitation in the case of a full sphere is compared with the numerical results obtained with FEniCS for a sphere with a micro-hole, and the results are displayed on Figure V.3. They match quite well, and prove that if the micro-hole is small enough, the solution tends to the solution of a full sphere that undergoes cavitation. In addition, it illustrates well the formula (V.50) that shows that if D becomes large in front of C, that is if the material becomes incompressible, λ_c tends to the value 1: for a full, incompressible sphere, if a displacement is imposed, the solution is instantaneously unstable.

V.3 Damage and cavitation

After studying the hyperelastic phenomenon of cavitation, we now want to see what changes can be brought by the addition of damage in the behaviour of the material.

V.3.1 Comparison of critical loads

We have established the expression of the critical load for cavitation, and want to compare with the critical load for damage. The material constants are now functions of the damage, and the hyperelastic potential is

$$\psi = C_0(1-\alpha)^2(J^{-2/N}I_1 - N) + D_0(1-\alpha)^2(J-1)^2. \tag{V.51}$$

with C_0 and D_0 the initial shear modulus and compressibility coefficient respectively.

In the case of a full domain, we write the total energy as a functional that depends on the damage α and the displacement u

$$\mathscr{E}(u,\alpha) = \int_{\Omega_0} \left(\psi(u,\alpha) + w(\alpha) + \frac{1}{2}w_1\ell^2\nabla\alpha\cdot\nabla\alpha\right) \mathrm{d}X. \tag{V.52}$$

In spherical coordinates, it becomes

$$\mathscr{E}(R,\alpha) = 2\pi(N-1)\int_0^{R_e} \left[\psi(u,\alpha) + w(\alpha) + \frac{1}{2}w_1\ell^2(\alpha')^2\right] R^{N-1}\mathrm{d}R. \tag{V.53}$$

The Gâteaux derivative at point α in the direction β gives

$$\mathscr{E}'(R,\alpha)(R,\beta) = 2\pi(N-1)\int_0^{R_e} \left[\frac{\partial\psi(u,\alpha)}{\partial\alpha}\beta + w'(\alpha)\beta + w_1\ell^2\alpha'\beta'\right] R^{N-1}\mathrm{d}R. \tag{V.54}$$

After integrating by part, the derivative becomes

$$\mathscr{E}'(R,\alpha)(R,\beta) = 2\pi(N-1)\int_0^{R_e} \left[\frac{\partial\psi(u,\alpha)}{\partial\alpha} + w'(\alpha) - w_1\ell^2\alpha''\right] \beta R^{N-1}\mathrm{d}R. \tag{V.55}$$

Using the first order stability condition gives the damage criterion

$$\left.\frac{\partial\psi(u,\alpha)}{\partial\alpha}\right|_{\alpha=0} + w'(0) = 0. \tag{V.56}$$

In spherical coordinates, with the potential (V.20), $\bar{I}_1 = N$ so the isochoric part of the potential is null, and the damage criterion is a function of the compressibility coefficient D_0 and the w_1 only

$$-2D_0(\lambda^N - 1)^2 + w_1 = 0, \tag{V.57}$$

that gives

$$\lambda_e = \left[1 + \left(\frac{w_1}{2D_0}\right)^{1/2}\right]^{1/N}. \tag{V.58}$$

To recapitulate, the critical elongation for cavitation is a function of the ratio of the material parameters C_0/D_0, while the critical elongation for damage is a function of the ratio of the compressibility coefficient D_0 and the constant of first damage w_1. Thus, for a given

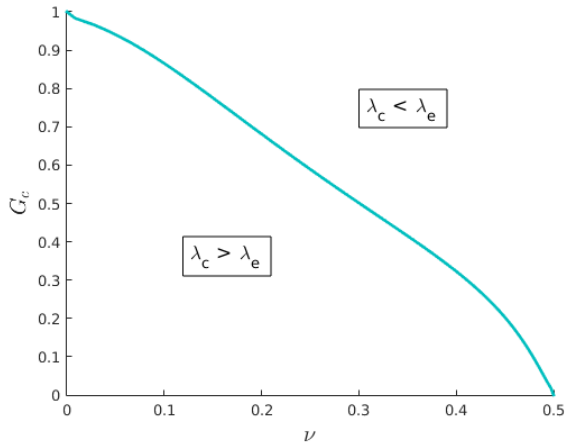

Figure V.4: Comparison of the critical loads of the damage λ_e and the cavitation λ_c. For a fixed value of ν, λ_c/λ_e depends on the value of G_c.

value of the Poisson coefficient, depending on the value of w_1, the critical elongation for cavitation λ_c can be smaller or greater than the critical elongation for damage λ_e. This is illustrated by Figure V.4 that shows two domains, depending on the values of $G_c = w_1\ell/c_w$ (with ℓ the internal length and c_w a constant) and ν. For small values of ν, that is to say, for materials that are very compressible, they are likely to initiate damage before cavitation: on Figure, for an example, for $\nu = 0.1$ and $G_c = 0.7$, $\lambda_c > \lambda_e$. Conversely, for materials with a high Poisson ratio, *i.e.* quasi-incompressible materials, they are likely to cavitate before they initiate damage.

V.3.2 2D numerical tests

Results have shown that the rupture pattern of a disk is not axi-symmetric. Therefore it would make no sense to do a one dimensional study of the competition between the damage and the cavitation phenomenon. Numerical tests were consequently performed with MEF++ in 3D, with plain strain conditions. These conditions lead to different results than those obtained in the previous section, where we worked with spheres (3D) or disks (2D), thereby making the comparison between analytical and numerical results difficult.

A compressible full disk made of a Mooney-Rivlin material was submitted to traction on its boundary. No micro-hole was introduced, because the aim was precisely to observe how the rupture is affected by the cavitation, without introducing artificial defects. Boundary conditions of no damage were imposed. Different sets of parameters were used, to study the influence of the internal length, the value of w_1, or the value of κ_0.

The results displayed were obtained using the parameter given in Table V.1. The internal length was chosen small enough with respect to the radius of the disk $\ell/R = 0.05$ so that the localisation of the damage would be ensured. Two different values of G_c are used: if G_c is small, damage initiates sooner that if G_c is large. The idea was to play over the ratio of the

R	C_{10}	C_{01}	κ	ℓ	G_c	k_{ell}	tol	h
1.0	10	5	0.1	0.05	1 or 50	1e-6	1e-4	0.3 ℓ

Table V.1: Geometrical, material and numerical parameters for a 2D disk made of a Mooney-Rivlin material, submitted to traction.

critical elongations for damage and cavitation.

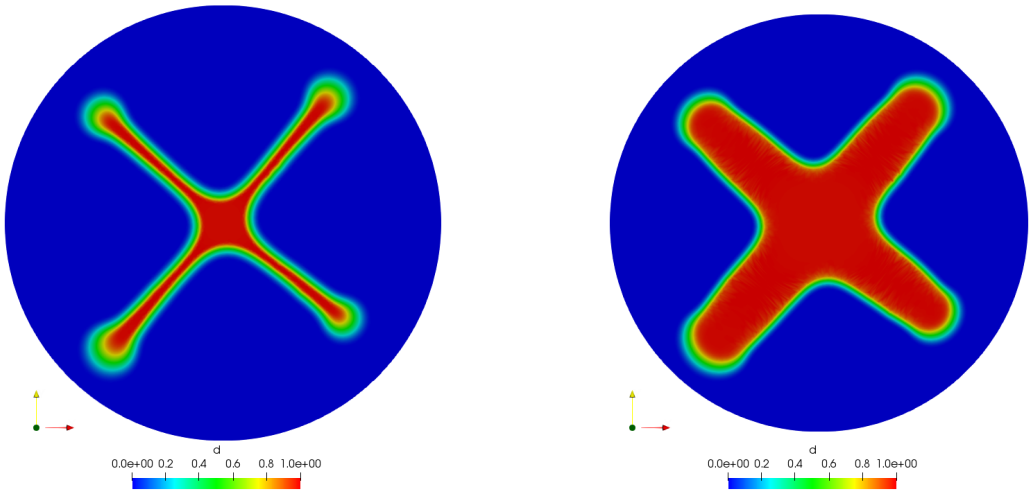

(a) Reference configuration. *(b) Deformed configuration.*

Figure V.5: Rupture pattern of a disk submitted to an elongation. Parameters of Table V.1 with $G_c = 1.0$. Reference and deformed configuration.

Figure V.5 shows the results for $G_c = 1.0$: the rupture pattern is displayed in the reference and deformed configurations. It is cross shaped, with a 90°angle between each one of its four branches. The rupture pattern V.5a is characteristic of the ones that are obtained in linear elasticity. There is yet a damper on these results: all the simulations carried out in small deformation for the same problem (under under radial displacement) have shown rupture patterns with branches that make a 120°angle. It has proven to be in keeping with the conjecture of Mumford and Shah. Yet, this 4-branches rupture pattern has been found in the simulations of [47], therefore it can be considered as typical of small deformation.

For a larger value of G_c, the rupture pattern V.6 is very different from what has been observed in this thesis. We have shown in the section II.2 that the rupture profile in the reference configuration is sharp, and is the same as in small deformation. Yet, here, we can see that the rupture profile is not sharp, since a large circular zone, that could be qualified as a hole, has a damage close to the value 1. This rupture pattern can be observed only in large deformation, and has to be triggered by the non linearities of the displacement problem. The

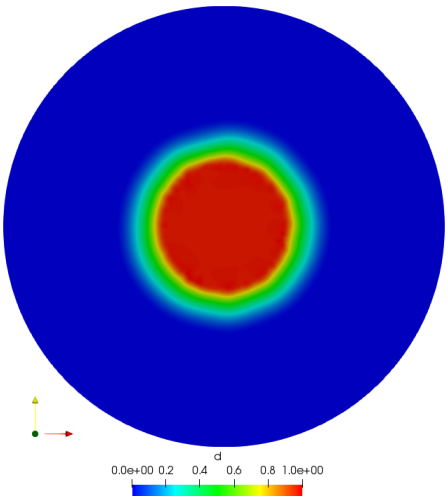

Figure V.6: Rupture pattern of a disk submitted to an elongation. Parameters of Table V.1 with $G_c = 50.0$. Reference configuration.

next time steps of the calculation are not shown here, but a crack eventually propagates from this hole, leading to the rupture of the disk.

By using two different values of G_c, we have shown that two different rupture pattern can appear. This corroborates well the results of the section V.3 where we have shown that for a fixed value of the compressibility coefficient, the critical elongation for damage can be higher (or smaller) than the critical elongation for damage, depending on the value of G_c. In other words, in the simulations, the value of G_c controls the moment when damage occurs: if the value is small enough, the rupture pattern is typical of small deformation, while if it is big enough, the rupture pattern is very different.

These results are very new, and to our knowledge, do not exist in the literature about gradient damage models in finite strain. It can be noticed that simulations carried out with the *compressible* Neo-Hookean and Mooney-Rivlin potentials have led to the same rupture patterns, *i.e.* hole-shaped cracks. Moreover, in these cases, the value of the residual energy k_{ell} has been chosen small enough to ensure its non influence over the results. One of the question that arise is: should these results considered as representative of the rupture behaviour of a hyperelastic solid under bi-axial loading? Or should the formulation of the damage problem be adapted to avoid such rupture patterns? For an example, it could be imagined that the dissipated energy for damage be different in large deformation, to take into account the stretching of the surfaces.

V.4 Conclusion

This chapter was an exploration of the cavitation phenomenon, and in particular, of its interaction with damage. Due to the complexity of the topic, many questions stay unanswered.

Although an analytical value for the critical elongation for cavitation, for a compressible Neo-Hookean material, has been found, the analytical expression of the bifurcated branch has not been established. The developments around the critical elongation that were tried did not lead to any usable expression.

Regarding the numerical simulations, some results could be enriched, using more realistic laws and parameters, provided that an adequate finite element method is used. In [60], Xu and Henao used a finite element method, based on non conforming Crouzeix-Raviart elements, that prevents the degeneration of the mesh when numerical computation of cavitation in non linear elasticity is performed. This could be one lead to follow in the future.

CONCLUSION

Gradient damage models have proven to be excellent at describing the initiation and propagation of cracks, in small deformation, for many situations (with temperature, plasticity, etc). By using both analytical and numerical approaches, this work has shown that they are also very relevant in large deformation, especially for the initiation of damage. In this conclusion, we recall the main results, and give some leads that could be followed to deepen the study.

Analytically, it has been established in Chapter II that in the reference configuration, the damage profile of a broken material is the same as for a linear elastic material, even if the snap-backs are different. Moreover, the one dimensional study of viscoelastic materials (in both small and large deformation), has revealed interesting properties, also visible in the numerical applications. Among them, there exists critical values of speed loading such that the localisation of the damage has necessarily to be following a homogeneous phase of damage. Yet, in order to deal with more realistic materials, more complicated models, such as the generalised Maxwell model, should be studied. Such studies means that it can only be done numerically, because the equations become far more complicated as the number of viscoelastic branches is increased. In a 3D finite deformation code, the influence of the viscosity over the initiation and propagation of cracks would certainly give interesting results.

Numerically, gradient damage models are very efficient to model the initiation of damage in sound (without the introduction of micro-defects), quasi-incompressible materials. By introducing a new dependency on damage of the compressibility coefficient of the type

$$\kappa(\alpha) = \frac{(1-\alpha)^2 \kappa_e}{\alpha}, \tag{V.59}$$

and using a dependency on damage law of $(1-\alpha)^2$ in front of the shear coefficient, it has been shown that the damage can initiate either in zones of large strain or of high pressure, depending on the value of the parameter κ_e. This parameter does not have a physical meaning, it is calibrated by comparing with experiments. The simulations have been confronted

to experimental results performed on specimen containing rigid inclusions, and have shown a very good agreement.

Numerical experiments performed on 2D disks have also shown that gradient damage models are able to reproduce the cavitation phenomenon, without needing to introduce any artificial micro-defects. Because of the complexity of the equations in non linear elasticity, analytical studies could not go very far. Nevertheless, we have been able to obtain the critical elongation at which cavitation of a sphere ($N = 3$) or a disk ($N = 2$) occurs, for an isotropic, compressible, Neo-Hookean material submitted to an elongation

$$\lambda_c = \frac{\sqrt[N]{\sqrt{\frac{8C+D}{D}} + 1}}{\sqrt[N]{2}}. \tag{V.60}$$

with C the shear modulus and D the compressibility coefficient. One lead to further the numerical study of the cavitation damage could be to use the function of κ (V.59) in the case of an incompressible disk. Some tests were performed in small deformation in that situation, that were not displayed in this thesis because they would have been redundant. In large deformation nonetheless, it would be interesting to see how it combines with the cavitation.

In a nutshell, gradient damage models are very good at modelling brittle fracture (Chapter III), or hydrostatic damage (Chapter IV), or cavitation (Chapter V), in large deformation.

BIBLIOGRAPHY

[1] Roberto Alessi, Jean-Jacques Marigo, and Stefano Vidoli. Gradient damage models coupled with plasticity and nucleation of cohesive cracks. *Archive for Rational Mechanics and Analysis*, 214(2):575–615, 2014. (Cited on page 15.)

[2] Roberto Alessi, Stefano Vidoli, and Laura De Lorenzis. A phenomenological approach to fatigue with a variational phase-field model: The one-dimensional case. 12 2017. (Cited on page 15.)

[3] Roberto Alicandro, Marco Cicalese, and Antoine Gloria. Mathematical derivation of a rubber-like stored energy functional. *Comptes Rendus Mathematique*, 345(8):479 – 482, 2007. (Cited on page 57.)

[4] Hanen Amor, Jean-Jacques Marigo, and Corrado Maurini. Regularized formulation of the variational brittle fracture with unilateral contact: Numerical experiments. *Journal of the Mechanics and Physics of Solids*, 57(8):1209 – 1229, 2009. (Cited on page 61.)

[5] Ellen M. Arruda and Mary C. Boyce. A three-dimensional constitutive model for the large stretch behavior of rubber elastic materials. *Journal of the Mechanics and Physics of Solids*, 41(2):389 – 412, 1993. (Cited on page 57.)

[6] John M. Ball. Convexity conditions and existence theorems in nonlinear elasticity. *Archive for Rational Mechanics and Analysis*, 63(4):337–403, 12 1976. (Cited on pages 39 and 58.)

[7] John M. Ball. Discontinuous equilibrium solutions and cavitation in nonlinear elasticity. *Philosophical Transactions of the Royal Society of London A: Mathematical, Physical and Engineering Sciences*, 306(1496):557–611, 1982. (Cited on pages 116 and 118.)

[8] Zdeněk P. Bazănt and Milan Jirásek. Nonlocal integral formulations of plasticity and damage: Survey of progress. *Journal of Engineering Mechanics*, 128(11):1119–1149, 2002. (Cited on page 2.)

[9] Blaise Bourdin, Gilles A. Francfort, and Jean-Jacques Marigo. Numerical experiments in revisited brittle fracture. *Journal of the Mechanics and Physics of Solids*, 48(4):797–826, 2000. (Cited on page 3.)

[10] Blaise Bourdin, Gilles A. Francfort, and Jean-Jacques Marigo. *The variational approach to fracture*, volume 91. Springer Verlag (Germany), 2008. (Cited on page 3.)

[11] Blaise Bourdin, Jean-Jacques Marigo, Corrado Maurini, and Paul Sicsic. Morphogenesis and propagation of complex cracks induced by thermal shocks. *Physical Review Letters*, 112:014301, Jan 2014. (Cited on page 15.)

[12] Patrick Ciarlet and Giuseppe Geymonat. Sur les lois de comportement en élasticité non linéaire compressible. *CR Acad. Sci. Paris Sér. II*, 295:423–426, 1982. (Cited on page 39.)

[13] G. Del Piero, G. Lancioni, and R. March. A variational model for fracture mechanics: Numerical experiments. *Journal of Mechanics Physics of Solids*, 55:2513–2537, December 2007. (Cited on page 56.)

[14] A. Dorfmann, K.N.G. Fuller, and R. W. Ogden. Shear, compressive and dilatational response of rubberlike solids subject to cavitation damage. *International Journal of Solids and Structures*, 39(7):1845–1861, April 2002. (Cited on page 114.)

[15] Wilhelm Flügge. *Viscoelasticity*. Number 67-10742. Blaisdell Publishing Company, 1967. (Cited on page 26.)

[16] André Fortin and Michel Fortin. Projet mef++. (Cited on pages 16, 56, and 111.)

[17] André Fortin and André Garon. *Les éléments finis : de la théorie à la pratique*. 2018. (Cited on page 58.)

[18] Gilles A. Francfort and Jean-Jacques Marigo. Revisiting brittle fracture as an energy minimization problem. *Journal of the Mechanics and Physics of Solids*, 46(8):1319 – 1342, 1998. (Cited on pages 3, 5, 6, 7, and 8.)

[19] Gilles A. Francfort and Jean-Jacques Marigo. Etude d'une classe de modèles d'endommagement à gradient. Technical report, 1999. (Cited on page 3.)

[20] Alan N. Gent and P. B. Lindley. Internal rupture of bonded rubber cylinders in tension. *Proceedings of the Royal Society of London A: Mathematical, Physical and Engineering Sciences*, 249(1257):195–205, 1959. (Cited on page 116.)

[21] Alan N. Gent and Byoungkyeu Park. Failure processes in elastomers at or near a rigid spherical inclusion. *Journal of Materials Science*, 19(6):1947–1956, Jun 1984. (Cited on page 107.)

[22] Antoine Gloria, Patrick Le Tallec, and Marina Vidrascu. Foundation, analysis, and numerical investigation of a variational network-based model for rubber. *Continuum Mechanics and Thermodynamics*, 26(1):1–31, 2014. cited By 4. (Cited on page 57.)

[23] Gert Heinrich and Michael Kaliske. Theoretical and numerical formulation of a molecular based constitutive tube-model of rubber elasticity. *Computational and Theoretical Polymer Science*, 7(3):227 – 241, 1997. (Cited on page 57.)

[24] Duvan Henao, Carlos Mora-Corral, and Xianmin Xu. γ-convergence approximation of fracture and cavitation in nonlinear elasticity. *Archive for Rational Mechanics and Analysis*, 216(3):813–879, 2015. (Cited on page 56.)

[25] Duvan Henao, Carlos Mora-Corral, and Xianmin Xu. A numerical study of void coalescence and fracture in nonlinear elasticity. *Computer Methods in Applied Mechanics and Engineering*, 303, 01 2016. (Cited on pages 61 and 116.)

[26] C. Hesch and K. Weinberg. Thermodynamically consistent algorithms for a finite-deformation phase-field approach to fracture. *International Journal for Numerical Methods in Engineering*, 99(12):906–924, 2014. (Cited on page 56.)

[27] Cristian Hesch, A.J. Gil, R. Ortigosa, M. Dittmann, C. Bilgen, P. Betsch, M. Franke, A. Janz, and K. Weinberg. A framework for polyconvex large strain phase-field methods to fracture. *Computer Methods in Applied Mechanics and Engineering*, 317:649 – 683, 2017. (Cited on page 56.)

[28] Cornelius O. Horgan. Void nucleation and growth for compressible non-linearly elastic materials: An example. *International Journal of Solids and Structures*, 29(3):279 – 291, 1992. (Cited on page 117.)

[29] Cornelius. O. Horgan and R. Abeyaratne. A bifurcation problem for a compressible nonlinearly elastic medium: growth of a micro-void. *Journal of Elasticity*, 16(2):189–200, Jun 1986. (Cited on page 117.)

[30] Cornelius O. Horgan and Debra A. Polignone. Cavitation in nonlinearly elastic solids: A review. *Applied Mechanics Reviews*, 48, 08 1995. (Cited on page 117.)

[31] Lazar M. Kachanov. Rupture time under creep conditions. *Izvestiya Akademii Nauk SSSR*, 8:26–31, 1958. (Cited on page 2.)

[32] Michael Kaliske, Lutz Nasdala, and Heinrich Rothert. On damage modelling for elastic and viscoelastic materials at large strain. *Computers & Structures*, 79(22):2133 – 2141, 2001. (Cited on page 61.)

[33] Aditya Kumar, Gilles A. Francfort, and Oscar Lopez-Pamies. Fracture and healing of elastomers: A phase-transition theory and numerical implementation. *Journal of the Mechanics and Physics of Solids*, 112:523 – 551, 2018. (Cited on pages 56, 78, and 108.)

[34] Patrick Le Tallec. *Modélisation et Calcul des Milieux Continus*. Les Editions de l'Ecole Polytechnique, 2009. (Cited on page 59.)

[35] Victor Lefèvre, K. Ravi-Chandar, and Oscar Lopez-Pamies. Cavitation in rubber: an elastic instability or a fracture phenomenon? *International Journal of Fracture*, 192(1):1–23, Mar 2015. (Cited on page 77.)

[36] Sophie Léger, Jean Deteix, and André Fortin. A Moore-Penrose continuation method based on a Schur complement approach for nonlinear finite element bifurcation problems. *Computers and Structures*, 152:173 – 184, 2015. (Cited on page 76.)

[37] Jean Lemaitre. *A Course on Damage Mechanics*. Springer-Verlag Berlin Heidelberg, 1992. (Cited on page 2.)

[38] Jean Lemaître, Jean-Louis Chaboche, Ahmed Benallal, and Rodrigues Desmorat. *Mécanique des matériaux solides*. Dunod, 3ème edition, 2009. (Cited on pages 26 and 57.)

[39] Jean Lemaitre and Rodrigue Desmorat. *Engineering Damage Mechanics*. Springer-Verlag Berlin Heidelberg, 2005. (Cited on page 2.)

[40] Sophie Léger, André Fortin, Cristian Tibirna, and Michel Fortin. An updated lagrangian method with error estimation and adaptive remeshing for very large deformation elasticity problems. *International Journal for Numerical Methods in Engineering*, 100(13):1006–1030, 2014. (Cited on page 76.)

[41] Tianyi Li, Jean-Jacques Marigo, Daniel Guilbaud, and Seguei Potapov. Gradient damage modeling of brittle fracture in an explicit dynamics context. *International Journal for Numerical Methods in Engineering*, 108(11):1381–1405, 2016. (Cited on page 15.)

[42] Oscar Lopez-Pamies. Onset of cavitation in compressible, isotropic, hyperelastic solids. *Journal of Elasticity*, 94(2):115, Nov 2008. (Cited on pages 117 and 118.)

[43] Oscar Lopez-Pamies, Martin Idiart, and Toshio Nakamura. Cavitation in elastomeric solids: I—A defect-growth theory. *Journal of the Mechanics and Physics of Solids*, 59:1464–1487, 08 2011. (Cited on page 117.)

[44] Gilles Marckmann and Erwan Verron. Comparison of Hyperelastic Models for Rubber-Like Materials. *Rubber Chemistry and Technology*, 79(5):835–858, 2006. (Cited on page 56.)

[45] Jean-Jacques Marigo. L'endommagement et la Rupture : hier, aujourd'hui et demain. Lecture, March 2000. (Cited on page 3.)

[46] Jean-Jacques Marigo and Kim Pham. Construction and analysis of localized responses for gradient damage models in a 1d setting. *Vietnam Journal of Mechanics*, 31(3-4):233–246, 2009. (Cited on page 3.)

[47] Corrado Maurini, B Bourdin, Georges Gauthier, and Véronique Lazarus. Crack patterns obtained by unidirectional drying of a colloidal suspension in a capillary tube: Experiments and numerical simulations using a two-dimensional variational approach. *International Journal of Fracture*, 184, 11 2013. (Cited on pages 79 and 128.)

[48] Christian Miehe, Serdar Göktepe, and Frank Lulei. A micro-macro approach to rubber-like materials—Part I: the non-affine micro-sphere model of rubber elasticity. *Journal of the Mechanics and Physics of Solids*, 52(11):2617 – 2660, 2004. (Cited on page 57.)

[49] Christian Miehe, Martina Hofacker, and Fabian Welschinger. A phase field model for rate-independent crack propagation: Robust algorithmic implementation based on operator splits. *Computer Methods in Applied Mechanics and Engineering*, 199(45):2765 – 2778, 2010. (Cited on page 61.)

[50] Christian Miehe and Lisa-Marie Schänzel. Phase field modeling of fracture in rubbery polymers. Part I: Finite elasticity coupled with brittle failure. *Journal of the Mechanics and Physics of Solids*, 65:93 – 113, 2014. (Cited on page 56.)

[51] Toshio Nakamura and Oscar Lopez-Pamies. A finite element approach to study cavitation instabilities in nonlinear elastic solids under general loading conditions. *International Journal of Non-Linear Mechanics*, 47:331–340, 03 2012. (Cited on page 117.)

[52] Kim Pham. *Construction and analysis of gradient damage models*. PhD thesis, Université Pierre et Marie Curie - Paris VI, 2010. (Cited on pages 5 and 8.)

[53] Kim Pham and Jean-Jacques Marigo. Approche variationnelle de l'endommagement : I. Les concepts fondamentaux. *C. R. Mecanique*, 2010. (Cited on pages 3, 6, and 8.)

[54] Kim Pham and Jean-Jacques Marigo. Approche variationnelle de l'endommagement : II. Les modèles à gradient. *Comptes Rendus Mécanique*, 338(4):199 – 206, 2010. (Cited on page 3.)

[55] Kim Pham and Jean-Jacques Marigo. From the onset of damage to rupture: construction of responses with damage localization for a general class of gradient damage models. *Continuum Mechanics and Thermodynamics*, 25(2-4):147–171, 2013. (Cited on page 3.)

[56] Xavier Poulain, Victor Lefèvre, Oscar Lopez-Pamies, and Krishnaswamy Ravi-Chandar. Damage in elastomers: nucleation and growth of cavities, micro-cracks, and macro-cracks. *International Journal of Fracture*, 205(1):1–21, May 2017. (Cited on pages 107, 108, 109, and 111.)

[57] François Sidoroff. Un modèle viscoélastique non linéaire avec configuration intermédiaire. *Journal de Mécanique*, 13:679–713, 12 1974. (Cited on page 44.)

[58] Erwan Tanne. *Variational phase-field models from brittle to ductile fracture: nucleation and propagation*. PhD thesis, Université Paris-Saclay, 2017. (Cited on page 15.)

[59] Sonu S. Varguese, Steven H. Frankel, and Paul F. Fischer. Direct numerical simulation of stenotic flows. part 1. steady flow. *Journal of Fluid Mechanics*, 582:253–280, 2007. (Cited on page 71.)

[60] Xianmin Xu and Duvan Henao. An efficient numerical method for cavitation in nonlinear elasticity. *Mathematical Models and Methods in Applied Sciences*, 21(08):1733–1760, 2011. (Cited on pages 116 and 130.)

Titre : Modèles d'endommagement à gradient en grandes déformations

Mots clés : endommagement, rupture, cavitation, hyperélasticité, pression, viscoélasticité

Résumé : Les modèles d'endommagement à gradient, aussi dénommés modèles à champs de phases, sont désormais largement utilisés pour modéliser la rupture fragile et ductile, depuis l'initiation de l'endommagement jusqu'à la propagation d'une fissure. Cependant, la majorité des études disponibles dans la littérature ne concerne que le cadre des petites déformations, et très peu d'études poussées ont été menées afin d'étudier leur pertinence dans un contexte de grandes déformations. Ce serait pourtant d'un intérêt primordial, notamment pour l'industrie pneumatique, qui deviendrait alors capable de prédire plus précisément l'initiation de l'endommagement dans ses structures.
Dans la première partie de ce travail, nous établissons des solutions analytiques d'évolution de l'endommagement (homogène et localisée) pour des matériaux visqueux, en petites et en grandes déformations. En petites déformations, les modèles rhéologiques de Maxwell et Poynting-Thomson sont étudiés, et en grandes déformations, les modèles de Maxwell et Zener sont choisis. Une étude sur l'évolution de l'endommagement dans un cas purement hyperélastique est aussi menée.
A cette première partie analytique succède une partie numérique, qui détaille l'implémentation des modèles d'endommagement à gradient dans des codes éléments finis en grandes déformations. De même qu'en petites déformations, une stratégie de minimisation alternée est adoptée pour résoudre successivement les problèmes d'endommagement et de déplacement. Le matériau suit une loi de Mooney-Rivlin quasi-incompressible, et une méthode mixte en déplacement-pression est utilisée. Des tests en 2D et 3D sont effectués, qui mettent en évidence la capacité des modèles à initier de l'endommagement en grandes déformations.
Les modèles d'endommagement utilisés pour la seconde partie ne sont cependant capables d'initier de l'endommagement que dans les zones où la déformation est importante, c'est-à-dire dans les zones de forte contrainte déviatorique. Il a toutefois été montré que certains matériaux polymères, quasi-incompressibles, s'endommagent dans les zones de forte pression hydrostatique. Par conséquent, la recherche et l'étude d'un modèle d'endommagement capable d'initier de l'endommagement dans les zones de forte pression, pour des matériaux quasi-incompressibles lorsqu'ils sont sains, fait l'objet d'une troisième partie.
Enfin, la croissance brusque de cavités dans un matériau hyperélastique, appelée phénomène de cavitation, est étudiée, ainsi que son interaction avec l'endommagement. Dans un premier temps, nous considérons la cavitation comme une simple bifurcation hyperélastique d'un matériau néo-hookéen compressible isotrope, et déterminons l'expression analytique de l'élongation critique pour laquelle la cavitation fait son apparition. Dans un second temps, nous montrons qu'il y a une compétition entre la cavitation et l'endommagement, et qu'en fonction de la valeur du ratio des élongations critiques respectives pour chaque phénomène, deux types de rupture apparaissent.

Title : Gradient damage models in large deformation

Keywords : damage, rupture, cavitation, hyperelasticity, pressure, viscoelasticity

Abstract : Gradient damage models, also known as phase-field models, are now widely used to model brittle and ductile fracture, from the onset of damage to the propagation of a crack in various materials. Yet, they have been mainly studied in the framework of small deformation, and very few studies aims at proving their relevance in a finite deformation framework. This would be more helpful for the tyre industry that deals with very large deformation problems, and has to gain insight into the prediction of the initiation of damage in its structures.
The first part of this work places emphasis on finding analytical solutions to unidimensional problems of damaging viscous materials in small and large deformation. In all the cases, the evolution of damage is studied, both in the homogeneous and localised cases. Having such solutions gives a suitable basis to implement these models and validate the numerical results.
A numerical part naturally follows the first one, that details the specificities of the numerical implementation of these non local models in large deformation. In order to solve the displacement and damage problems, the strategy of alternate minimisation (or staggered algorithm) is used. When solved on the reference configuration, the damage problem is the same as in small deformation, and consists in a bound constraint minimisation. The displacement problem is non linear, and a mixed finite element method is used to solve a displacement-pressure problem. A quasi-incompressible Mooney-Rivlin law is used to model the behaviour of the hyperelastic material. Various tests in 2D and 3D are performed to show that gradient damage models are perfectly able to initiate damage in sound, quasi-incompressible structures, in large deformation.
In the simulations depicted above, it should be noted that the damage laws combined to the hyperelastic potential results in an initiation of damage that takes place in zones of high deformation, or in other words, in zones of high deviatoric stress. However, in some polymer materials, that are known to be quasi-incompressible, it has been shown that the initiation of damage can take place in zones of high hydrostatic pressure. This is why an important aspect of the work consists in establishing a damage law such that the material be incompressible when there is no damage, and the pressure play a role in the damage criterion. Such a model is exposed in the third part.
Finally, the last part focuses on the cavitation phenomenon, that can be understood as the sudden growth of a cavity. We first study it as a purely hyperelastic bifurcation, in order to get the analytical value of the critical elongation for which cavitation occurs, in the case of a compressible isotropic Neo-Hookean material submitted to a radial displacement. We show that there is a competition between the cavitation phenomenon and the damage, and that depending on the ratio of the critical elongation for damage and the critical elongation for cavitation, different rupture patterns can appear.

Université Paris-Saclay
Espace Technologique / Immeuble Discovery
Route de l'Orme aux Merisiers RD 128 / 91190 Saint-Aubin, France